KINEMATIC FINITE-FAULT MODEL OF THE OCTOBER 23, 2011 VAN M_w7.1 EARTHQUAKE OBTAINED FROM REGIONAL AND TELESEISMIC P WAVES USING THE EMPIRICAL GREEN FUNCTION METHOD

by

Zeynep Yılmaz

B.S., Geophysical Engineering, İstanbul University, 2008

Submitted to the Kandilli Observatory and Earthquake Research Institute in partial fulfillment of the requirements for the degree of Master of Science

Graduate Program in Geophysics

Boğaziçi University

2013

ACKNOWLEDGEMENTS

First of all, I would like to thank my thesis advisors, Professor Hayrullah Karabulut and Assistant Professor Ali Özgün Konca, for their genuine academic support and guidance during these two years. I am sincerely and heartily grateful to my advisor, Professor Hayrullah Karabulut for his continuous support, patience and scientific advice and knowledge. I am truly indebted and thankful to my advisor, Assistant Professor Ali Özgün Konca who was always eager to help and my primary resource for getting my questions answered and gave me his endless support. This thesis would not have been possible without their invaluable assistance, understanding, patience and encouragement. They have provided, with kindness, their keen scientific insight and excellent suggestions, which are very precious to me. I feel fortunate to have had a chance to work with them and learn from them.

I also like to thank Professor Argun Kocaoğlu, who accepted to be on my jury and gave me many precious suggestions. I also wish to thank Professor Nurcan Meral Özel. She always made me invaluable contributions. I am grateful to my former research advisor Professor Yıldız Altınok. She always helped me as an undergraduate student.

I would also like to thank all my teachers Professor Cemil Gürbüz, Mustafa Aktar and Niyazi Türkelli for their patient instruction. I am thankful to many of the faculty members in Geophysics Department who supported me.

I would like to express my eternal gratitude to my parents and my brothers Engin and Adnan. I will forever be thankful to my cousin Selin Taşkent who was my best role model throughout my life. Finally, I would like to thank my cousins Burak Sakarya and Ahmet Taşkent and my dear friends Nilay Başarır, Yasemin Korkusuz and İrfan Kılıç who always boosted me morally and provided me great information resources.

ABSTRACT

KINEMATIC FINITE-FAULT MODEL OF THE OCTOBER 23, 2011 VAN M_w 7.1 EARTHQUAKE OBTAINED FROM REGIONAL AND TELESEISMIC P WAVES USING THE EMPIRICAL GREEN FUNCTION METHOD

We obtained a kinematic finite-fault rupture model for the October 23, 2011 M_w 7.1 Van Earthquake using Empirical Green Function (EGF) method. We used an M_w 6.0 aftershock which occurred 10 hours after the main event as the EGF event. The analysis is performed for two distance ranges; regional (1°-20°) and teleseismic (20°-90°). Stations were selected to have good azimuthal coverage and high S/N levels as well as the similarity of the waveforms between the mainshock and the EGF event. Data from 52 regional and 33 teleseismic stations were used and the deconvolution is performed in the time domain. The shapes of the source time functions varying with the azimuth of the stations were mapped into the spatial evolution of slip. The inversion of the source time functions was performed with rupture velocities of 1.0-4.0 km/s with the interval of 0.5 km/s and the rise times of 1.0-5.0 s with the interval of 0.5 s. Finally the source model was tested by evaluating the difference between the original source time functions and the synthetic source time functions which were predicted by forward modeling. Teleseismic and regional slip distributions are found consistent. The slip distribution shows that the fault rupture propagated up-dip towards southwest. The maximum slip is approximately 3.5 m and the rupture velocity is between 1.5 and 2.0 km/s with the rise times of 1.0 s to 2 s where the models have high variance reductions.

ÖZET

23 EKİM 2011 VAN M_w 7.1 DEPREMİNİN KİNEMATİK SONLU-FAY MODELİNİN BÖLGESEL VE TELESİSMİK P DALGALARI KULLANILARAK AMPİRİK GREEN FONKSİYONU İLE BULUNMASI

23 Ekim 2011 Van M_w 7.1 depreminin sonlu fay kırılma modelini Ampirik Green Fonksiyonu (AGF) metodu kullanarak elde ettik. Bunun için ana şoktan 10 saat sonra meydana gelen artçı şok AGF olarak kabul edildi. Analiz bölgesel (1°-20°) ve telesismik (20°-90°) olmak üzere iki uzaklık aralığında gerçekleştirildi. İstasyonların seçiminde, ana şok ve artçı şok dalga şekillerinin benzerliğinin yanı sıra sinyal/gürültü oranının yüksek olmasına ve iyi bir yönsel dağılıma sahip olmalarına dikkat edildi. 52 tane bölgesel, 33 tane telesismik istasyon seçildi. Dekonvolüsyon işlemi zaman ortamında gerçekleştirildi. Yönsel olarak şekli değişen kaynak zaman fonksiyonları kullanılarak, kayma modelleri oluşturuldu. Kaynak zaman fonksiyonlarının ters çözümü, kırılma hızları 1 km/s ile 4km/s arasında 0.5 km/s aralıklarla ve yükselim zamanları ise 1.0 s ile 5 s arasında 0.5 s aralıklarla gerçekleştirildi. Orijinal kaynak zaman fonksiyonları ile yapay kaynak zaman fonksiyonları arasındaki farklar değerlendirilerek, kaynak model test edildi. Sonuç olarak, telesismik ve bölgesel kayma dağılımlarının birbirleriyle uyumlu olduğu görülmüştür. Kayma dağılımları, fay kırığının eğim yukarı güney-batı yönünde yayıldığını göstermiştir. Maksimum kayma büyüklüğü yaklaşık 3.5 m olarak hesaplanmış ve modelin varyans azaltma değerleri karşılaştırılarak, kırık hızı 1.5 km/s ile 2.0 km/s arasında ve yükselim zamanı ise 1.0 s ile 2.0 s arasında bulunmuştur.

TABLE OF CONTENTS

LIST OF FIGURES

LIST OF TABLES

LIST OF SYMBOLS / ABBREVIATIONS

EGF	Empirical Green Function
STF	Source Time Function
P	Primary waves
M_0	Seismic Moment (Nm)
str	Strike
M_w	Moment Magnitude
V_R	Rupture velocity
T_D	Rise time
δ	Dirac delta function
L	Fault length
W	Fault width
A	Fault area
λ	Smoothing constant
α	Parameter alpha
$\overline{D}$	The mean displacement
P	The potency
D (x,y,t)	The slip history
G (x,y,t)	Green's function
T	Time delay
∇_j^2	The Laplacian operator
w_j	Weight
B_j	Source time function of a subfault
N	Number of subfaults
N	Number of subfaults
μ	Rigidity (Shear Modulus)
f	Frequency
S	Rupture surface
S/N	Signal to noise ratio
GMT	Greenwich Mean Time
GIMP	The GNU Image Manipulation Program

Lat	Latitude
Lon	Longitude
Mag	Magnitude
str	Strike
bp	Bandpass filter
bu	Butterworth filter
Alp	The width of the Gaussian filter
u(t)	The earthquake time series (seismogram)
s(t)	The synthetic seismogram
x(t)	The source signal of the earthquake
q(t)	The site effect
i(t)	The instrument Response
SAC	Seismic Analysis Code
NAF	North Anatolian Fault
EAF	East Anatolian Fault
BS	Bitlis Suture
KbF	Kavakbaşı Fault
EAAC	Eastern Anatolian Accretionary Complex
ALM	Lithospheric mantle of Arabian Plate
BPLM	Lithospheric mantle of Bitlis Pötürge Massif
PLM	Lithospheric mantle of the Pontides
EMSC	Eastern Mediterranean Seismological Center
USGS	The United States Geological Survey
IRIS	Incorporated Research Institutions for Seismology
KOERI	Kandilli Observatory and Earthquake Research Institute
ISC	International Seismological Centre
USGS	The United States Geological Survey
CMT	The Global Centroid Moment Tensor
ÇDFZ	Çobandede Fault Zone
KF	Kağızman Fault
TF	Tulak Fault
BGF	Balıkgölü Fault
VR	Variance Reduction

1. INTRODUCTION

The October 23, 2011 Van Earthquake (M_w 7.1) at 13.41 local time (10.41 GMT) occurred on the Bitlis Suture Zone in the northeast of the city of Van in eastern Turkey at a depth of 16.0 km. Emre (2011) suggested that the Van Earthquake happened on a newly found Van Fault on the east of Lake Van (Taşkın *et al*., 2013). Bitlis Suture Zone and Zagros fold and thrust belt which are formed as a result of the collision of Arabian Plate and Eurasian Plate control the seismicity of Lake Van and its surroundings. The surface area of the fault is approximately 20x20 km with a 241° of strike angle to SW and a 51° of dip angle in the direction of SW according to USGS. The fault mechanism is oblique-thrust and in good agreement with the previous earthquake focal mechanisms in this region (Örgülü *et al*., 2003) (Figure 1.1) just as 15 November 2000 Van Earthquake which is 58 km from the 2011 event's hypocenter (Utkucu, 2013) as shown in Figure 1.2.

The goal of this study is to generate a kinematic source model and determine source effects such as rupture velocity and the rise time for the Van Earthquake by utilizing the regional and teleseismic. In order to obtain spatiotemporal models of the earthquake rupture, we utilized an Empirical Green Function Method (Dreger, 1994; Hartzell, 1978). We have chosen M_w 6.0 event as an Empirical Green Function which occurred 10 hours after the main event having the similar focal mechanisms and locations with the mainshock. We computed the source time function for the mainshock via deconvolution in the time domain. We used the iterative time domain deconvolution algorithm of Ligorria and Ammon (1999) which is an application of the Kikuchi and Kanamori (1982) method. We have obtained slip distribution models and the rupture directivity and found the optimal rupture velocities and rise times according to variance reductions. High variance reductions show that the rupture velocity is between 1.5 km/s and 2 km/s, the rise time is approximately between 1.0 s and 2 s and maximum slip is 3.5 m. Consistent regional and teleseismic slip models show that the rupture propagated updip and towards SW in the strike direction.

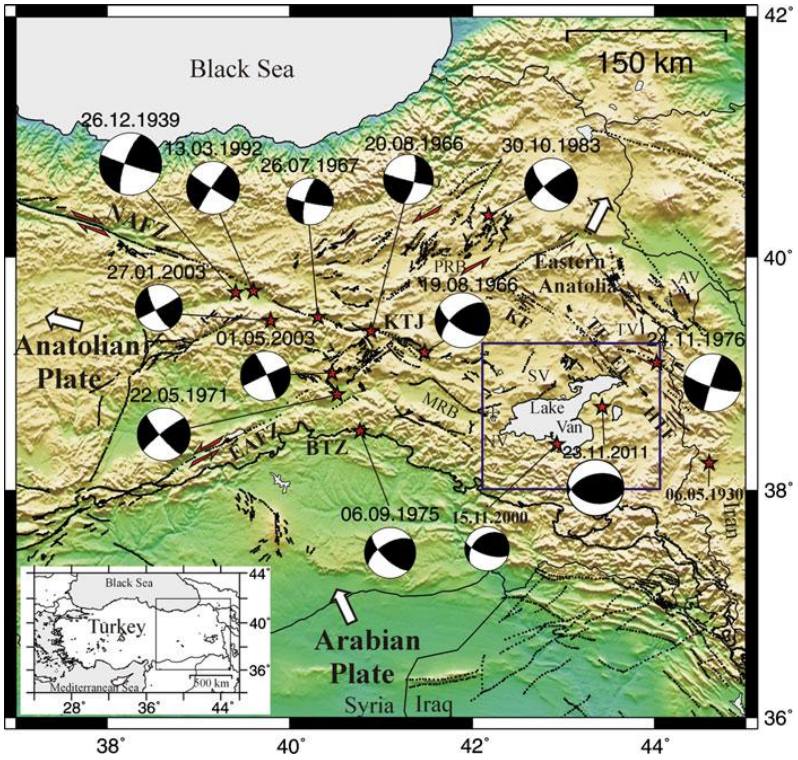

Figure 1.1. Map of the October 23, 2011 (M_w 7.1) Van Earthquake and historical earthquakes M_w > 6.0 with fault mechanisms in Eastern Turkey (McKenzie, 1972; Pınar, 1995; Şaroğlu F *et al*., 1992; Taymaz *et al*., 1991; Toksöz *et al*., 1978; Utkucu, 2013).

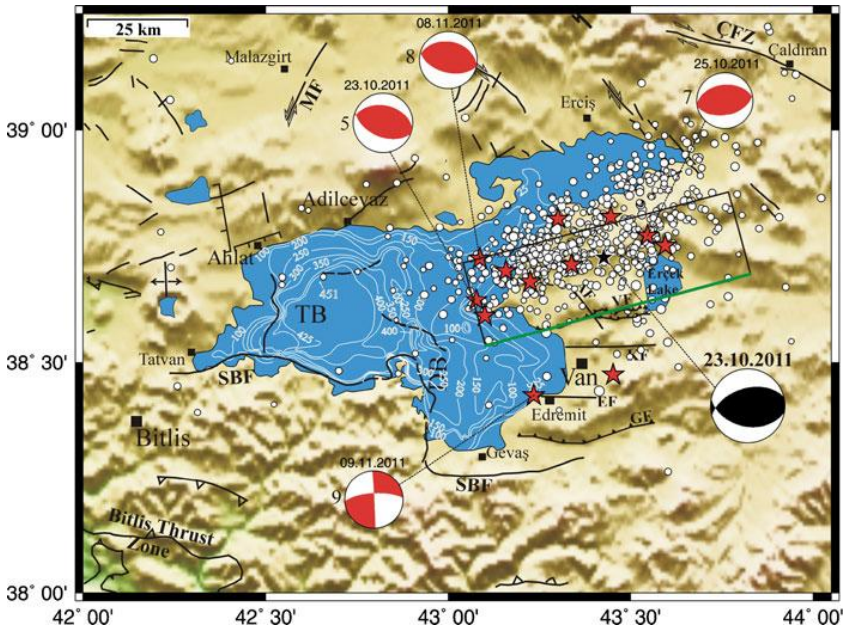

Figure 1.2. Map of seismicity of Lake Van and the October 23, 2011 (Mw 7.1) Van Earthquake and aftershocks with source mechanisms (Utkucu, 2013).

2. TECTONICS OF TURKEY AND EASTERN ANATOLIA REGION

2.1. General Tectonic Settings of Turkey and its Surroundings

The east-west oriented mountain ranges of Turkey are part of the Alp-Himalayan orogenic belt system. Convergence of African and Eurasian continents started with closing of Paleo-Tethys ocean. Thus the continental plates bordering the Paleo-Tethys ocean collided and formed the collision zones and mountain ranges. The Alps were formed 30 million years ago as a result of the collision of these two plates. Indian and Eurasian Plates formed the Himalayas starting around 10 Ma.

In the Oligocene, African and Arabian Plates started to separate from each other by the Red Sea Rift extending from the Afar triple junction to south of Dead Sea Fault (Figure 2.2). Both of the plates move towards north; however, the Arabian Plate is relatively faster (Reilinger *et al*., 2006). African Plate is divided into two recent plates named Somalian and Nubian in the African Rift Zone as shown in Figure 2.2. Other tectonically significant component of the region is the Hellenic Trench which has formed due to the subduction of oceanic crust of Arabian beneath Eurasian Plate. Aden Ridge is a spreading center between Arabian and African Plates extending from Afar Junction to Owens Fracture Zone which is a transform boundary separating Indian Plate from Arabian and African Plates. Between the Arabian and African Plates, there is one more boundary called the Dead Sea Fault. It is a left lateral transform fault and stretches from Maraş triple junction -where it meets with Eastern Anatolian Fault- towards the north of Red Sea Rift (Reilinger *et al*., 2006). Dead Sea Fault also has an extension *i.e*. pull apart basin which is a depression where Dead Sea exists. Arabian Plate is moving towards Eurasian Plate and forming Bitlis Zagros Suture Zone (Faccenna *et al*., 2006) and Caucasus mountain belts. Eastern Anatolia which situates behind the suture zone and forms the NW part of Turkish-Iranian Plateau is one of the high plateaus of Alp-Himalayan belt system and approximately 2 km high above sea level (Keskin, 2003) as shown in Figure 2.1.

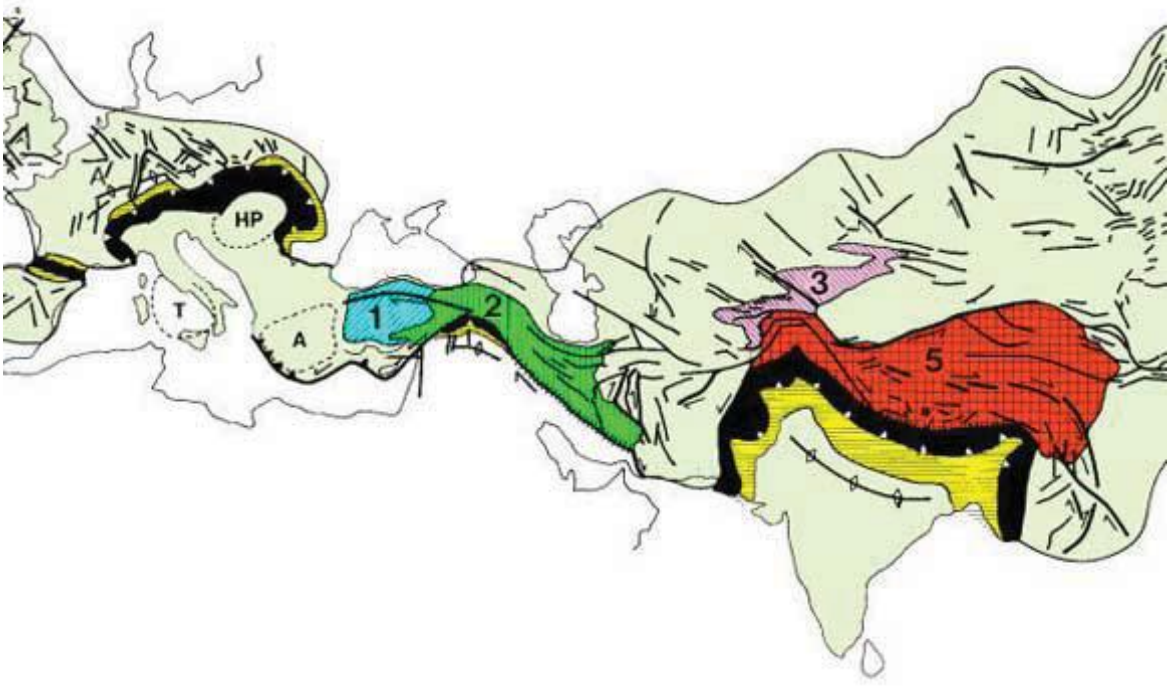

Figure 2.1. Map of Alp-Himalayan belt system and 2: Eastern Anatolian Plateau (Dewey *et al*., 1986; Keskin, 2003).

The compression of the collision zone causes Anatolian Plate to escape and rotate westward by the transform faults North Anatolian Fault and East Anatolian Fault which are active since miocene. North Anatolian Fault is 1300 km and right lateral (Dewey and Şengör, 1979; McClusky *et al*., 2000; Şengör, 1979) while East Anatolian Fault extending between Arabian and Anatolian Plates is left lateral (Jackson and McKenzie, 1988; McKenzie, 1972) with reverse component. Just Palu area shows reverse mechanisms due to the local compression (Örgülü *et al*., 2003). Main Recent Fault which is in NW Iran (Zagros Mountains) is a continuation of North Anatolian Fault and shows an approximately continuous dextral shear.

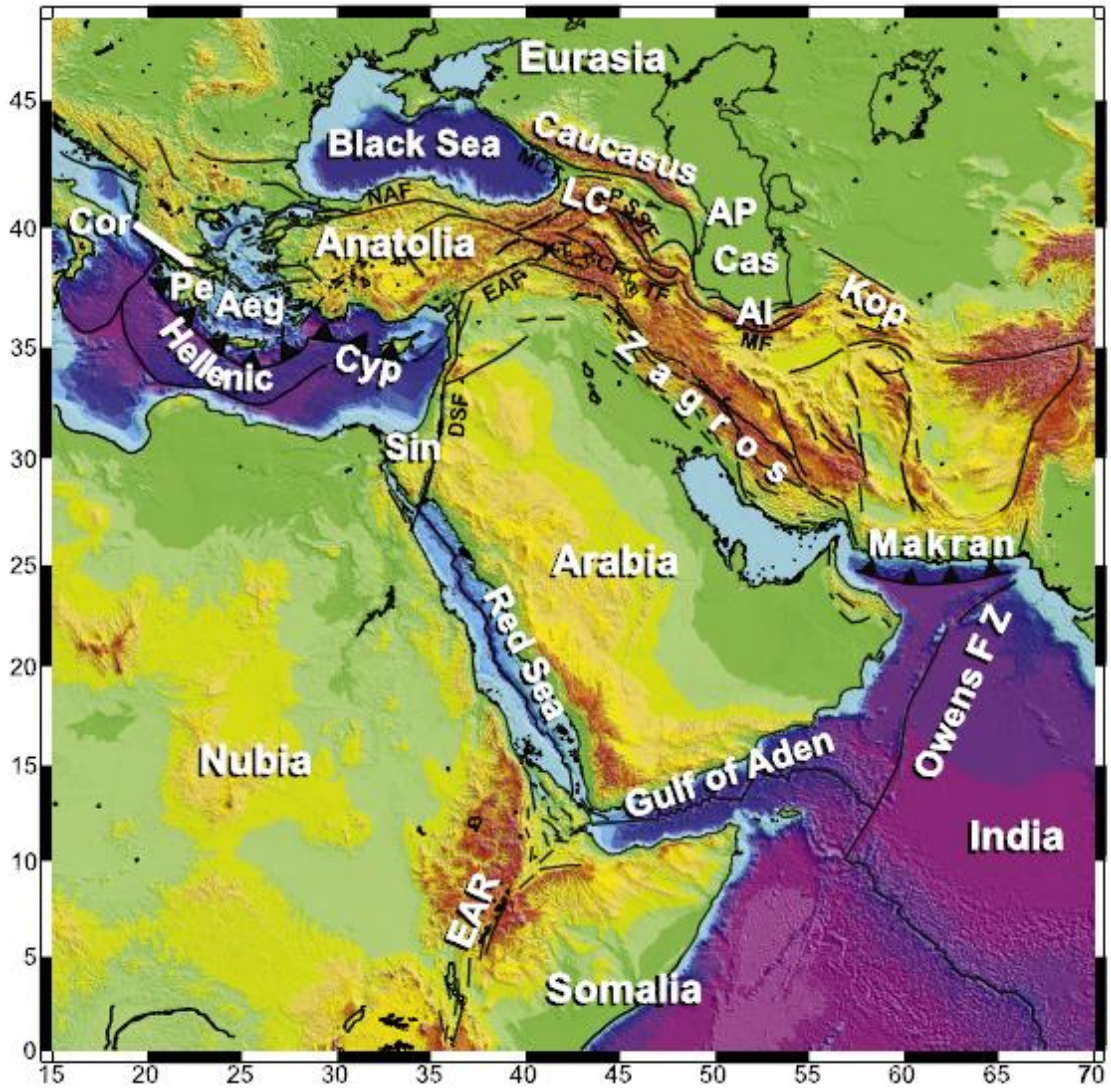

Figure 2.2. Map of African-Arabian-Eurasian collision zone (Reilinger *et al*., 2006).

The fault plane solutions of the earthquakes are an indicator of the plate boundaries such as collision zone in Eastern Anatolia, North Anatolian and East Anatolian Faults, Hellenic and Cyprus Trenches, East African Rift, Red Sea Rift and Aden Ridge as shown in Figure 2.3 (Reilinger *et al*., 2006). Except these plate boundaries most of the area is aseismic. There is a counterclockwise rotation from Arabian Plate to Hellenic Trench parallel to North Anatolian Fault with an increasing velocity toward west (Toksöz *et al*., 1999). The rollback along the Hellenic and Cyprus Trench and the collision of the African Plate at the east, is the primary reason for the counterclockwise rotation, which is characterized by east-west normal faults along Aegean, right lateral strike-slip motion

along NAF, and right and left lateral and thrust faulting in the Eastern Anatolia (Reilinger *et al*., 2006) (Figure 2.3).

.

The North Anatolian Fault and East Anatolian Fault intersect at Karlıova Junction which is a pull apart basin. A pull apart basin forms when the displacement related to strike slip faults pulls a segment of mass apart leading to extension in the region.

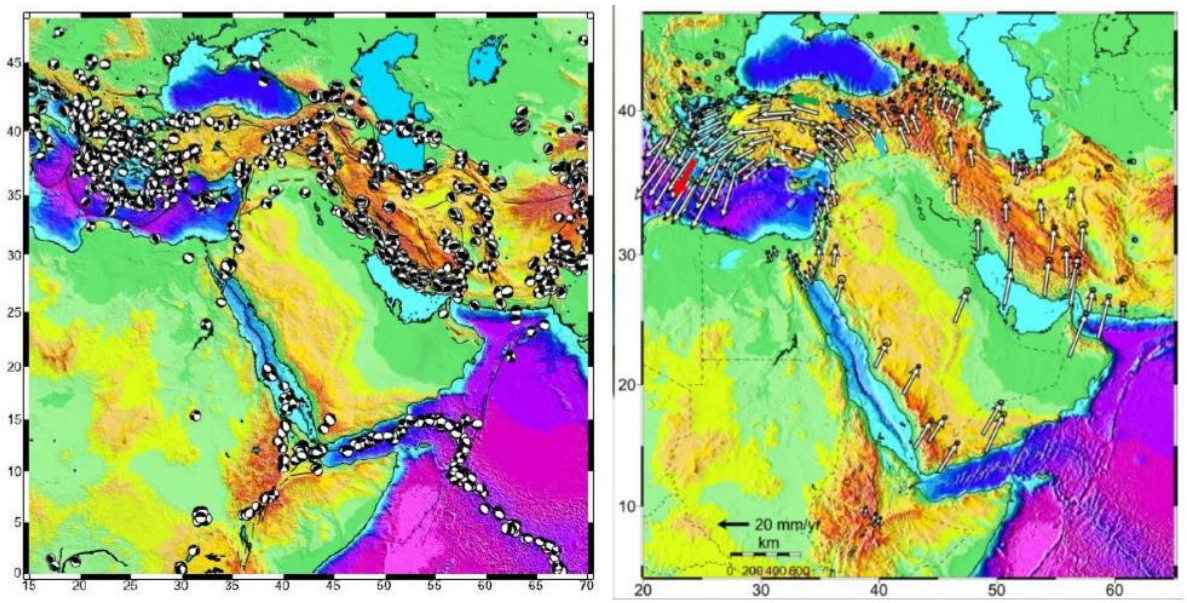

Figure 2.3. Map of African-Arabian-Eurasian collision zone with (a) focal mechanisms and (b) GPS velocities (Reilinger *et al*., 2006).

Figure 2.4. Map of tectonic plates and faults around Turkey (basemap-ESRI).

2.2. Eastern Anatolian High Plateau

The geographic coordinates of the Eastern Anatolian High Plateau lie between the latitudes of 38°N-41°N and longitudes of 41°E-45°E. In the north it has a boundary with Pontide/Minor Caucasus Zone (Dewey *et al*., 1986), while the Zagros Mountains forms the southern extrimity. The average elevation of the plateau is 2200 m above sea level. The Central Range (3000 m above sea level) separates the plateau into two depressions namely Erzurum Kars Plateau and Murat Region which are encircled by high mountains. The area of the southern part of the plateau -the trapezoidal shaped Murat Region- is larger than the northern part which is the triangular shaped Erzurum Kars Plateau (Şengör *et al*., 2008). The elevations of the bottom of the two depressions are above 1500 m. Murat Region is endorheic *i.e*. a closed dreainage around Lake Van. The plateau consists of tectonic plates namely the Northwest Iranian Plate, Eastern Rhodope-Pontide, The Eastern Anatolian Accretionary Complex, Arabian Foreland and the Bitlis-Pötürge Massif (Figure 2.5) (Keskin, 2005; Şengör *et al*., 2003).

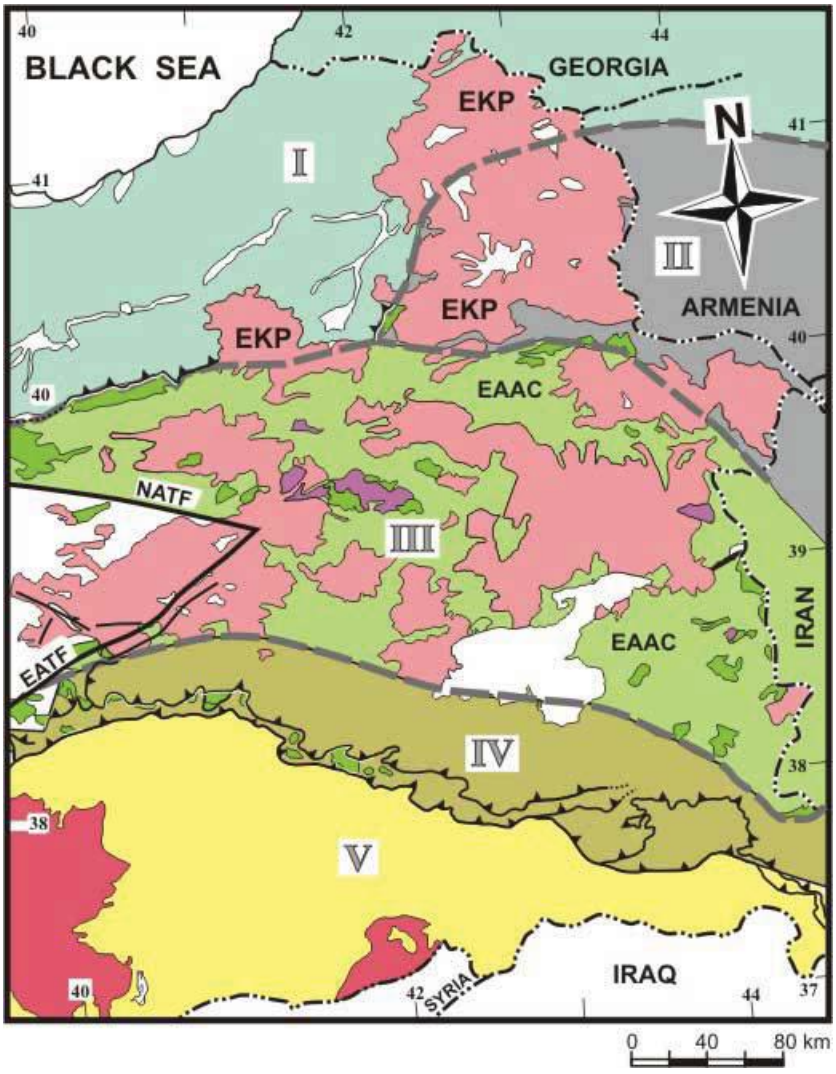

Figure 2.5. Tectonic plates of Eastern Anatolian Plateau I: Rhodope-Pontide fragment, II: Northwest Iranian fragment, III: Eastern Anatolian Accretionary Complex (EAAC), IV: Bitlis-Pötürge Massif and V: Arabian foreland (Keskin, 2005; Şengör *et al*., 2003).

Receiver Function studies show that crustal thickness in Eastern Anatolia changes between <38 km in the south Bitlis Suture Zone and 50 km in the north about the Erzurum-Kars Plateau (Zor *et al*., 2003). The average thickness of the crust in Eastern Turkey is 45 km which is not usual in a continental collision zone. The smallest crust in Eastern Anatolia is in the central part of the Lake Van Dome where Lake Van locates (Figure 2.6). The crust is thicker than 46 km in the Northwest Iranian Fragment, the south of the Rhodope–Pontide Fragment and north of the Bitlis Massif. The highest elevation in Eastern Anatolian Plateau concides with the thinnest crust beneath the Murat Region.

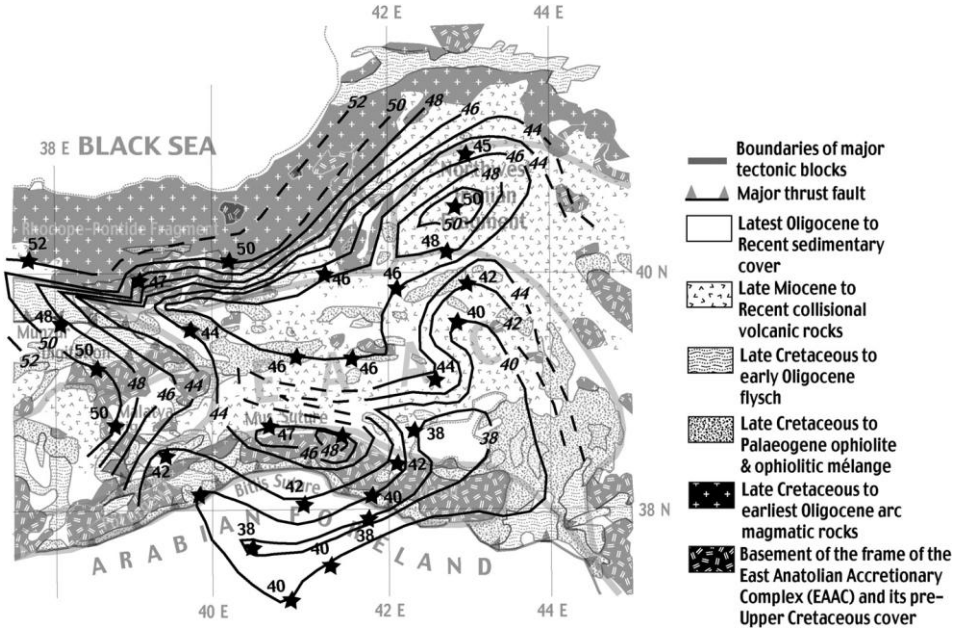

Figure 2.6. Map of Eastern Anatolian Plateau showing crustal thicknesses (Şengör *et al*., 2003).

The Eastern Anatolian High Plateau is an active, Turkic type orogen and formed in the late miocene, after the collision of the Arabian and Eurasian Plates (Şengör *et al*., 2008). Post collisional magmatism in the plateau is a consequence of the slab detachment or break off under the subduction-accretionary complex whose age is between Late Cretaceous to earliest Oligocene. Beneath Eastern Anatolia there is not a lithospheric mantle which means existence of asthenosphere directly below the crust. The slab detachment or break off leads to flow and rise of materials of mantle and forms a high elevation plateau Eastern Anatolia (Şengör *et al*., 2003).

Whereas Tibet type post colliisional magmatism occurs as a result of the crustal melting and is calc-alkalic type (Dewey and Burke, 1973), Turkic type post collisional magmatism additionally contains alkalic to peralkalic materials as in the Eastern Anatolian Plateau (Şengör *et al*., 2008). Calc-alkalic type rocks are in the north while alkalic type rocks are in the south and transitional rocks are in the middle of the plateau. In the plateau, the ages of volcanics change between 11 ma and 17 century in the direction of south.

Whle the Eastern Anatolian Accretionary Complex was shortening and thickening between the Oligocene and Serravalian, the subduction stopped (Figure 2.7.a). Consequently, oceanic plate steepened and resulted in detachment beneath the Eastern Anatolian Accretionary Complex. This created an opening for asthenospheric mantle wedge and a southward mantle flow which carried the partly depleted mantle with subduction component from north (Figure 2.7.b,c). After slab steepening and break-off, a slab window created and filled with hot asthenosphere causing a melting under the collision zone. This changed the direction of the asthenospheric mantle flow to north and carried the enriched hot material under the Arabian Plate to shallow depths (Figure 2.7.d). The mixture of the enriched material with the partly depleted mantle containing a subduction component created a variety of volcanic material (Keskin, 2007).

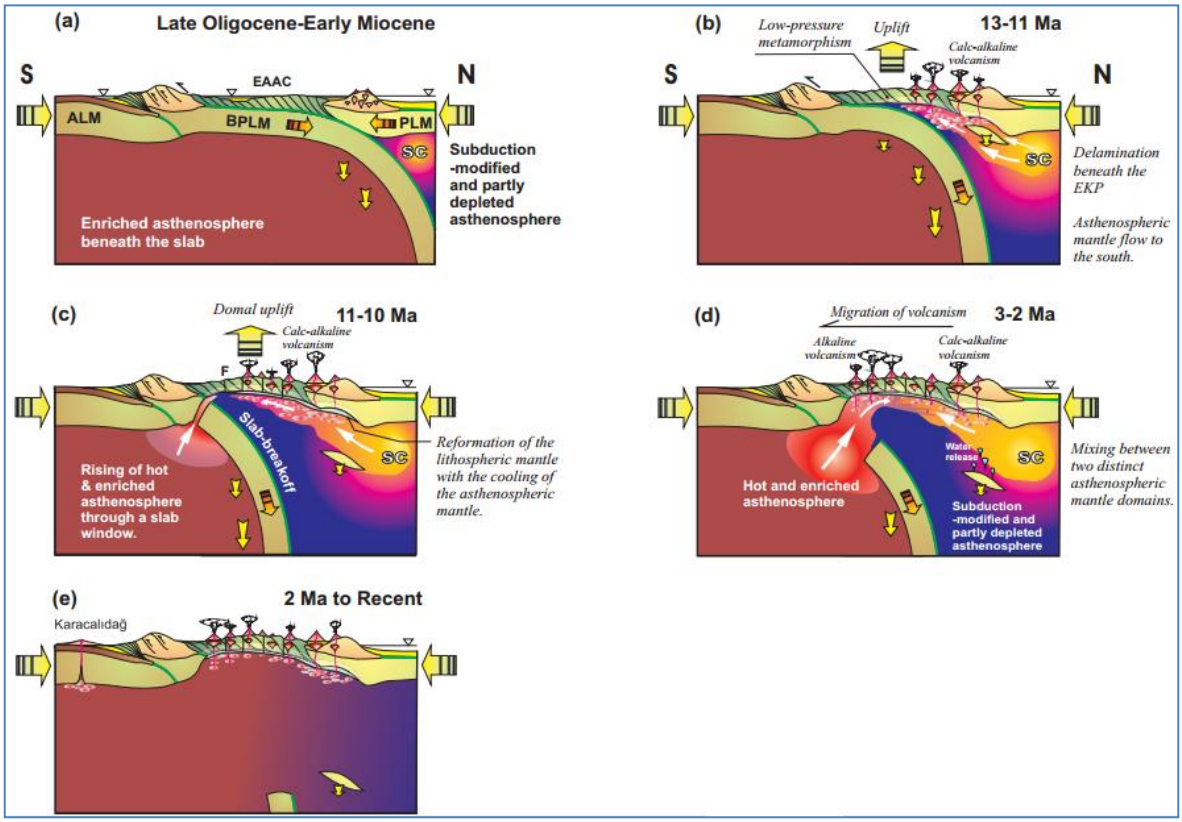

Figure 2.7. Eastern Anatolian Collision Zone where F denotes strike slip faults; EAAC is Eastern Anatolian Accretionary Complex and SC asthenospheric mantle. ALM, PLM and BPLM are respectively listhospheric mantles of Arabian Plate, the Pontides and Bitlis Pötürge Massif (Keskin, 2007).

When the topographic profiles of Eastern Anatolian Plateau and Ethiopian Plateau are compared despite of totally different tectonic settings, it is clearly seen that both of the profiles fit to the Wilson cycle (Figure 2.8) (Şengör *et al*., 2003). They both have hot, rising asthenosphere directly above the crust and are deprive of lithospheric mantle.

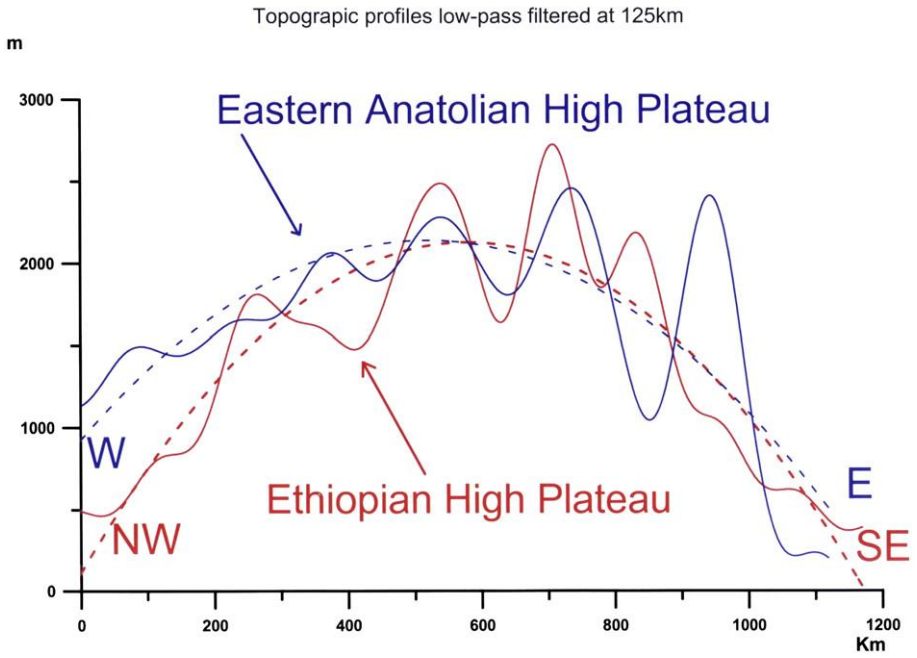

Figure 2.8. Similarity between the topographic profiles obtained from Eastern Anatolian Plateau and Ethiopian Plateau (Şengör *et al*., 2003).

The compresssional behaviour and crustal shortening and thickening in Eastern Anatolia is replaced by conjugate strike slip faults due to lack of major thrust faults (Dhont and Chorowicz 2006). Also lack of subcrustal earthquakes and existence of strike slip earthquakes refute the continuing crustal shortening. These distributed strike slip faults demonstrate a V-shape since the fault and the maximum compressive stress cuts at an angle with 60-75 degrees (Yin and Taylor, 2008). These faults are parallel to North Anatolian Fault and East Anatolian Fault. To exemplify, Kavakbaşı (KbF), Tulak (TF) and Balıkgölü (BGF) Faults are right lateral faults (Bozkurt, 2001; Koçyiğit *et al*., 2001; Örgülü *et al*., 2003) which are parallel to North Anatolian Fault with the trend of NW-SE while Çobandede Fault Zone (ÇDFZ) and Kağızman Fault (KF) are left lateral which are parallel to East Anatolian Fault with the trend of NE-SW (Figure 2.4). There are also a few reverse faults (Örgülü *et al*., 2003). Furthermore, Türkelli *et al*. (2003) observed that North

Anatolian Fault continues to the east of Karlıova Junction.

There are not any reverse focal mechanisms at the foreland of the Bitlis Zagros Suture Zone. A foreland basin can be defined as the depression caused by lithospheric flexure process. While the crustal thickening occurs as a result of the continental collision, the mass gives rise to bending in the lithosphere called as lithospheric flexure. Most of the faults are right lateral strike slip faults in the Eastern Anatolia (Figure 2.9). The north boundary of the Eastern Anatolia shows left lateral faulting such as Çobandede Fault. Reverse mechanisms occur at Caucasus Region in the north and shows crustal thickening. Muş-Lake Van and Pasinler Basins with the E-W trend are other tectonic settings of the region which show N-S compression (Şengör, *et al*. 1985).

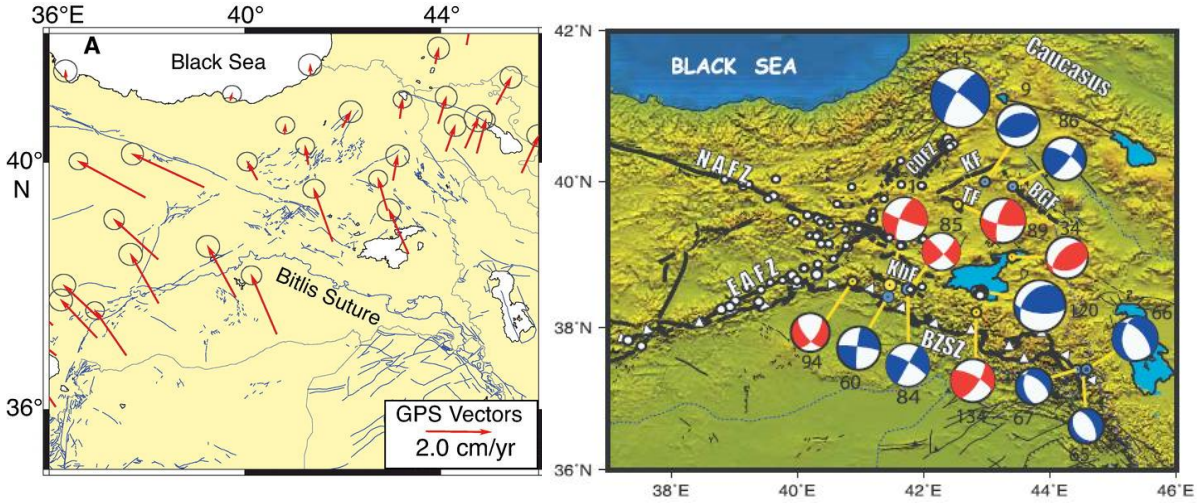

Figure 2.9. Map of Eastern Turkey with (a) GPS velocities (Barazangi *et al*., 2006) and (b) focal mechanisms (Örgülü *et al*., 2003).

2.3. 2011 M_w 7.1 Van Earthquake

The October 23, 2011 Van Earthquake (M_w 7.1) at 13.41 local time (10.41 GMT) occurred on the Bitlis Suture Zone in the northeast of the city of Van in Eastern Turkey at a depth of 16.0 km which is followed by an aftershock sequence with the largest being an M_w 6 earthquake. USGS, CMT and finite fault model shows that the surface area of the fault is approximately 20x20 km with a 241° of strike angle and a 51° of dip angle (Hayes 2011). The fault mechanism is oblique-thrust (USGS) (Figure 2.11) and consistent with the

previous earthquake focal mechanisms in this region. 15 November 2000 Van Earthquake has a similar mechanism just 58 km from the 2011 main shock hypocenter (Utkucu, 2013).

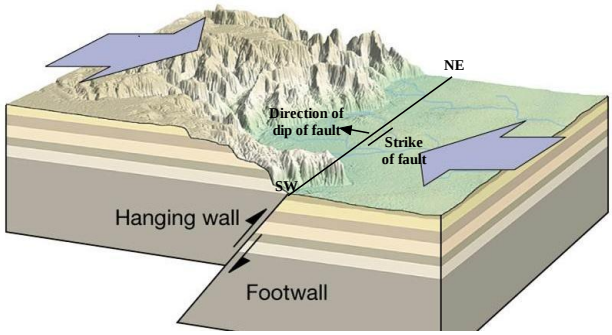

Figure 2.10. Figure of a reverse fault (http://www.studyblue.com/notes/note/n/chapter-10/deck/112814).

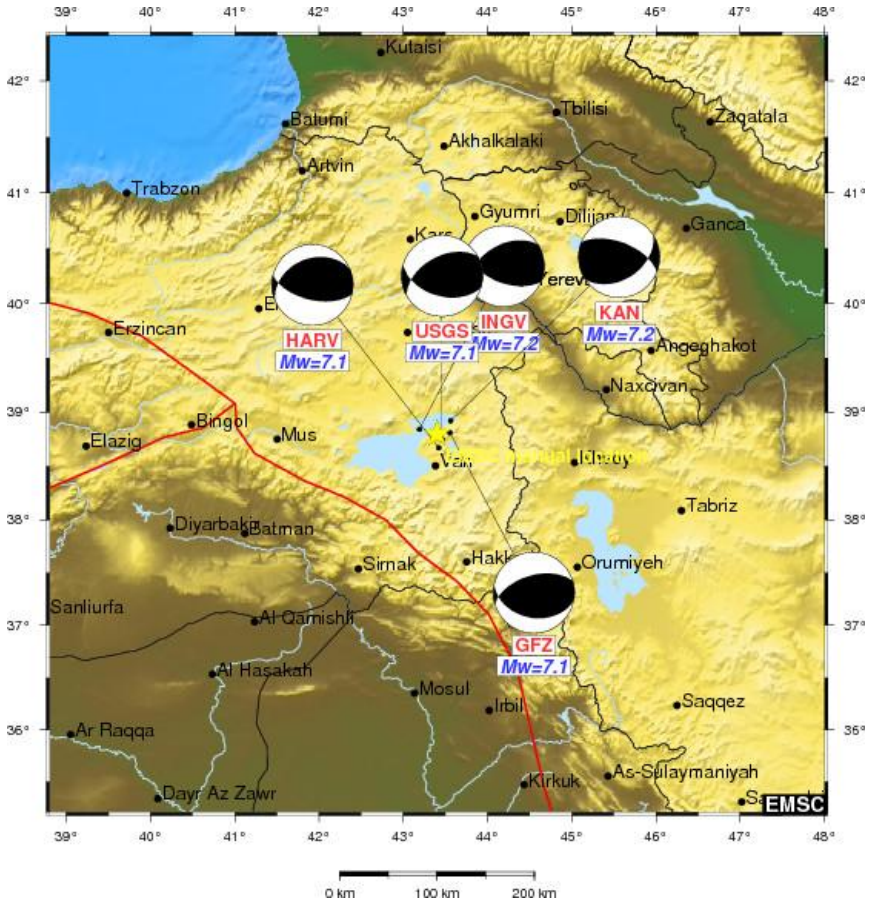

Figure 2.11. Location map of the October 23, 2011 Van Earthquake and focal mechanism from various agencies as given in the Table 2.1 (EMSC).

Table 2.1. Fault plane solutions of the October 23, 2011 Van Earthquake from various agencies.

	Latitude	Longitude	Depth (km)	Type	Magnitude
AFAD	38.6890	43.4657	19.02	M_l	6.7
	38.7578	43.3602	5	M_l	6.6
				M_w	7.2
USGS	38.691	43.497	16	M_w	7.1
	38.86	43.48	10	M_w	7.2
GFZ	38.674	43.581	15	M_w	7.1

Figure 2.12. Location map of the October 23, 2011 Van Earthquake and its aftershocks (red and yellow stars show the mainshock M_w 7.1 and the aftershock Mw 6.0 events, respectively. The circles are the subsequent events) (basemap ESRI, USGS).

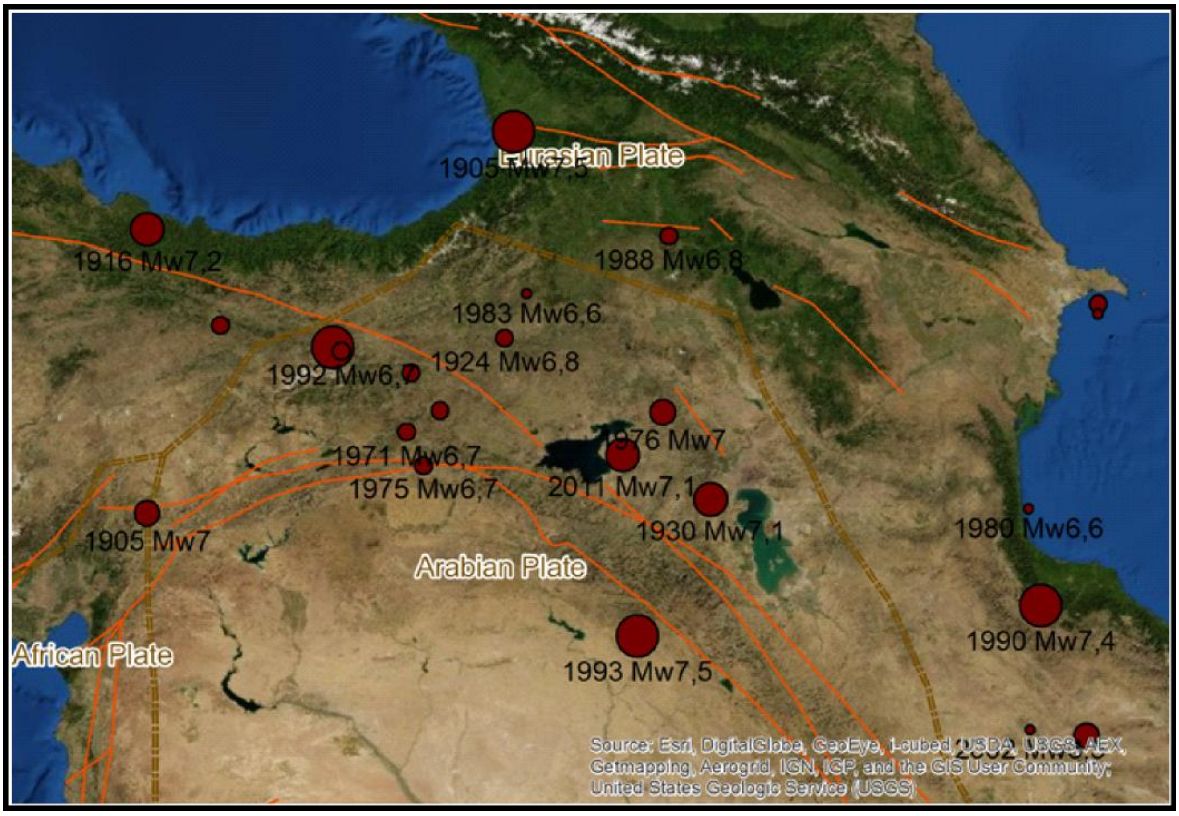

Figure 2.13. Location map of the October 23, 2011 Van Earthquake and previous earthquakes in the region $M_w > 6.5$ obtained from Table 2.2 (USGS, ESRI).

Table 2.2. List of Important Earthquakes Magnitude > 6.5 given by USGS.

Year	Month	Day	Time	Latitude	Longitude	Depth	Magnitude
1905	10	21	1101	42.000	42.000	60	7.5
1905	12	04	1220	38.000	37.000	60	7.0
1909	02	09	1124	40.000	38.000	60	6.8
1916	01	24	0655	41.000	37.000	0	7.2
1924	09	13	1434	39.864	41.876	35	6.8
1930	05	06	2234	38.152	44.685	25	7.1
1939	12	26	2357	39.770	39.533	35	7.8
1949	08	17	1844	39.500	40.600	0	6.8
1954	03	28	0447	39.100	41.000	0	6.8
1962	09	01	1920	35.556	49.810	17.6	6.9
1971	05	22	1644	38.868	40.542	3.6	6.7
1975	09	06	0920	38.516	40.768	39.7	6.7
1976	11	24	1222	39.083	44.030	9.7	7.0
1980	05	04	1835	38.047	49.018	25	6.6
1983	10	30	0412	40.328	42.177	15	6.6
1988	12	07	0741	40.928	44.114	5	6.8
1990	06	20	2100	37.001	49.186	19	7.4
1992	03	13	1718	39.728	39.654	7	6.7
1993	01	15	1215	36.666	43.686	42.4	7.5
2000	11	25	1809	40.226	49.974	50	6.8
2000	11	25	1810	40.123	49.960	37.7	6.5
2002	06	22	0258	35.626	49.047	10	6.5
2011	10	23	1041	38.628	43.486	20	7.1

3. DATA and METHODS

3.1. Data

In this study, our objective is to obtain a kinematic source model for the Mw 7.1 October 23, 2011 Van Earthquake. For this purpose, we utilize Empirical Green Function Method (Hartzell, 1978) using the STF inversion scheme by Dreger (1994). We obtained the regional data from Kandilli Observatory and Earthquake Research Institute (KOERI) and the teleseismic data from IRIS-WILBER II for the October 23, 2011 Van Earthquake and its aftershocks with magnitude M_w >5.5 as seen in Table 3.1. We merged the data from KOERI and WILBER II. Station coordinates are obtained from the ISC website (International Seismological Centre, On-line Bulletin, http://www.isc.ac.uk).

Table 3.1. List of the October 23, 2011 Van Earthquake and its aftershocks with magnitude M_w >5.5 obtained from WILBER II (http://www.iris.edu/cgi-bin/wilberII/wilberII_page1.pl).

Date	Time	Source	Mag	Lat	Lon	Description
2011/10/23	10:41:21.3	SPYDER®	7.3	38.63	43.53	TURKEY
2011/10/23	20:45:37.3	SPYDER®	6.0	38.56	43.16	TURKEY
2011/10/25	14:55:07.7	SPYDER®	5.7	38.80	43.56	TURKEY
2011/11/09	19:23:35.5	SPYDER®	5.7	38.35	43.40	TURKEY

However, we have chosen Empirical Green Function (EGF) event (Mw 6.0) which occurred 10 hours after the main event which has a similar mechanism and location with respect to the main shock as shown in Table 3.2 and Figure 3.1. The waveforms of the two other events were rather noisy and not suitable for this analysis.

Table 3.2. Fault plane solutions of the October 23, 2011 Van Earthquake and the aftershock used in our study (Global CMT Catalog).

Event	Date	Time	Epicentre	Depth	Moment	Plane1 str/dip/slip	Plane2 str/dip/slip
Main	23.10.2011	10:41:28.4	38.640/43.400	12.0	6.3E26	246/38/60	103/58/112
Aftershock (EGF)	23.10.2011	20:45:38.6	38.510/43.070	12.0	1.1E25	281/40/82	111/50/90

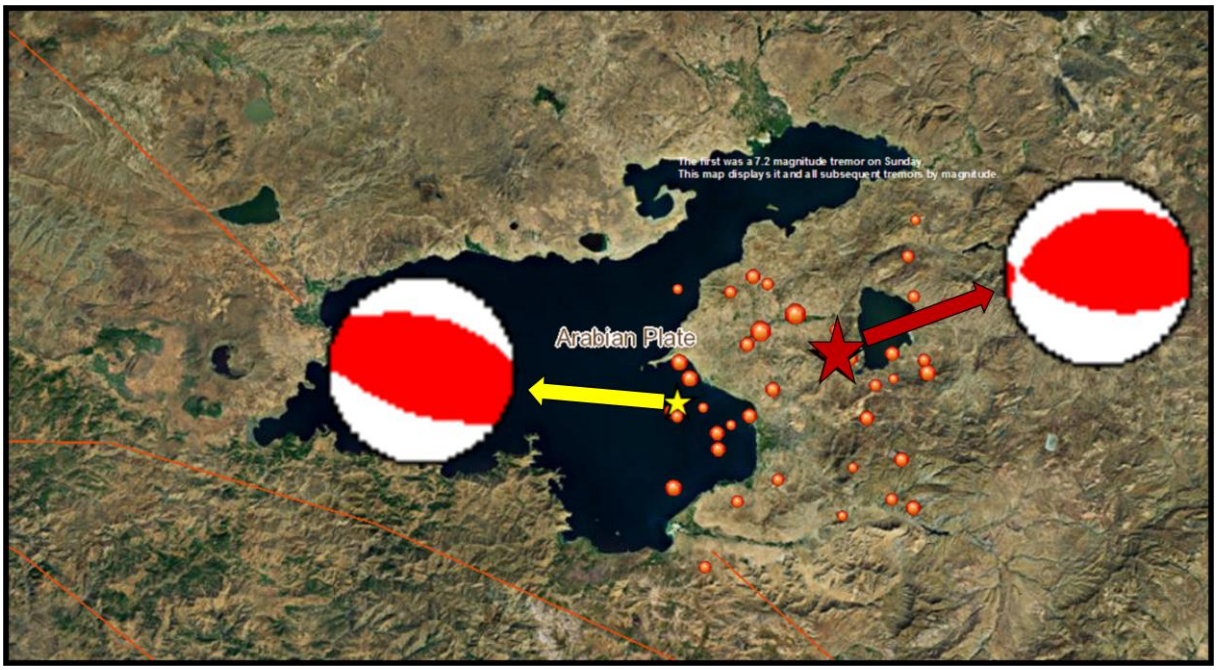

Figure 3.1. Location map of the October 23, 2011 Van Earthquake and the aftershock used in our study with focal mechanisms (Global CMT Catalog).

The seismic stations can be categorized into 3 classes according to their distances from the epicentre of the mainshock (Shear, 1999).

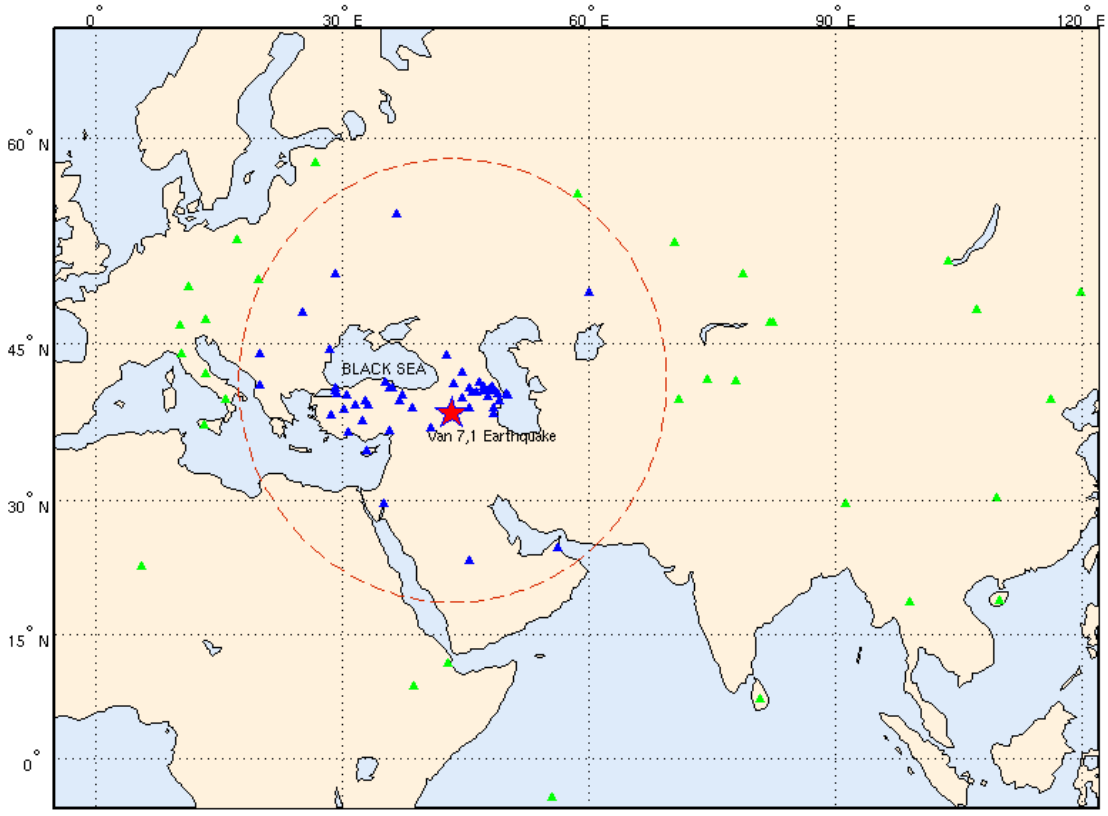

Figure 3.2. Map of the regional stations (1° - 20°) represented with blue triangles and teleseismic stations (30° - 90°) represented with green triangles (MATLAB).

We picked P waves for all 3 components and eliminated the noisy stations which led to azimuthal gap at some areas. A good azimuthal coverage is important for getting a clear directivity from source time functions. Data from 52 regional and 33 teleseismic stations were used (Figure 3.2).

3.2. Pre-processing

We cut the waveforms with respect to first P-wave arrival and used the time window 10 seconds before ($CUTL = -10\ s$) and 40 seconds after ($CUTH = 40\ s$) t_0 pick. A 4-pole (np=4) Butterworth filter (bu) is used as a bandpass filter (bp) with the low and high corner cutoffs (co). The frequency band used for the prefiltering was $FL = 0.05$ Hz (20 seconds) and $FH = 0.5$ Hz (2 seconds) which shows the corner frequencies. We removed the mean and the trend from data. We interpolated the traces to a sampling rate of 0.1 ($INTDELTA = 0.1$) and applied a hanning type taper with the width of 0.1.

3.3. Empirical Green's Function Method

Seismic signal from an earthquake travels through the earth and arrives at a receiver as shown in simple model below (Figure 3.3).

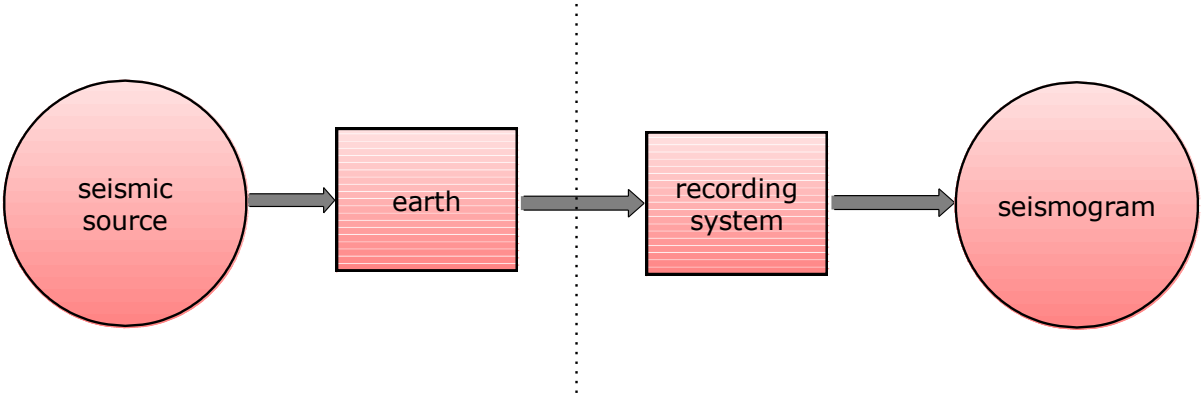

Figure 3.3. Diagram of a Seismogram (Scherbaum, 1994).

Seismogram is the convolution of earthquake source time function x(t) (the source signal of the earthquake), the site q(t) and the instrument response i(t) as seen in Figure 3.4 (Stein and Wysession, 2003) given by Equation 3.1.

$$u(t) \approx x(t) * q(t) * i(t) \tag{3.1}$$

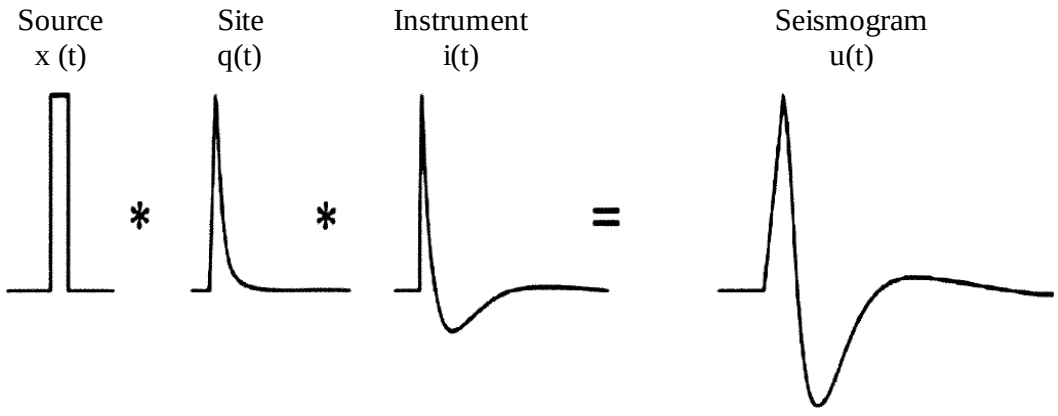

Figure 3.4. Demonstration of a seismogram as the convolution of the source, the site and the instrument response (Stein and Wysession, 2003).

$$U(w) \approx X(w) \,.\, Q(w) \,.\, I(w) \tag{3.2}$$

$$u(t) = \frac{1}{2\,\pi} \int_{-\infty}^{\infty} U(w) \,.\, e^{iwt} \,.\, dw \tag{3.3}$$

$$U(w) = \int_{-\infty}^{\infty} u(t) \,.\, e^{-iwt} \,.\, dt \tag{3.4}$$

$U_m(t)$ and $U_a(t)$ denotes the earthquake time series of the mainshock and aftershock events respectively.

$$U_m(t) \approx X_m(t) * Q_m(t) * I_m(t) \tag{3.5}$$

$$U_a(t) \approx X_a(t) * Q_a(t) * I_a(t) \tag{3.6}$$

Each earthquake has its distinctive source time function separating from others as shown in Figure 3.5 which is made by (Fukao and Kikuchi, 1987) displaying the large earthquakes which occurred in 1960s and 1970s.

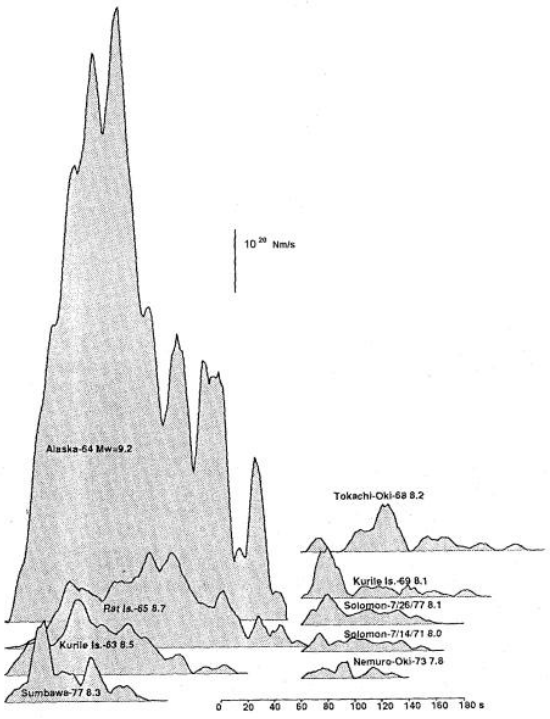

Figure 3.5. The differences in source time functions of large earthquakes (Fukao and Kikuchi, 1987).

In order to isolate source time functions and remove the other two effecs from seismograms at each station, a smaller aftershock event (EGF) is chosen and deconvolved from the mainshock event (Hartzell, 1978). This Empirical Green Function (EGF) needs to have approximately same time arrivals, focal mechanisms and locations as the mainshock. Figure 3.6 shows that while the waveforms of the main event have long durations the waveforms of the aftershock (EGF) are impulsive.

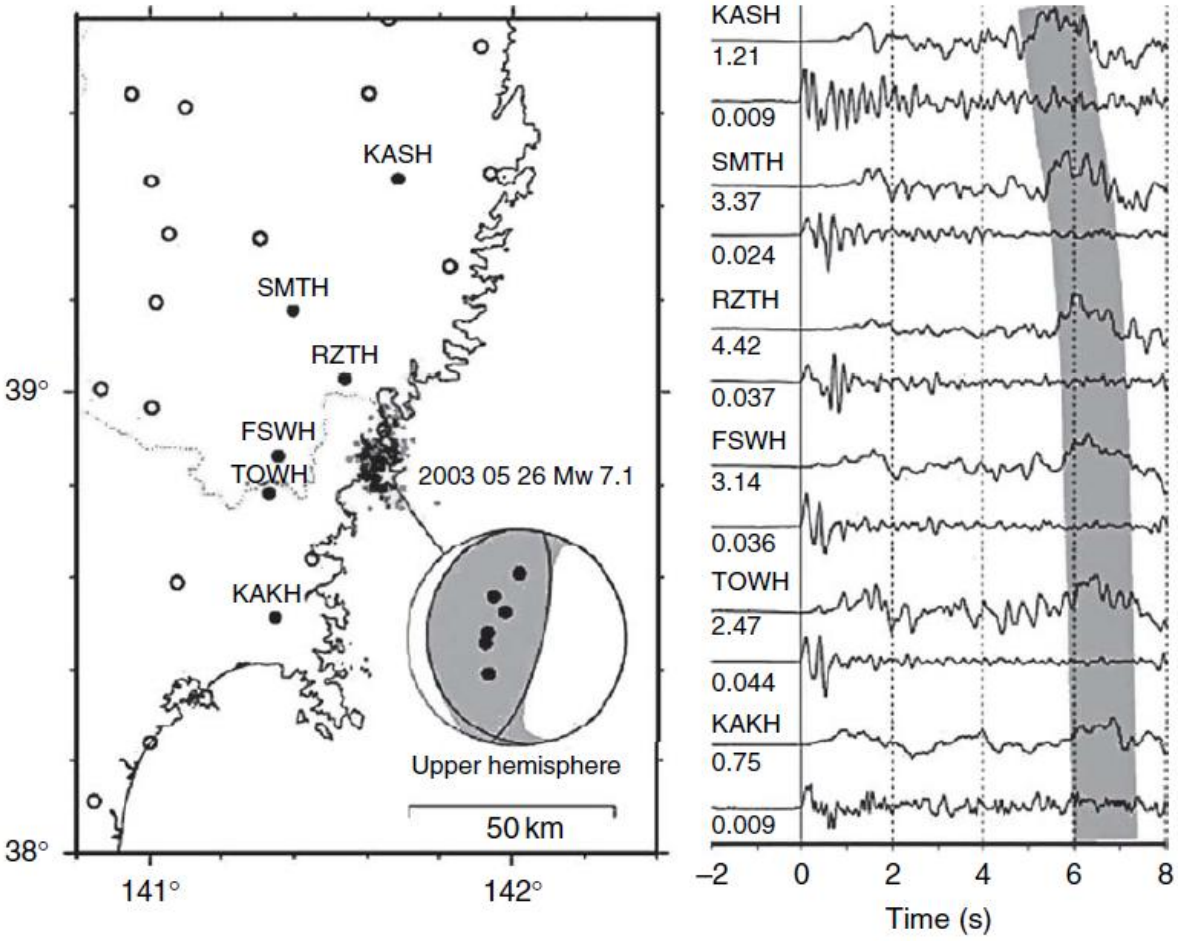

Figure 3.6. The waveforms of the 2003 Miyagi-Oki, Japan Earthquake M_w 7.1 and its aftershocks (impulsive) for 6 stations (Schubert, 2007).

Thus we can suppose the source time function of the aftershock as a Delta function $\boldsymbol{\delta}$ (idealized impulse) which represents a point source in physics ($X_a(t) = \delta(t)$).

We can confirm this approach by comparing the moment magnitudes (M_w) of the mainshock 7.1 and the aftershock event 6.0 (Clinton 2004) via Equation 3.12 which is moment magnitude equation of (Kanamori, 1977). Moment magnitude is directly related to seismic moment M_0 - a way of measuring the earthquake size (Figure 3.7) as given in Equation 3.11.

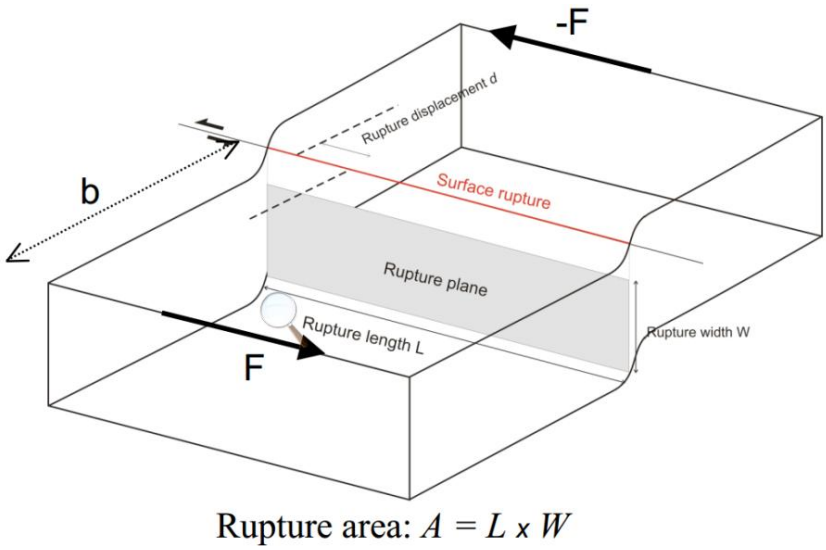

Figure 3.7. Earthquake size calculation.
(http://web.ics.purdue.edu/~ecalais/teaching/eas450/seismology4.pdf)

$$M_0 = 2 . b. F \tag{3.7}$$

$$\epsilon_{shear} = \frac{d}{2b} \tag{3.8}$$

$$\sigma_{shear} = \frac{F}{A} = \frac{F}{L . W} \tag{3.9}$$

$$\mu = \frac{\sigma_{shear}}{\epsilon_{shear}} = \frac{F/A}{d/2b} = \frac{2 . b . F}{d . A} = \frac{M_0}{d . A} \tag{3.10}$$

$$M_0 = \mu . A\bar{D} \equiv \mu . P \tag{3.11}$$

$$M_w = \frac{log\, M_0}{1.5} - 10.73 \tag{3.12}$$

Thus we obtain the size of the earthquake where μ is rigidity, A is the fault area L (length) x W (width), $\bar{D}$ is the mean displacement and P is the potency $P \equiv A.\bar{D}$. Equation

3.6 shows that the fault area of the mainshock approximately equals to 12 times the fault area of the aftershock event.

$$M_w = \frac{\log M_0}{1.5} - 10.73 \propto \log M_0 \propto \log P \propto \log A \,.\, \bar{D} \propto \log A^{3/2} \propto \frac{3}{2} \log A \qquad (3.13)$$

$$\frac{7.1}{6.0} = \frac{log\ A_{7.1}}{log\ A_{6.0}} \qquad (3.14)$$

The site, response and the radiation pattern effect are the same for both of the events because of the close focal mechanisms and locations. $U_a(t) \approx \boldsymbol{\delta}\ (t) * Q_a(t) * I_a(t) = Q_a(t) * I_a(t)$ since $\boldsymbol{\delta}\ (t) * f(t) = f(t)$ and thereby if we know the empirical Green's function which equals to $U_a(t)$, we can compute the solution of the source time function for main shock $X_m(t)$ via deconvolution in the time domain as given in Equaiton 3.5

$$U_m(t) \approx X_m(t) * U_a(t) \qquad (3.15)$$

or division in the frequency domain using Equation 3.16.

$$X_m(w) \approx U_m(w)/U_a(w) \qquad (3.16)$$

We can show the convolution as a serial product or a matrix multiplication by using the Toeplitz matrix where each diagonal is constant. So source time function can be deconvolved by linear matrix inversion Clinton (2004).

We used the iterative time domain deconvolution algorithm of (Ligorria and Ammon, 1999)-an application of the (Kikuchi and Kanamori, 1982) method -to estimate the source time functions. This algorithm is built on a least squares minimization. The convolution of empirical Green's function with the iteratively renewed Gaussian pulse summation gives us the synthetic signal. The amplitude and position of Gaussian pulses are determined by cross correlation of the mainshock and aftershock seismograms at each iteration (Ligorría, 2000). The pulse amplitude is proportional to the maximum cross correlation coefficient which is an indicator of the similarity between the two sets and its time offset which depends on the related time lag (Stich *et al*., 2005). ($\star$ symbol signifies

the correlation.) If $U_a(t)$ represents the aftershock and $U_m(t)$ represents the mainshock seismogram, then a cross correlation of these two seismograms is:

$$R_{xh}(\tau) = U_m(\tau) \star U_a(\tau) = \int_{-\infty}^{\infty} U_m(t)\, U_a(t+\tau)\, dt \tag{3.17}$$

Convolution of the initial guess of the source time function x(t) with aftershock $U_a(t)$ gives synthetic seismogram s(t).

$$s(t) = x(t) * U_a(t) \tag{3.18}$$

The iterative source time function $x_i(t)$ is x(t) unless the misfit fails under a predefined value. While generating the source time function $x_i(t)$, a sequence of Gaussian pulses with a time shift are summed. In the frequency domain, it is given by:

$$G(w) = e^{-\pi^2 f^2/\alpha^2} = e^{-w^2/(4\alpha^2)} \tag{3.19}$$

$$w = 2\,\pi\, f \tag{3.20}$$

$\alpha = 5 \rightarrow$ exp(-PI^2*(f/5)^2)

$\alpha = 2 \rightarrow$ exp(-PI^2*(f/2)^2)

$\alpha = 1 \rightarrow$ exp(-PI^2*(f/1)^2)

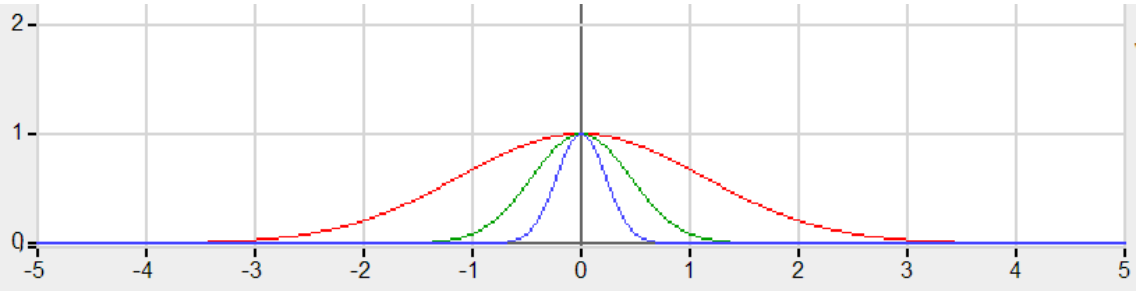

Figure 3.8. Comparison of Gaussian pulses according to parameter α.

Parameter α is the Gaussian width parameter which is related to bandwith of the signal as given in the Equation 3.19. As alpha parameter α gets larger the bandwidth also gets larger (Figure 3.8). Parameter alpha α is inportant for the resolution of the source time function and it controls the frequency content (Table 3.3).

Table 3.3. The frequency content according to parameter α.
(http://eqseis.geosc.psu.edu/~cammon/HTML/RftnDocs/seq01.html)

Value of alpha a	**Frequency (Hz) at which G(f)=0.1**	**Approximate pulse width (s)**
10	4.8301	0.50
7.5	3.6226	0.61
5	2.4151	0.75
2.5	1.2075	1.00
1.25	0.6038	1.50
1	0.4830	1.67
0.875	0.4226	1.78
0.75	0.3623	1.92
0.625	0.3019	2.10
0.5	0.2415	2.36
0.4	0.1932	2.64
0.3	0.1449	3.04
0.2	0.0966	3.73
0.1	0.0483	5.27

After each iteration, the synthetic seismogram s(t) is removed from the mainshock seismogram $U_m(t)$.

$$U_{m_d}(t) = U_m(t) - s(t) \tag{3.21}$$

Thus the primary event is elimnated. The $U_{m_d}(t)$ is substituted into the Equation 3.17 for the $U_m(t)$. This process continues to find the other amplitudes and spike delays and adds every pulse to the source time function and hence the misfit decreases. The iteration

stops when the decrease in misfit becomes unimportant. The scaled error ε can be calculated by using the weighted norm (Ligorría, 2000):

$$\varepsilon_j = \frac{\sum_i (s_i - \hat{s}_i)}{\sum_i (s_i)^2} \tag{3.22}$$

where j shows the iteration number.

$$\hat{s}(t) = x_i(t) * U_a(t) \tag{3.23}$$

$$100 \times (\varepsilon_{j-1} - \varepsilon_j) \tag{3.24}$$

$$\varepsilon_1 \equiv 1 \tag{3.25}$$

The Equation 3.24 gives us the misfit value. Iterative time domain deconvolution is not based on a regularization. This algorithm takes the crucial features initially, after that it brings out the other properties. It produces a causal source time function.

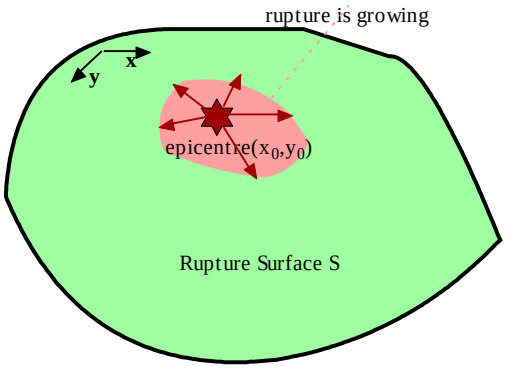

Figure 3.9. Model of the empirical Green's function method modified from Clinton (2004). Red star shows the epicentre of the earthquake.

$U^i(t)$ represents the observed vector displacement for the station i and $u^i(x, y, t)$ is the vector displacement at the station i as a result of dislocation on the fault at (x,y) cartesian co-ordinates along strike and plunge (Figure 3.9).

$$U_M^i(t) = \iint_S u^i(x,y,t)\, dS \tag{3.26}$$

$D(x,y,t)$ is the slip history at (x,y) cartesian co-ordinates and $G^i(x,y,t)$ is the Green's functions which is the displacement at the station i because of a unit step function dislocation on the fault at (x,y). Mainshock displacement is then given by the Equation 3.27 and if we write the surface S as length L and width W of the fault, we obtain the Equation 3.28.

$$U_M^i(t) = \iint_S \dot{D}_M(x,y,t) * G^i(x,y,t) dS \tag{3.27}$$

$$U_M^i(t) = \int_0^L \int_0^W \dot{D}_M\,(x,y,t) * G^i(x,y,t)\, dy\, dx \tag{3.28}$$

The Green's function at the point (x,y) given by Equation 3.29 and 3.30 is same as the shifted version of the Green's function at the epicentre (x_0, y_0) with a time delay of $T^i(x,y)$ which shows the travel time difference between the point (x,y) and the epicentre (x_0, y_0).

$$G^i(x,y,t) \approx G^i(x_0,y_0,t) * \delta(t - T^i(x,y)) \tag{3.29}$$

or

$$G^i(x,y,t) \approx G^i[x_0,y_0,t - T^i(x,y)] \tag{3.30}$$

Since the delta function $\boldsymbol{\delta}$ has the property of (Bracewell, 2000)

$$f(x) * \delta(x-a) = f(x-a) \tag{3.31}$$

If we put the Equation 3.29 into the Equation 3.27, then we get:

$$U_M^i(t) \approx \iint_S \dot{D}_M(x,y,t) * G^i(x_0,y_0,t) * \delta\left(t - T^i(x,y)\right) dS$$
$$\approx \iint_S \dot{D}_M\,[x_0,y_0,t - T^i(x,y)] * G^i(x_0,y_0,t)\,dS \quad (3.32)$$

$$U_M^i(t) \approx\ G^i(x_0,y_0,t) * F_M^i(t) \quad (3.33)$$

The source time function at the station i, $F_M^i(t)$ and the mainshock potency P_M are given in Equation 3.34 and Equation 3.35 respectively:

$$F_M^i(t) \equiv \iint_S \dot{D}_M\,[x_0,y_0,t - T^i(x,y)]\,dS \quad (3.34)$$

$$P_M \approx \int F_M^i(t)\,dt \quad (3.35)$$

On the other hand the duration of the aftershock source time function is too short, so it becomes a multiplication of a $\boldsymbol{\delta}$ function with the aftershock potency P_A.

$$U_A^i(t) \approx P_A\,G^i(\,x_0,y_0,t) \quad (3.36)$$

$$U_M^i(t) \approx\ G^i(x_0,y_0,t) * F_M^i(t) \approx [\frac{1}{P_A}]\,U_A^i(t) * F_M^i(t) \quad (3.37)$$

Thereby we obtained source time function at every station by deconvolving the aftershock event from mainshock event. In order to equalize the weights of the source time functions, we normalized them to unit area.

If we discretize the fault area into patches as shown in Figure 3.10 then we get the large event's ground motion $U_M(t)$ as a sum of each fault patch's motion as given in Equation 3.38 (Yang, 2009). In Equation 3.39 $u_{ij}(t)$ denotes the empirical Green's functions for small earthquakes. Thus the empirical Green's function summation approach gives us the large event's ground motion.

$$U_M(t) = \sum_{i=1}^{l}\sum_{j=l}^{m} U_{M_{ij}}(t) \quad (3.38)$$

$$U_M(t) = \sum_{i=1}^{l}\sum_{j=l}^{m} F_{ij}(t) * u_{ij}(t) \quad (3.39)$$

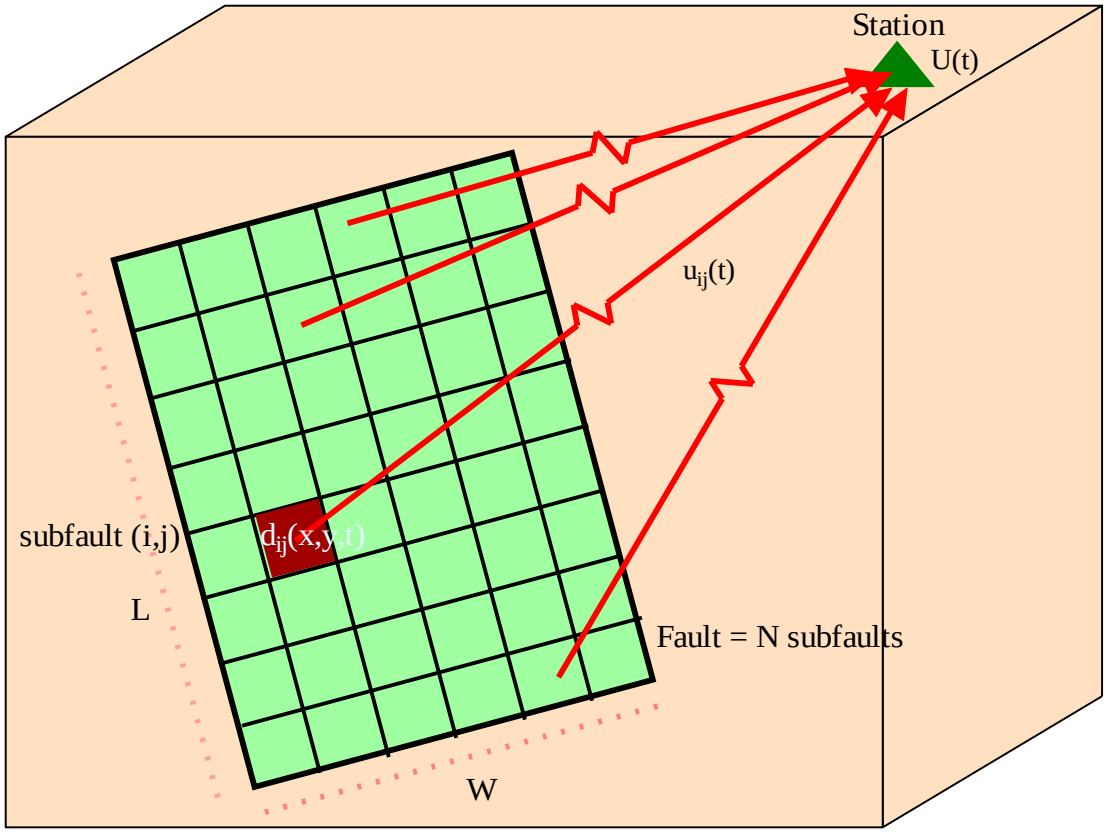

Figure 3.10. Model of the empirical Green's function method modified from Yang (2009). Red square shows the subfault on a rupture fault and green triangle shows a station.

3.4. A Brief History of Slip Inversion

Some large earthquakes have an importance in the history of slip inversion method (Schubert, 2007). The first studied earthquake was 22 May 1960, Chielan Earthquake M_w 9.5 which is the largest earthquake in the world so far. Fault length of the Chilean Earthquake was 1000 km and rupture velocity was between 3 and 4 km/s (Benioff *et al.*, 1961; Press *et al.*, 1961). A finite fault model which is called Haskell model was

introduced in 1960s. This model shows the unidirectional rupture propagation along a rectangular fault with a constant rupture velocity and rise time which is rational for strike-slip faults (Aki and Richards, 2002; Haskell, 1964, 1969).

June 28, 1966 Parkfield M 6.0 Earthquake which is one of the well studied earthquakes showed that the earthquake source can be represented with a dislocatiion propagation (Aki, 1968). Kanamori and Anderson (1975) formulated empirical relations for large earthquakes on the basis of a constant stress drop.

Trifunac (1974) calculated slip on each subfault for 9 February 1971, San Fernando Earthquake via least squares method and thus he resolved the inversion problem first time. February 4, 1976 Guatemala Earthquake which involves 10 different pulses was proof of not all the earthquakes have a simple rupture (Kanamori and Stewart, 1978; Kikuchi and Kanamori, 1982; Kikuchi and Kanamori, 1991) as seen in Figure 3.11.

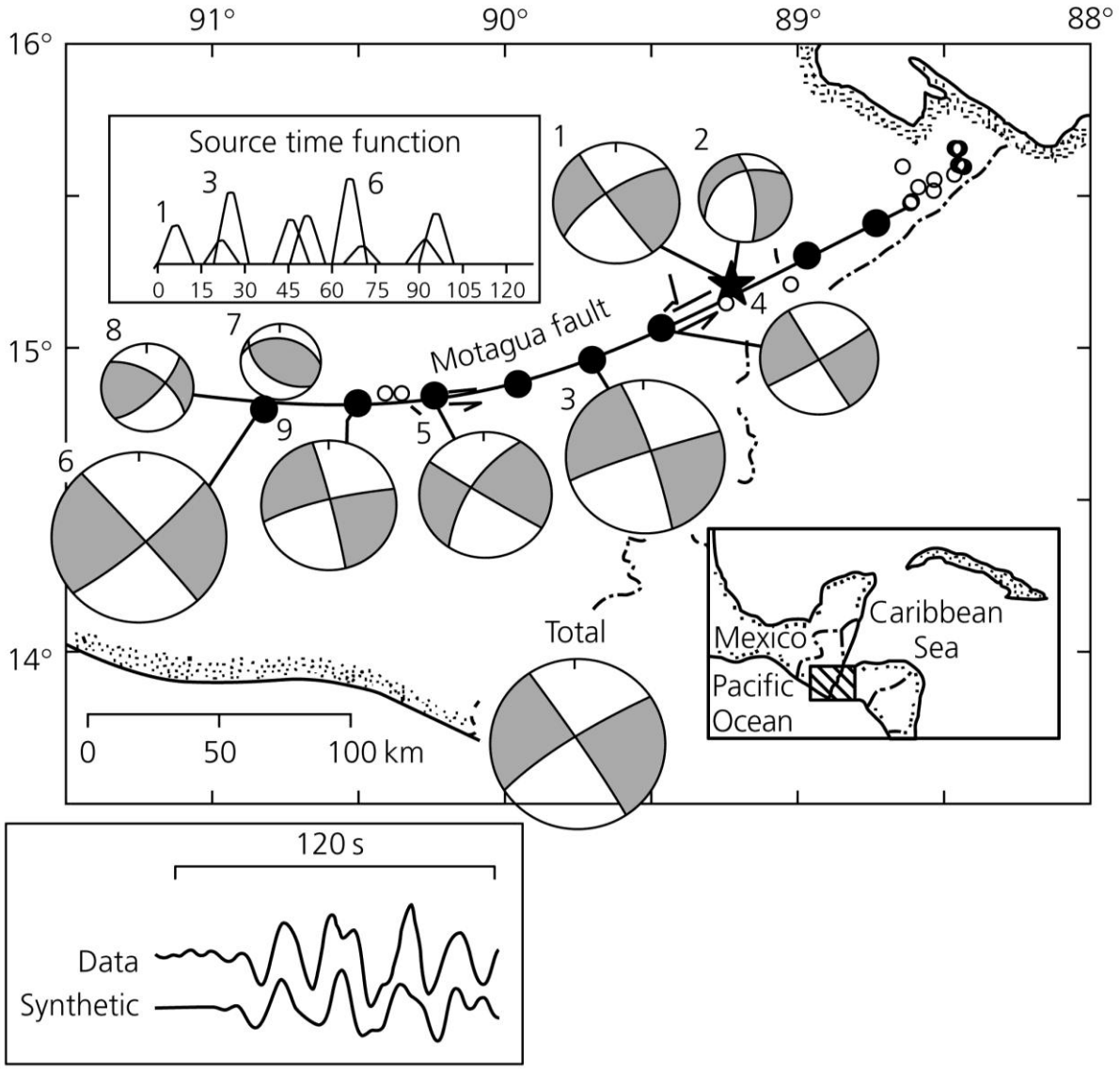

Figure 3.11. Location and focal mechanisms which are proportional to seismic moment of subevents for 1976 Guatemala Earthquake (Kikuchi and Kanamori, 1991).

The 15 October 1979 Imperial Valley Earthquake with M_w 6.4 was slip modeled by various groups which gave the opportunity to compare the models (Archuleta, 1984; Hartzell and Heaton, 1983; Olson and Apsel, 1982). The M_w 7.5 1999 Chi-Chi, Taiwan Earthquake was one of the best recorded and slip modeled earthquakes due to its dense station coverage (Ma *et al*., 2001).

Other important earthquakes which are well-studied on slip inversion are the 1989 Loma Prieta, California, M 6.9 Earthquake (Beroza, 1991; Liu and Archuleta, 2004; Steidl

et al., 1991; Wald *et al*., 1991), 26 June 1992 Landers Earthquake M_w 7.2 (Wald and Heaton, 1994) (Figure 3.17.a), 17 January1994 Northridge Earthquake M_w 6.7 (Hartzell *et al*., 1996; Wald *et al*., 1996). 17 January 1995 Hyogoken-Nanbu, Kobe Japan Earthquake M_w 6.9 and 10 June 2000 Tottori, Japan Earthquake M_w 6.7 are similar in size. 2000 Tottori Earthquake took place on a left lateral strike slip fault which was unknown before (Semmane *et al*., 2005) while Kobe Japan Earthquake occurred on a right lateral strike slip fault. Figure 3.12 shows kinematic source models of some famous earthquakes.

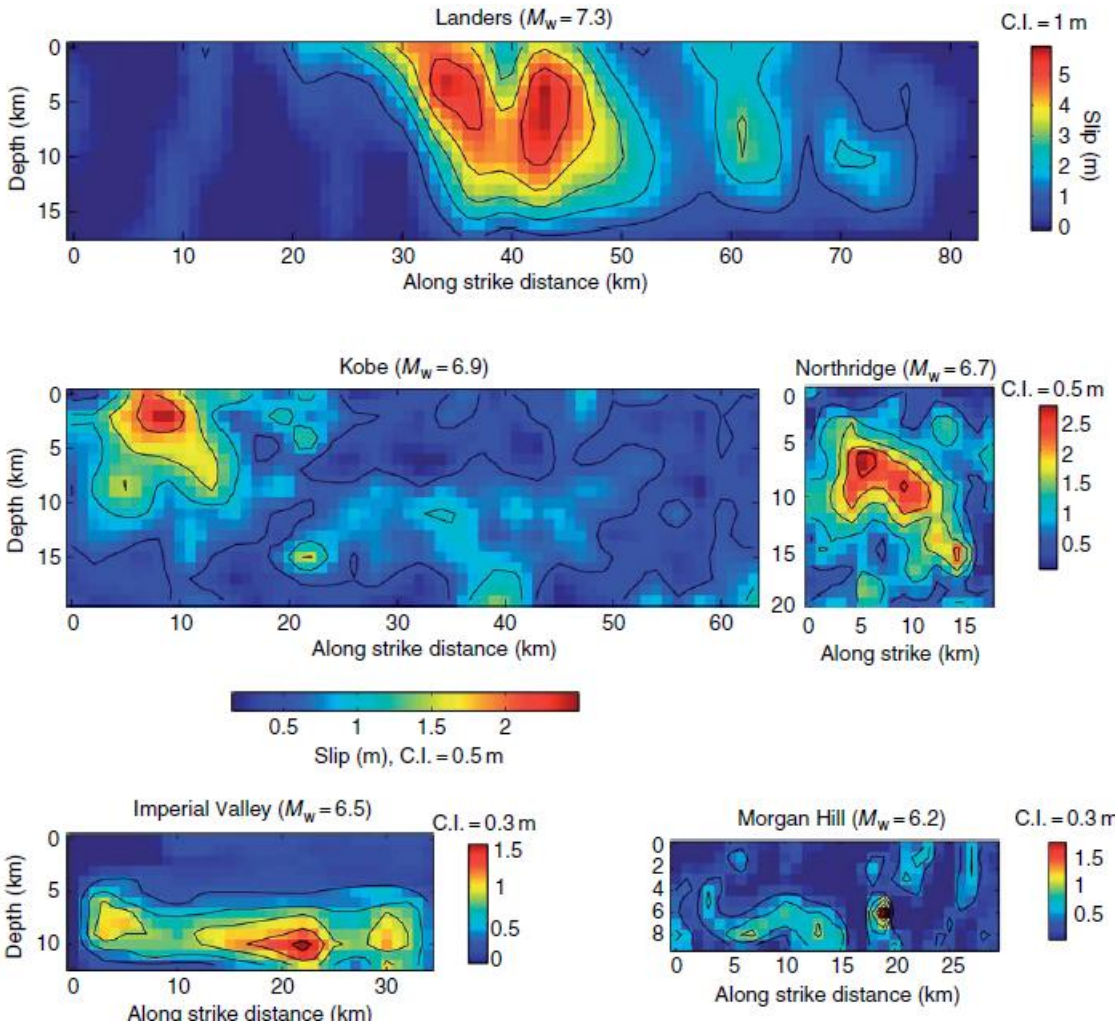

.

Figure 3.12. Kinematic source models for the 1992 Landers Earthquake, 1995 Kobe Earthquake, 1994 Northridge Earthquake, 1979 Imperial Valley Earthquake and 1984 Morgan Hill Earthquake (Schubert, 2007).

3.5. The Inversion of Source Time Functions

The shapes of the STFs varying with the azimuth of the stations were mapped into the spatial evolution of slip on the fault plane. We used the inversion method of (Dreger, 1994) where source time functions are modelled to obtain slip distribution on the fault plane with constant rupture velocity and rise time using a linear least squares inversion with positivity constraint. In order to obtain the best fit rupture parameters, we have performed a grid search over rupture velocity and rise time.

In order to construct slip models, we need source parameters such as hypocenter coordinates (latitude, longitude and depth), size of the rupture surface (length and width) and the fault orientations such as dip and strike (Schubert, 2007). In our study, each subfault $1\ km\ \times 1\ km$ along strike of 241° and dip of 51°. We take the fault length (L) and width (W) as 90 km and 70 km, respectively, so the total number of subfaults is 6300. For each inversion the rise time T_D and the rupture velocity V_R are fixed. We compared the inversion results according to variance reductions and found the optimal values for V_R and T_D as well as the slip distribution.

The summation of the product of each subfault's source time function B_j and the weight w_j equals to D_i which is the source time function at the station i as given in Equation 3.41 (Dreger, 1994). N denotes the number of subfaults and time delay T is:

$$T_{ij} = \frac{R_{ij}}{V} \tag{3.40}$$

where V is the wave speed and R_{ij} is the distance between the i-th station and the j-th subfault.

$$D_i(t) = STF_i(t) = \sum_{j}^{N} B_j\left(t - T_{ij}\right)\ w_j\ = \sum_{j}^{N} \delta\left(t - T_{ij}\right) * B_j(t)\ w_j \tag{3.41}$$

In matrix form, it can be written as $G\ m\ = d$ where d is the data vector and shows the observed source time functions; G is the forward operator containing the STFs with the

time delays; m is the model vector consisting of the unknowns namely weights of all subfaults. A stable solution requires the use of some constraints. We impose two constraints 1) a positivity constraint which means no backward slip is allowed 2) a spatial derivative minimization constraint which smoothens the slip model. L shows a matrix of second spatial derivatives (Laplacian) and λ is a constant which shows how strong the smoothing equation is. The nonnegative least squares method of (Lawson and Hanson, 1974) (it provides the positivity constraint thus the solution vector has nonnegative elements and prohibits backward slips) with a smoothing operator is applied to find the slip weight vector w (Dreger, 1994).

$$\left|\frac{B}{\lambda L}\right| w = \left|\frac{D}{0}\right| \tag{3.42}$$

First, we have determined the smoothing constant $\lambda = 100$ in our inversion process by trial and error (Figure 3.15). This was the smallest weight that generated a smooth model which has approximately maximum fit to data. It is compared by variance reduction formula in the Equation 3.38 (Dreger 2002) where d is data and s is synthetic time series. Moreover, if $\lambda = 0$ then this means there is no smoothing.

$$VR = \left[1 - \frac{\sum_i (d_i - s_i)^2}{\sum_i (d_i)^2}\right] \cdot 100 \tag{3.43}$$

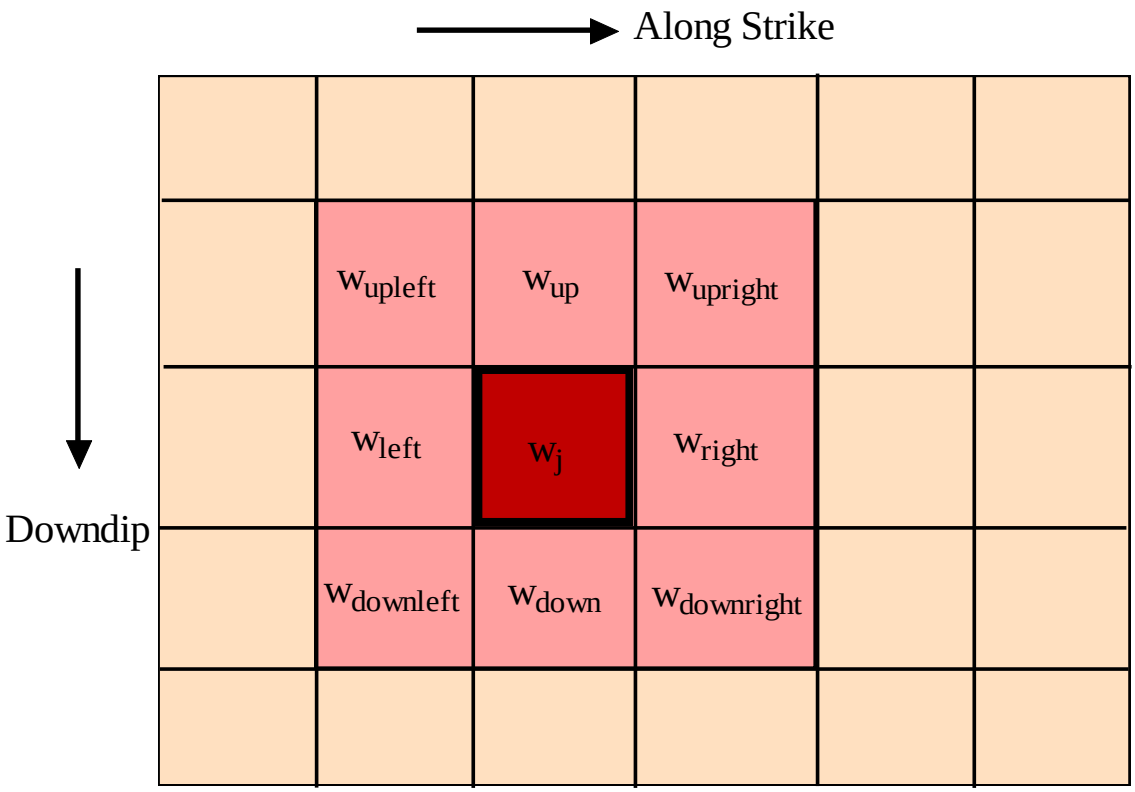

Figure 3.13. 2D Laplacian smoothing model modified from (Shear, 1999).

Laplacian operator is as follows:

$$\nabla_j^2 = \frac{1}{\Delta x^2}[w_{left} + w_{right} - 4w_j + w_{up} + w_{down}] \tag{3.44}$$

Laplacian of the jth point in a 2D model is given by (Figure 3.13) (Shear, 1999):

$$\nabla_j^2 \simeq \frac{1}{4}(w_{left} + w_{right} + w_{up} + w_{down}) - w_j \tag{3.45}$$

However we used a specific Laplacian in our process:

$$\begin{aligned}\nabla_j^2 \simeq \frac{1}{8}(&w_{left} + w_{right} + w_{up} + w_{down} + w_{upright} \\ &+ w_{upleft} + w_{downright} + w_{downleft}) \\ &- w_j\end{aligned} \tag{3.46}$$

We are searching for the model m which minimizes L_2 norm of the misfit function Φ.

$$\Phi = \|(d - Gm)\|_2 \tag{3.47}$$

The roughness **p** is the average 2nd order finite difference sum of the N number of patches and is given by:

$$p = \frac{\sum_i |p_i|}{2N} \tag{3.48}$$

where p=D m.

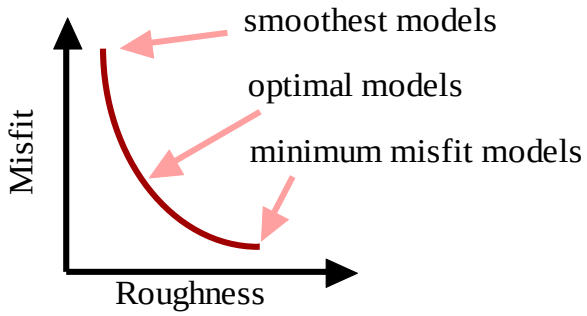

Figure 3.14. Graph of model roughness and misfit modified from (Shear, 1999).

It can be inferred from the tradeoff curve above -which shows the data misfit and the model roughness- that if data fit is poor, smoothest models can be possible (as $\lambda \to \infty$) (Figure 3.14). On the other hand, minimizing the misfit to low values *i.e.* good data fit results in high model roughness with complex solutions (as $\lambda \to 0$). Optimal models are in the corner of the curve, since there is a quite smooth model with good fittings to the data. This method is time consuming, subjective and challenging (Shear, 1999).

The integral of the each source time function has to be fixed and proportional to scalar seismic moment M_0. By using the fault slip weight vector w which is proportional to slip, we computed the slip (Dreger, 1994). For rupture velocity $V_R = 2.0\ km/s$ and rise time $T_D = 1.0\ s$, we found the maximum slip as 3.5 m.

$$slip_j = \frac{M_0\, w_j}{A\, \mu}$$

$$= \frac{6.4\ 10^{26}(dyne.cm)}{3\ 10^{11}\,(dyne/cm^2)\ \ 10^{10}(cm^2)}\ \ w_j \tag{3.49}$$

$$= 2133\ 10^{2}(cm)\, w_j = 2133\ (m)\ \ w_j$$

$$\sum_{j}^{N} w_j = 1 \tag{3.50}$$

We have obtained kinematic rupture models of M_w 7.1 Van Earthquake for both regional and teleseismic distance. It is called kinematic because slip models give the time history of a rupture but does not contain the full physics such as stress at each point on the fault, or the friction law on the fault (Schubert, 2007).

Finally the model of source was tested by evaluating the difference between the original source time functions and the synthetic source time functions using L_2-norm which were predicted from the model by forward modeling.

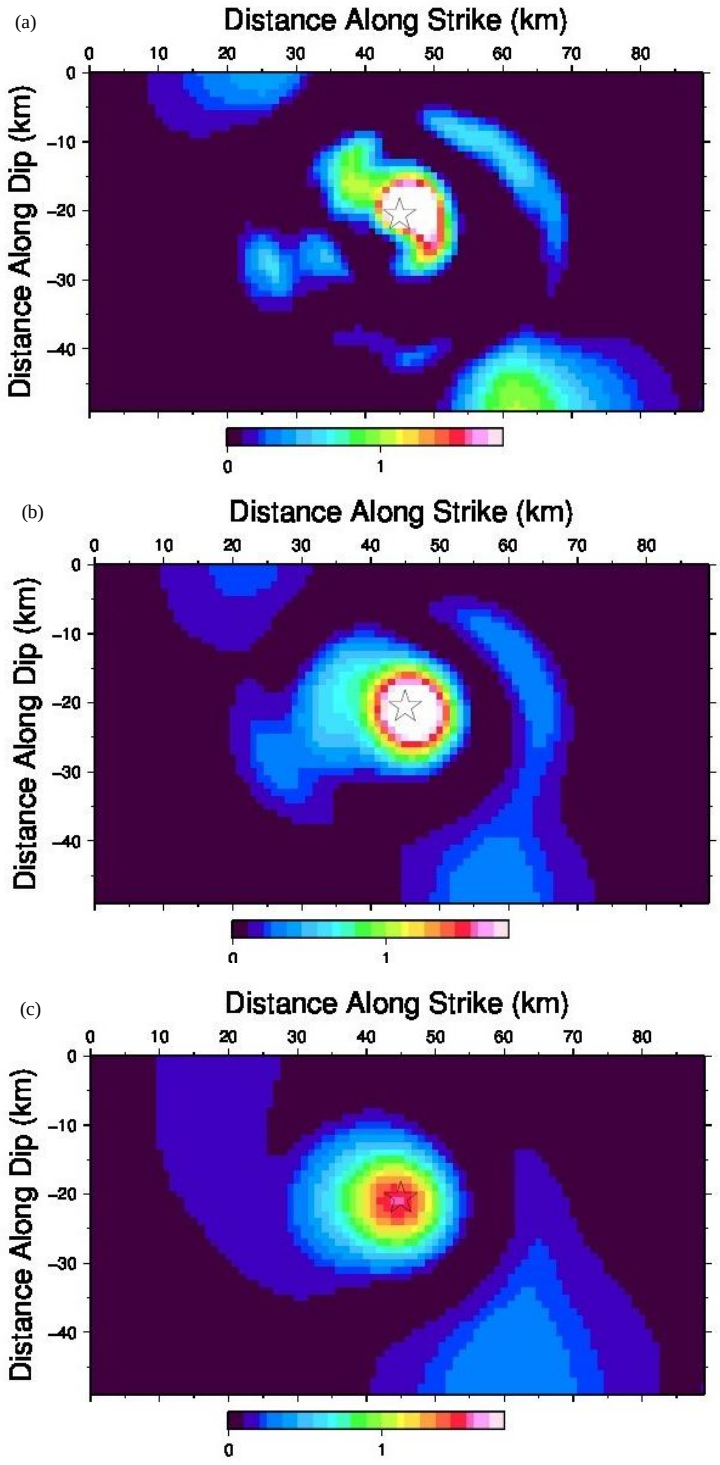

Figure 3.15. Comparison of smoothing constants and variance reductions for same rise time and rupture velocity (a) $\lambda = 10,\ VR = 82.643\ \%;$ (b) $\lambda = 100,\ VR = 79.706\ \%;$ (c) $\lambda = 300,\ VR = 73.479\ \%.$

4. RESULTS

The essential part of this study is to constrain the rupture velocity, rise time and slip distribution, independently from two distance ranges of seismic data; regional and teleseismic. Afterwards we join these two datasets to improve resolution and obtain a better constraint spatiotemporal model of the Van Earthquake.

Figure 4.1 shows the mainshock and aftershock events with source time functions at various azimuth-distance stations. The amplitude is different in all directions because of different rupture times known as "directionality affect". Toward the southwest, source time function has a shorter duration and higher amplitude. On the other hand, toward the northeast the duration of the source time function is longer and the amplitude is lower. Thus we can conclude that the rupture is propagating in the direction of southwest.

Figure 4.2.a shows the variance reduction for different values of rupture velocity and rise time using the regional STF's only. The grid search shows a clear peak around rupture velocity of 1.5-2 km/s and rise time of 1-2 seconds. Figure 4.2.b and 4.2.c show two end member slip models in the best-fitting range of rupture velocity and rise time with their fits to the data.

The results of the grid search for the teleseismic data is shown in Figure 4.3. Figure 4.3.a shows the grid search of the rupture velocity and rise time and associated variance reduction. The results from regional data are consistent with those obtained from teleseismic STF's. The best-fit range of rupture velocity is 1.5-2 km/s and best-fit range for rise time is 1-2 seconds.

Since the results for the best-fit range of rupture velocity and rise time are consistent from these datasets, the joint model of the regional and teleseismic data show similar peaks for the variance reduction with best-fit rupture velocity around 1.5-2 km/s and best-fit range for rise time between 1 to 2 seconds (Figure 4.4.a). The slip is primarily updip toward the southwest (Figure 4.4.c).

Figures from 4.5 to 4.10 show the slip models and the associated fits using the regional, teleseismic, and joint (both regional and teleseismic data) for various rupture velocities and rise time values which are in the range of plausible solutions based on the grid search results of Figures 4.2.a, 4.3.a. 4.4.a. These figures show that the results obtained from teleseismic distances are quite similar to the ones that are obtained from regional distances.

The maximum slip is about 3-3.5 meters. Most of the slip is concentrated around the hypocenter with propagation primarily toward southwest.

The azimuthal distribution of stations was not homogeneous and at some azimuths there was not any high S/N records and so we eliminated them from analysis. These azimuth ranges are 100°-120°, 140°-160° and 190°-220°.

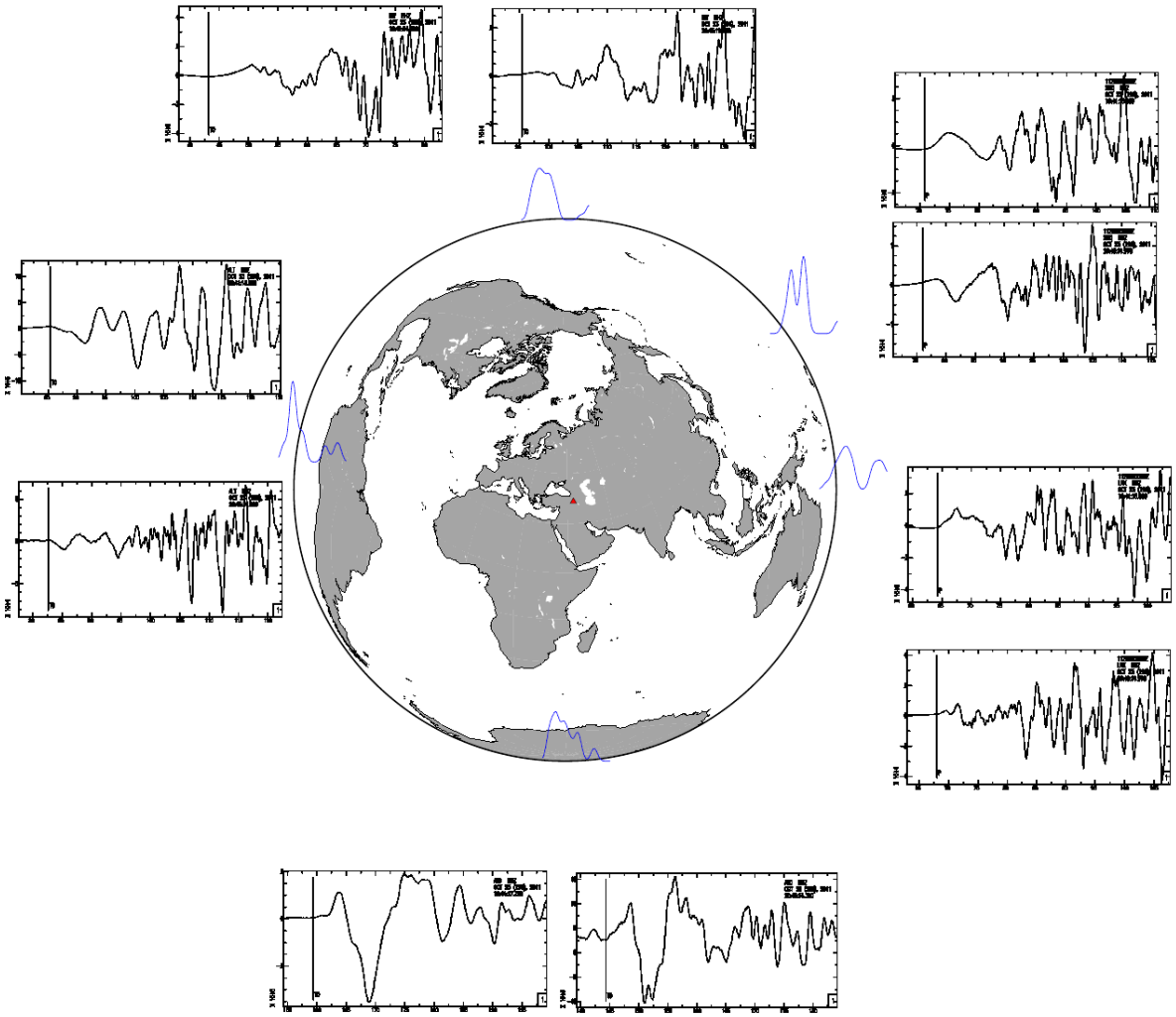

Figure 4.1. The P waveforms from the mainshock and the EGF aftershock (boxes) with source time functions (blue traces) obtained from deconvolution of two waveforms.

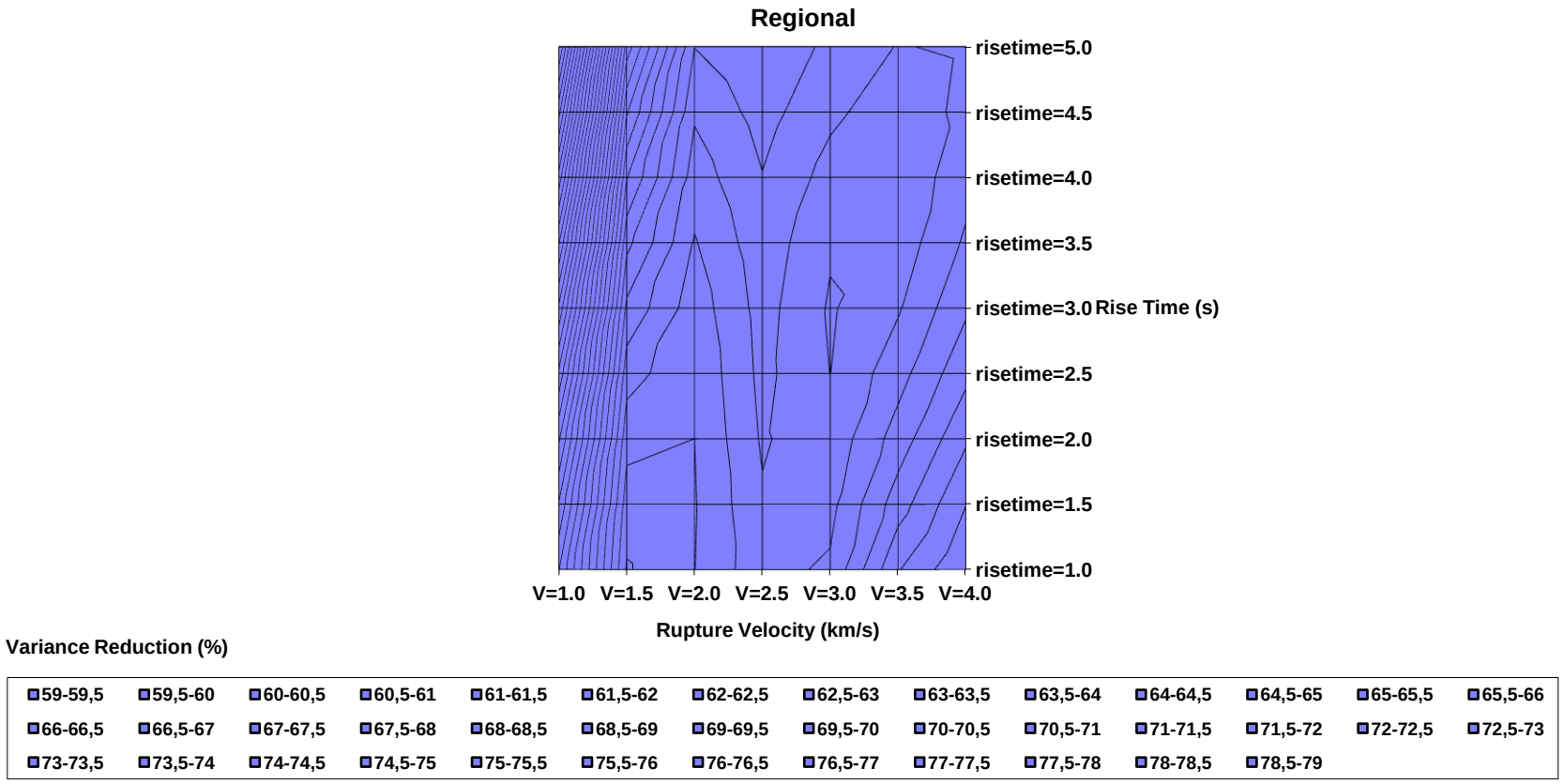

Figure 4.2.a. Variance reduction with rupture velocity and rise time for regional data.

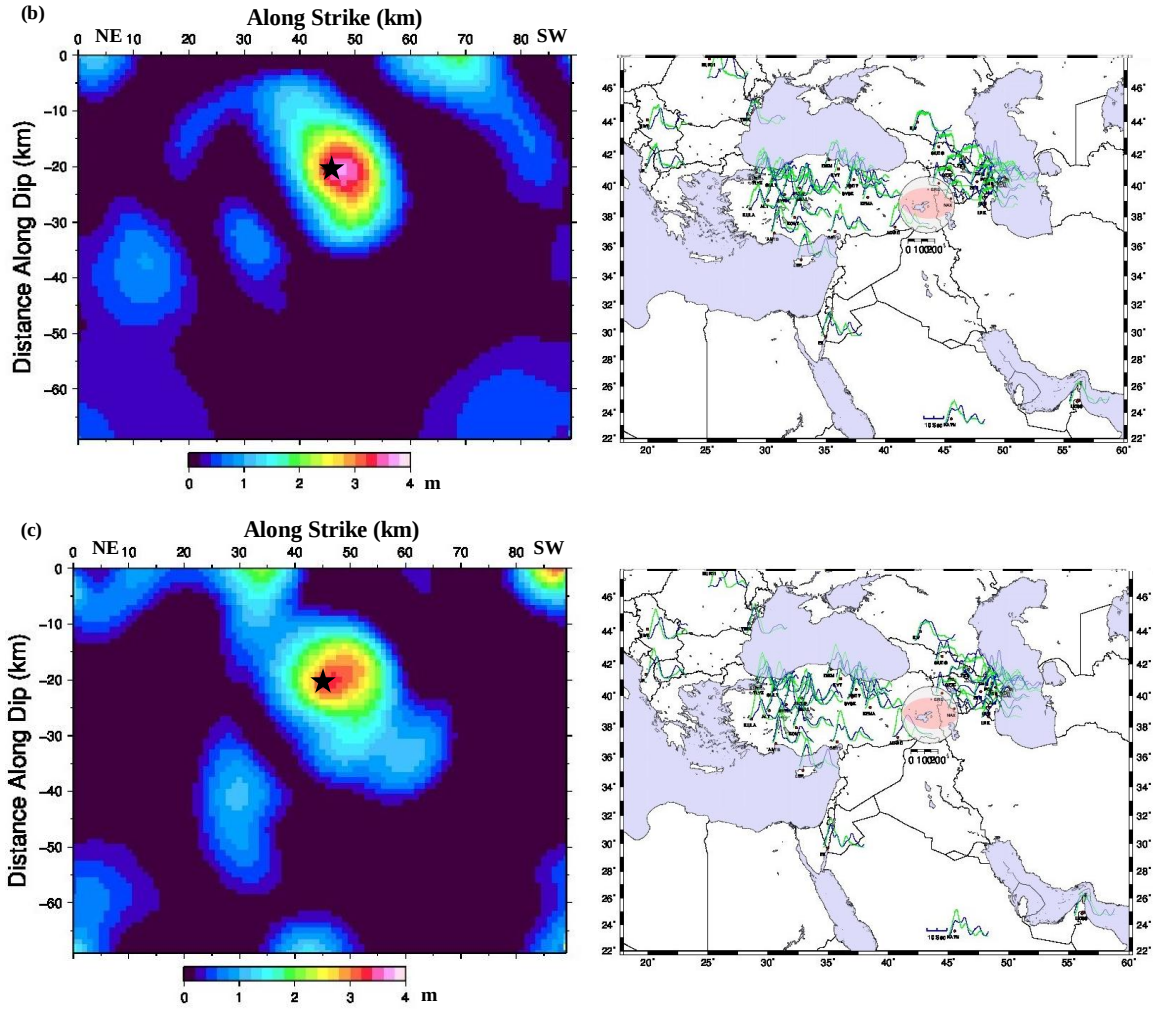

Figure 4.2. Comparison of original and synthetic STFs and the slip model inverted from regional data (b) Rupture Velocity $V_R = 1.5\ km/s$; rise time $T_D = 1.0\ s$ (c) Rupture Velocity $V_R = 2.0\ km/s$; rise time $T_D = 2.0\ s$.

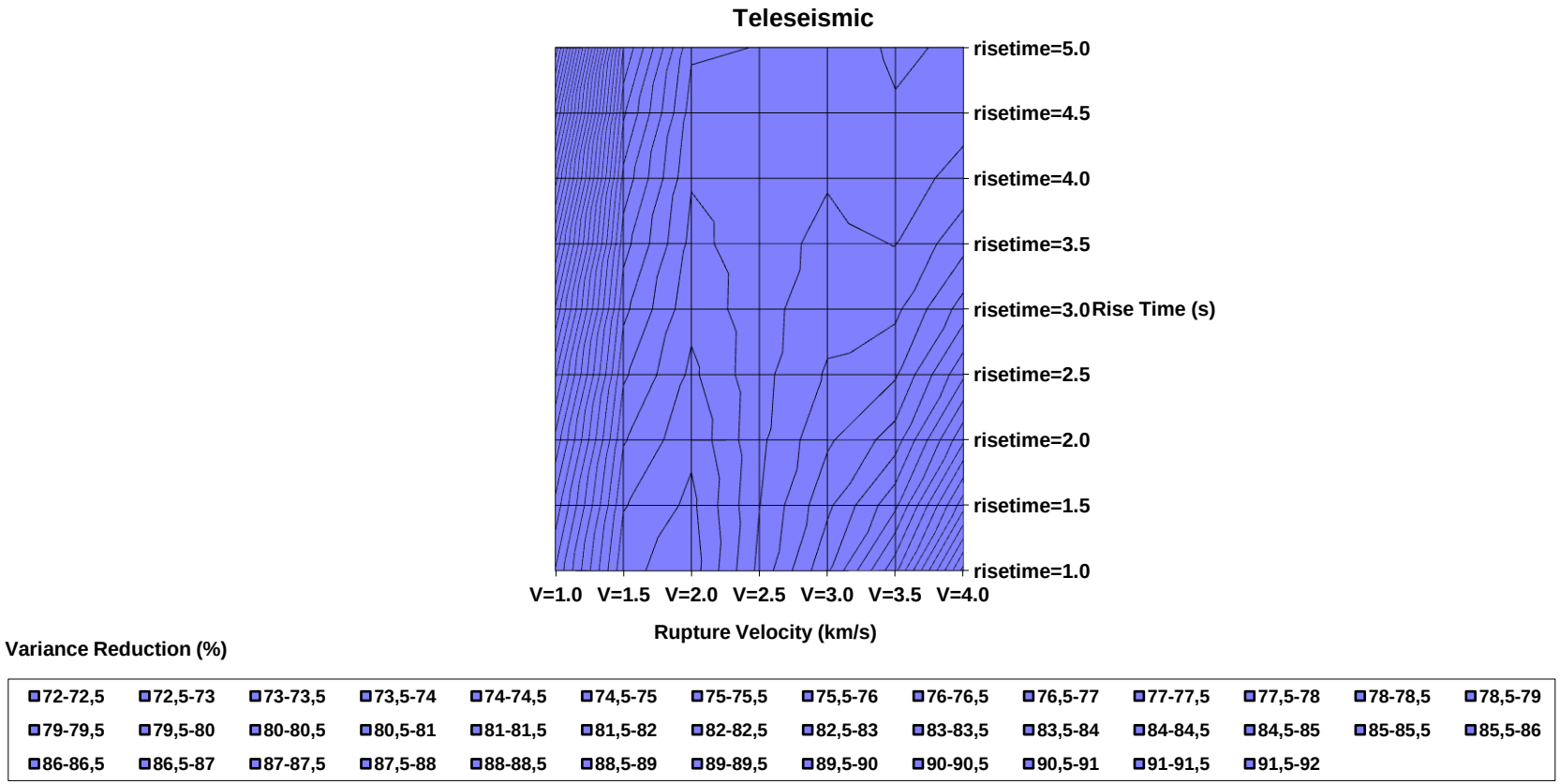

Figure 4.3.a Variance reduction with rupture velocity and rise time for teleseismic data.

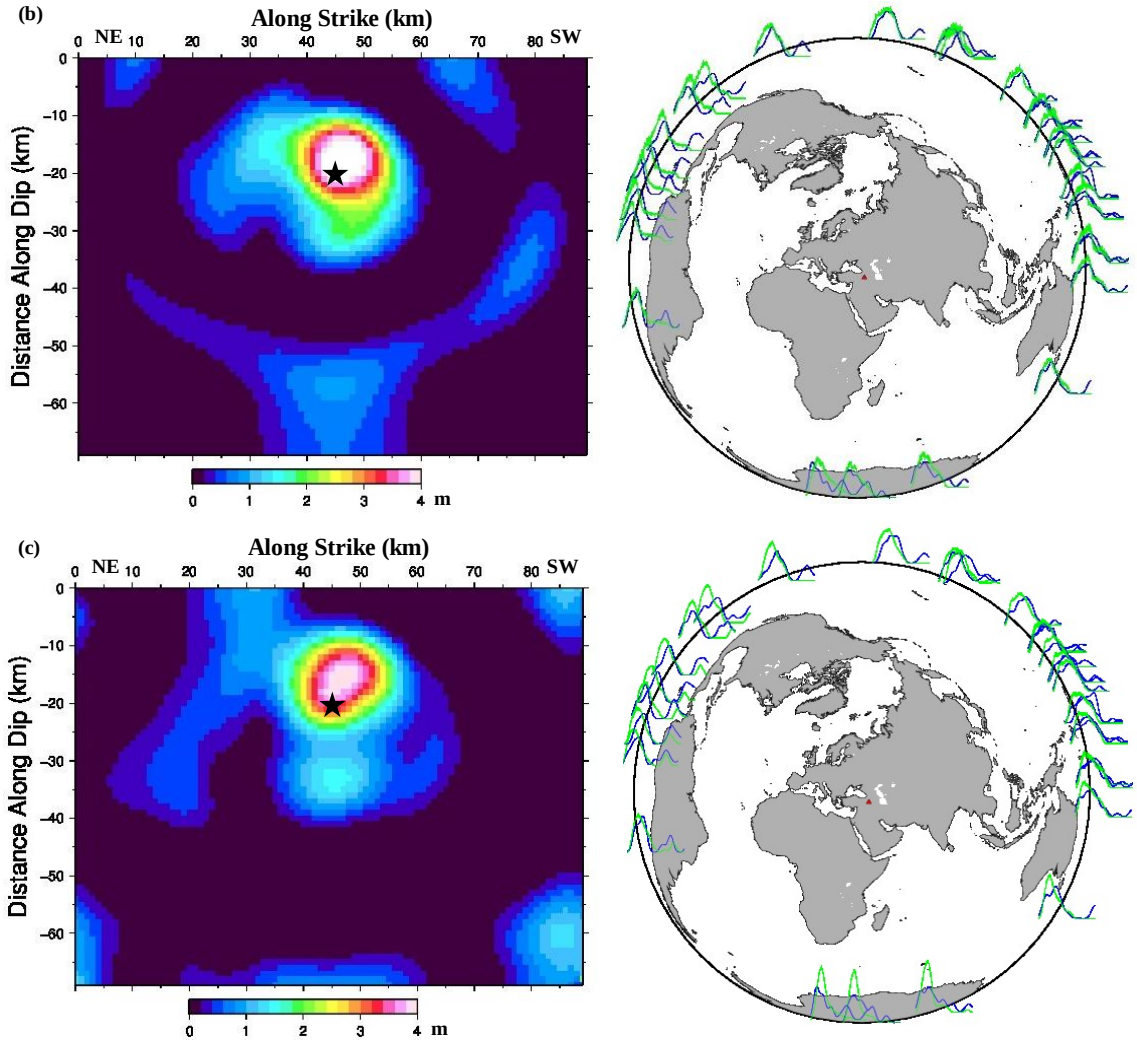

Figure 4.3. Comparison of original and synthetic STFs and the slip model inverted from teleseismic data (b) Rupture Velocity $V_R = 1.5\ km/s$; rise time $T_D = 1.0\ s$ (c) Rupture Velocity $V_R = 2.0\ km/s$; rise time $T_D = 2.0\ s$.

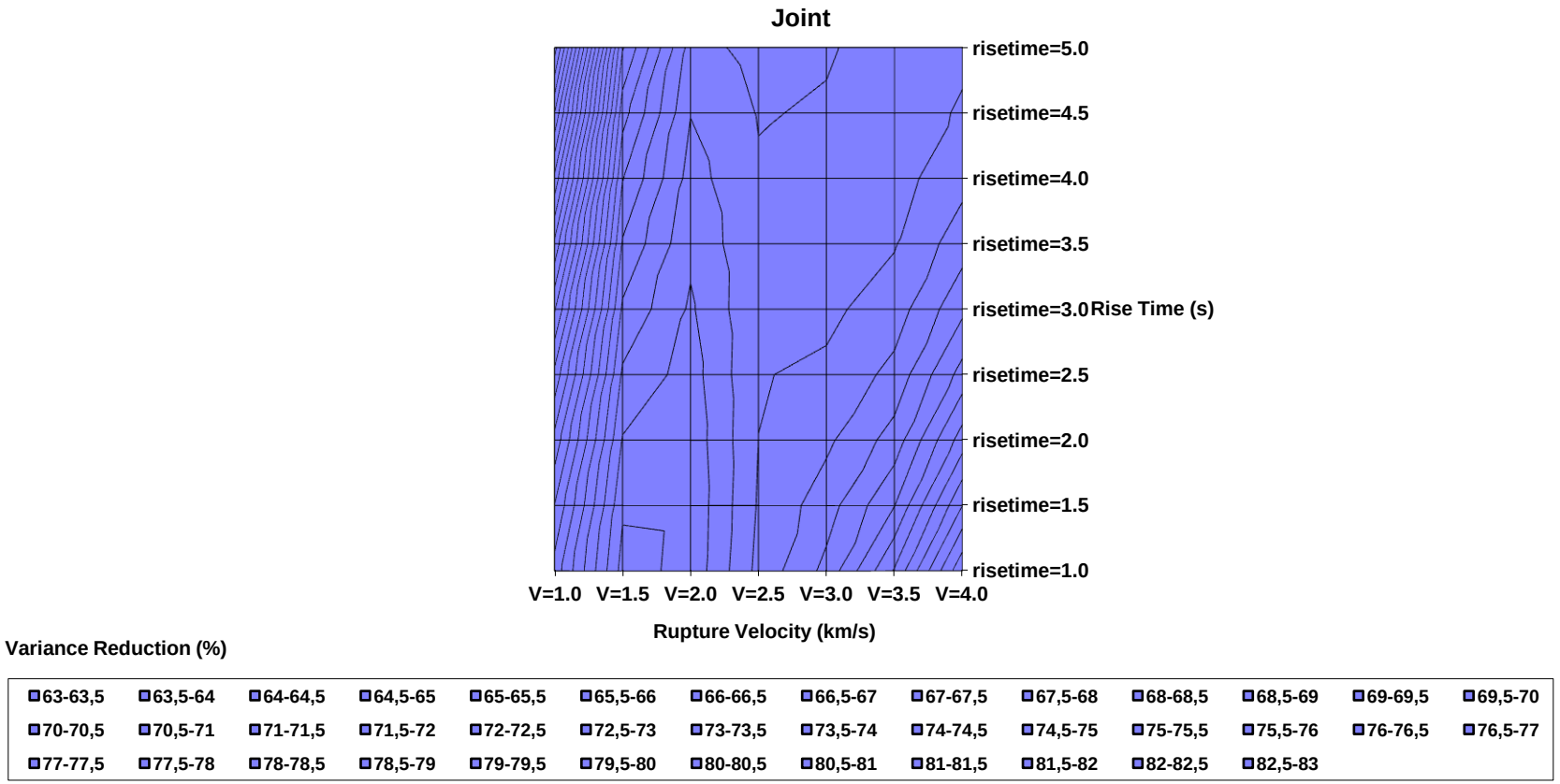

Figure 4.4.a. Variance reduction with rupture velocity and rise time for joint data.

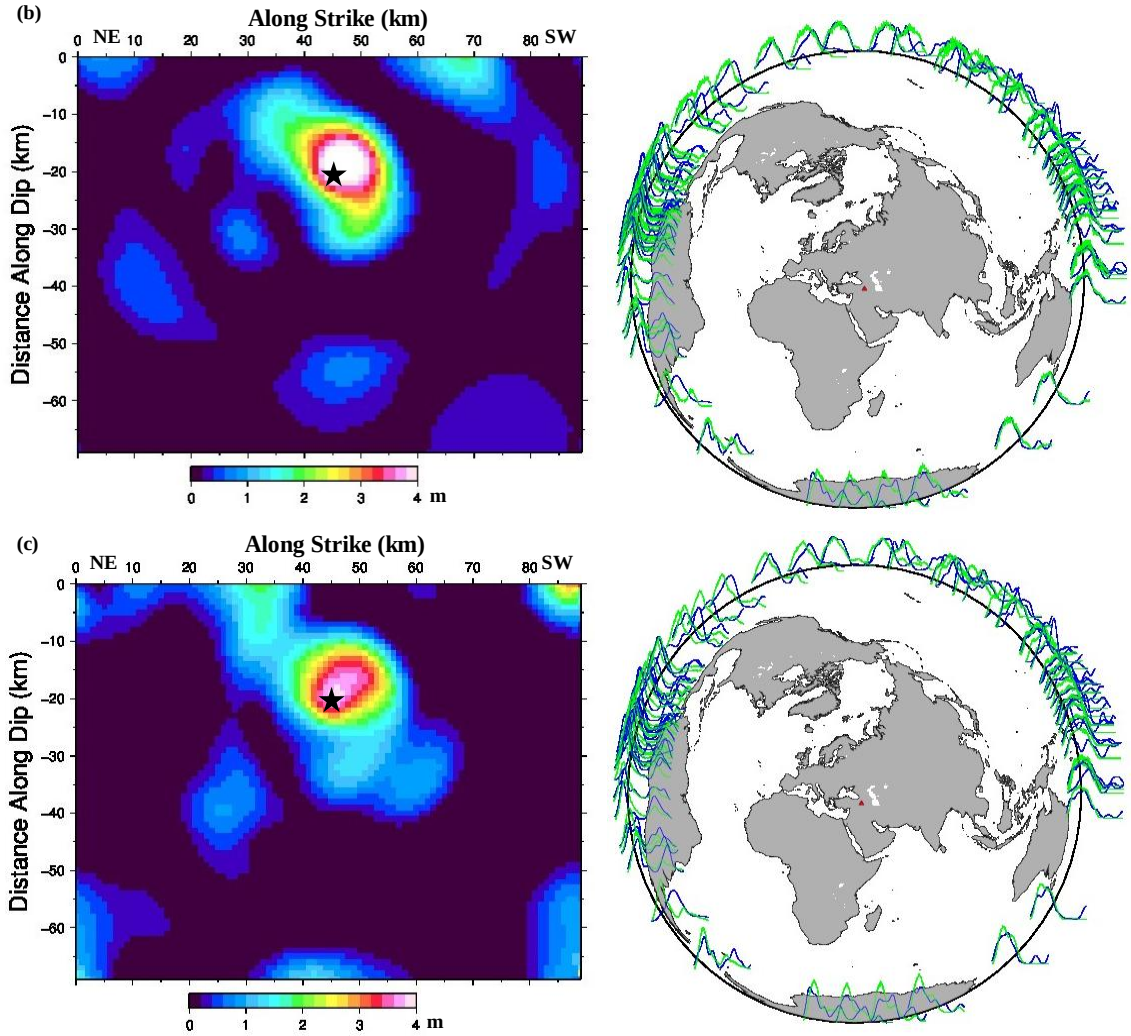

Figure 4.4. Comparison of original and synthetic STFs and the slip model inverted from joint data (b) Rupture Velocity $V_R = 1.5\ km/s$; rise time $T_D = 1.0\ s$ (c) Rupture Velocity $V_R = 2.0\ km/s$; rise time $T_D = 2.0\ s$.

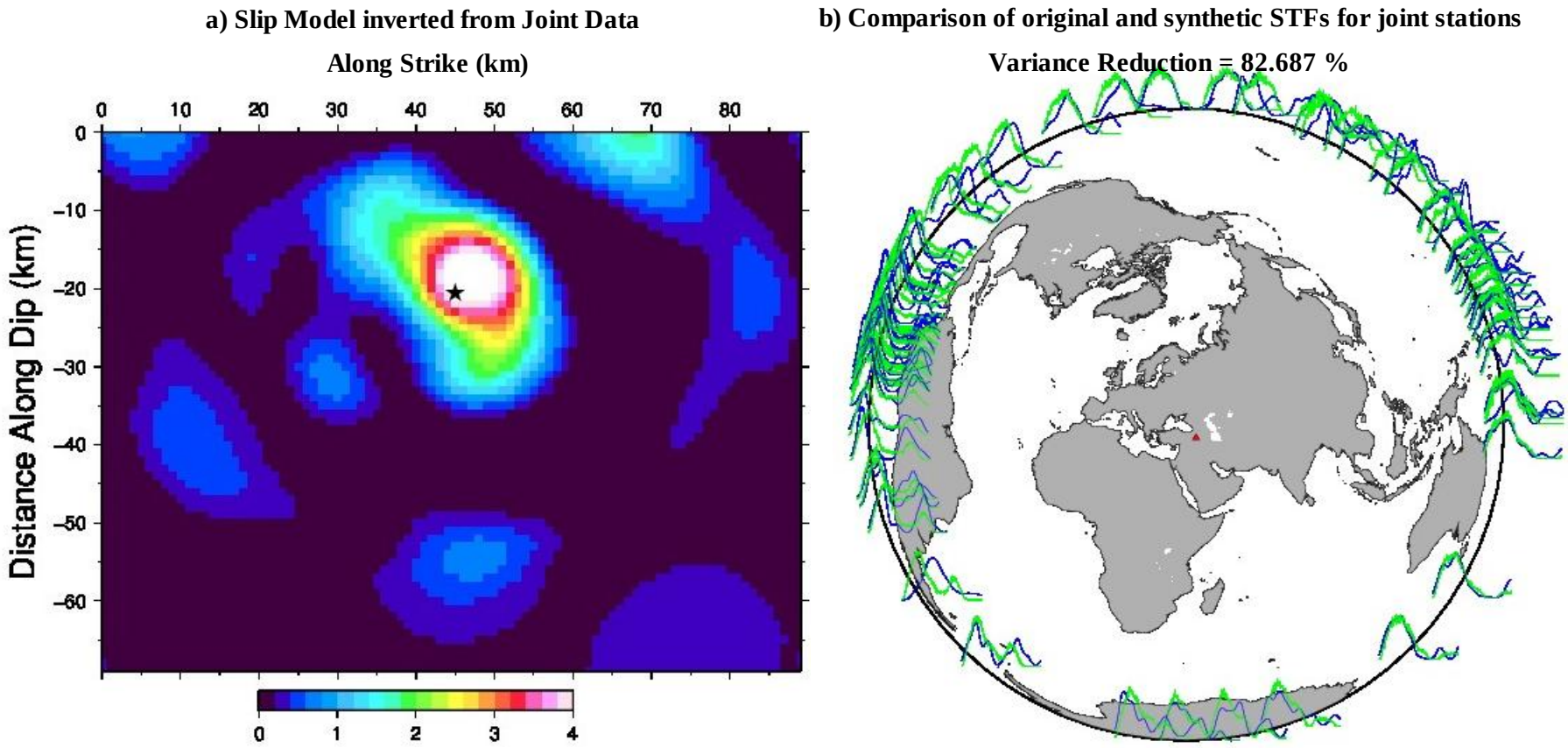

Figure 4.5. (a) Comparison of original and synthetic STFs and (b) the slip model inverted from joint data Rupture Velocity $V_R = 1.5\ km/s$; rise time $T_D = 1.0\ s$.

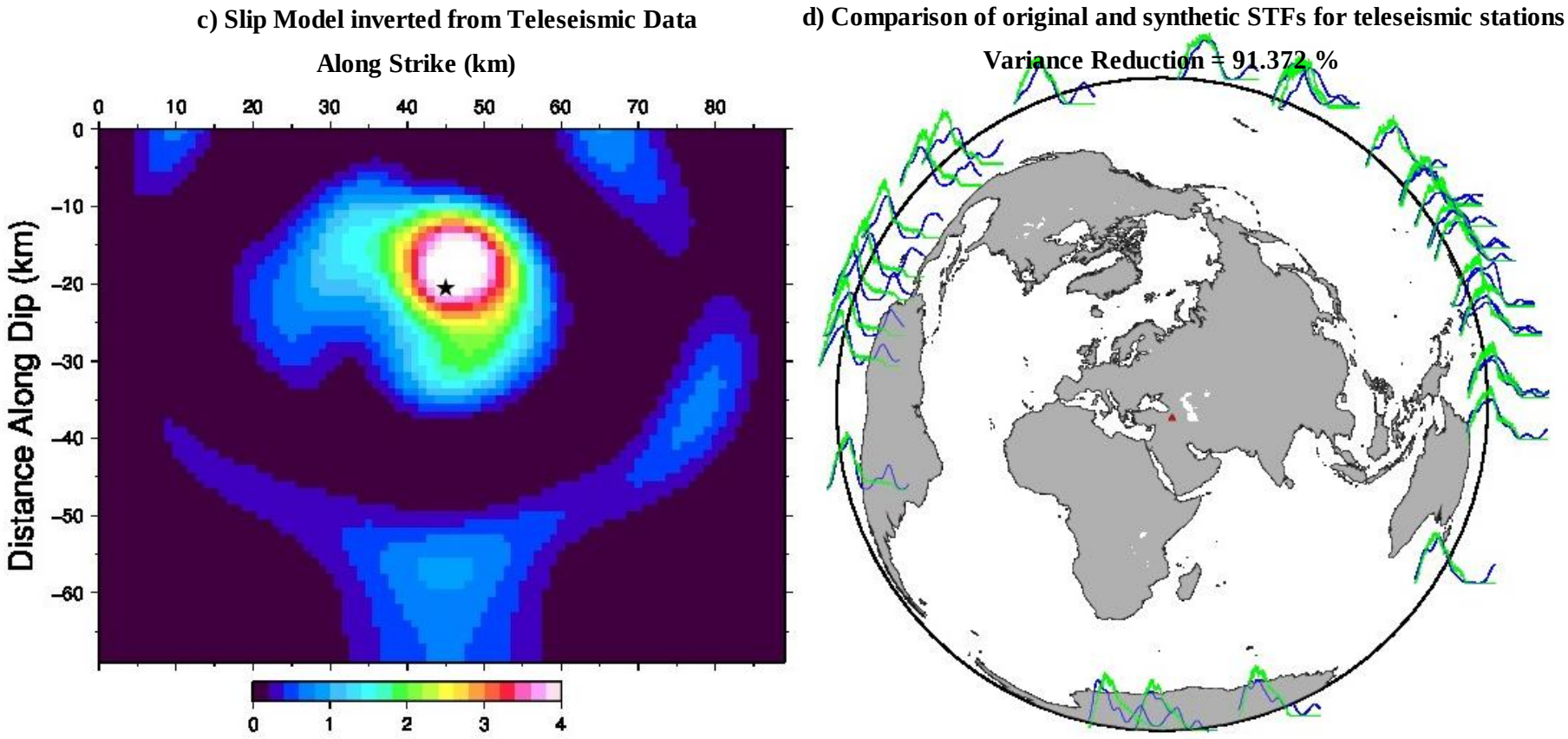

Figure 4.5. (c) Comparison of original and synthetic STFs and (d) the slip model inverted from teleseismic data Rupture Velocity $V_R = 1.5\ km/s$; rise time $T_D = 1.0\ s$.

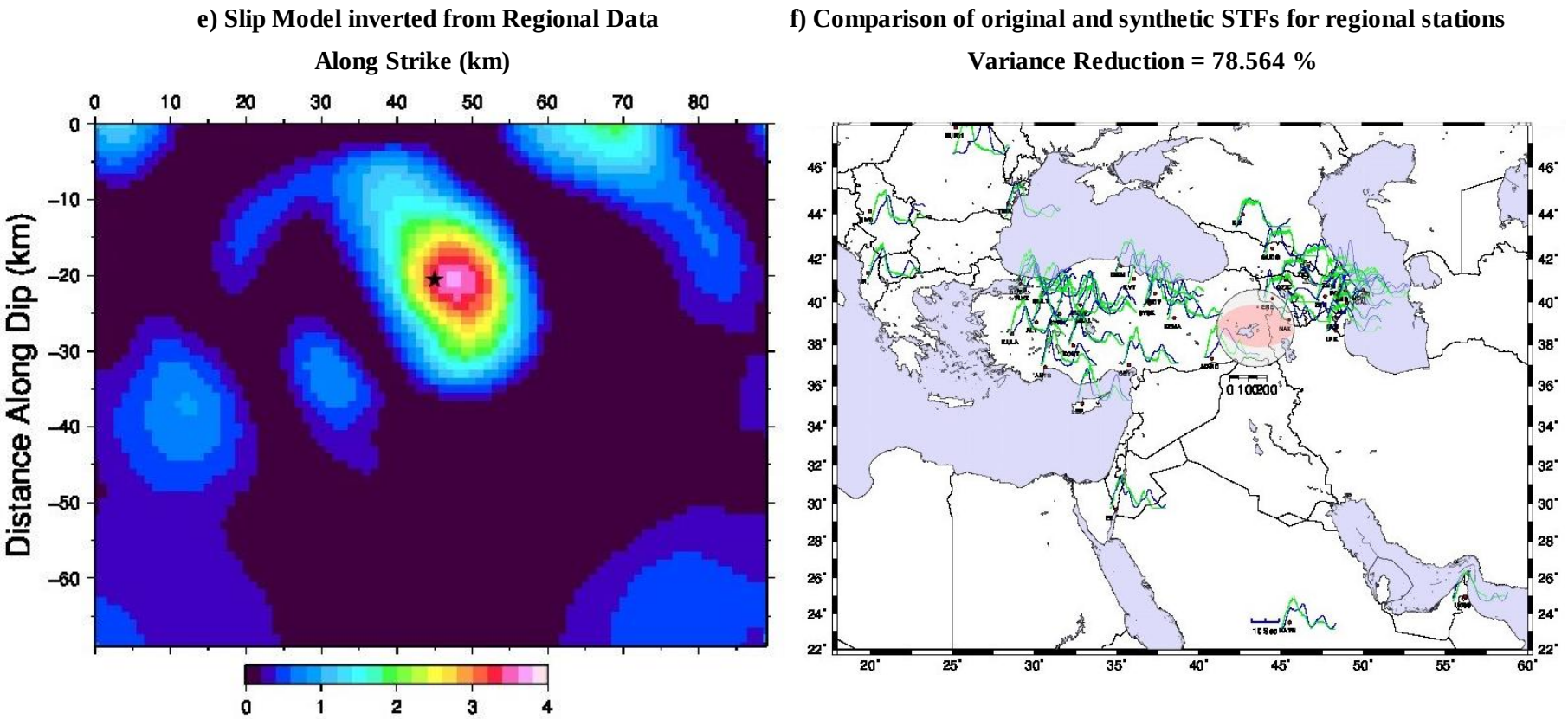

Figure 4.5. (e) Comparison of original and synthetic STFs and (f) the slip model inverted from regional data Rupture Velocity $V_R = 1.5\ km/s$; rise time $T_D = 1.0\ s$.

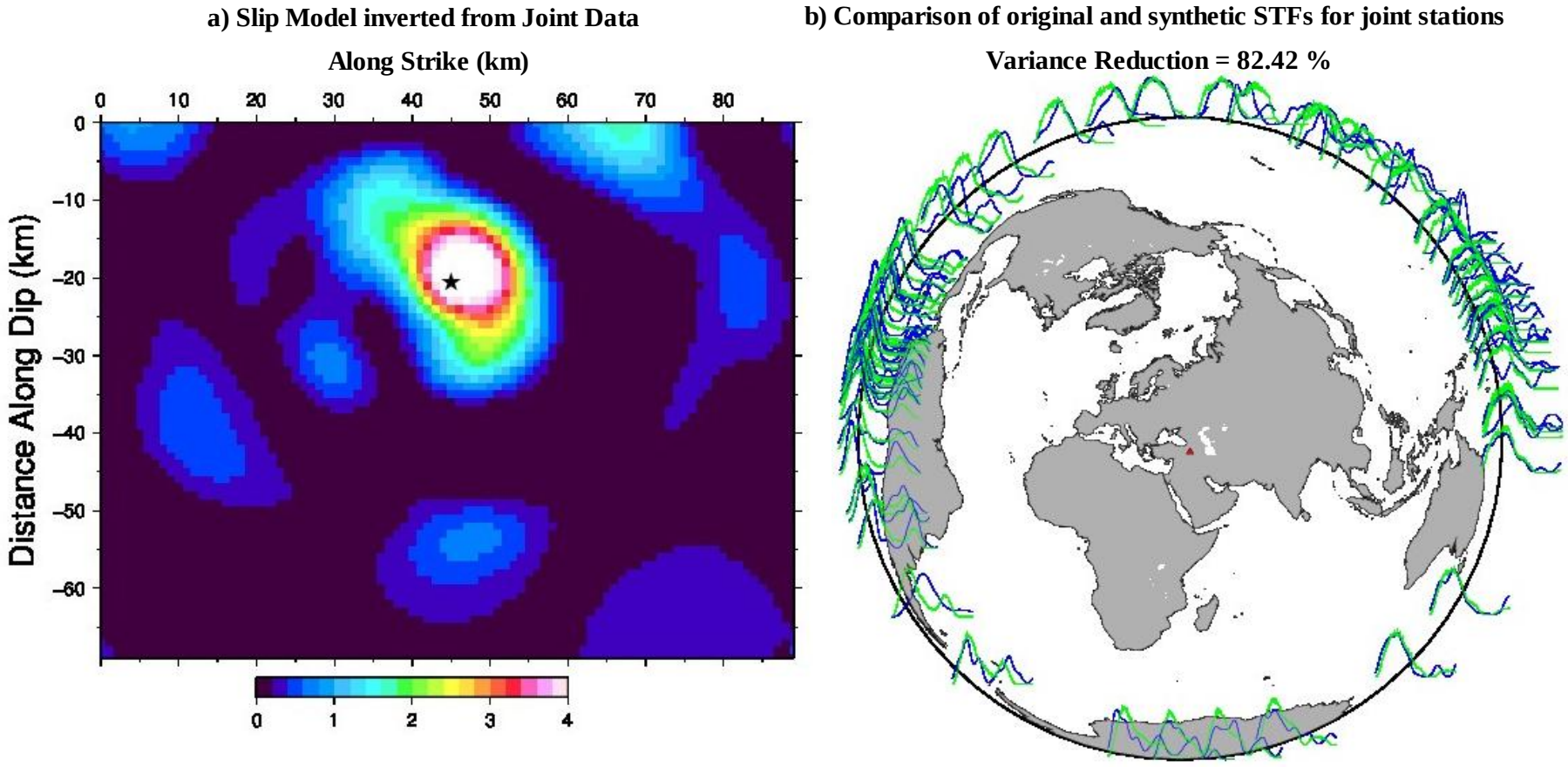

Figure 4.6. (a) Comparison of original and synthetic STFs and (b) the slip model inverted from joint data Rupture Velocity $V_R = 1.5\ km/s$; rise time $T_D = 1.5\ s$.

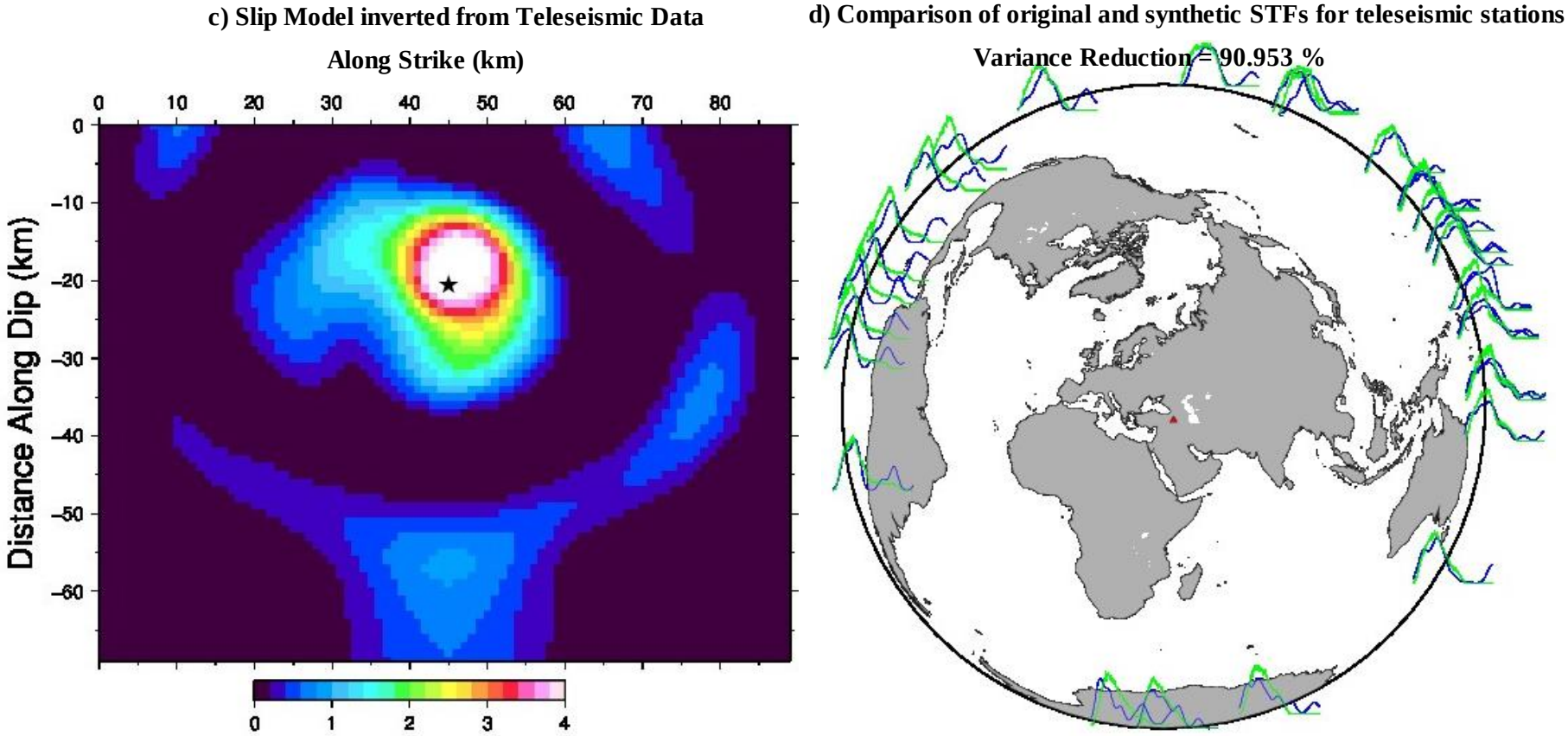

Figure 4.6. (c) Comparison of original and synthetic STFs and (d) the slip model inverted from teleseismic data Rupture Velocity $V_R = 1.5\ km/s$; rise time $T_D = 1.5\ s$.

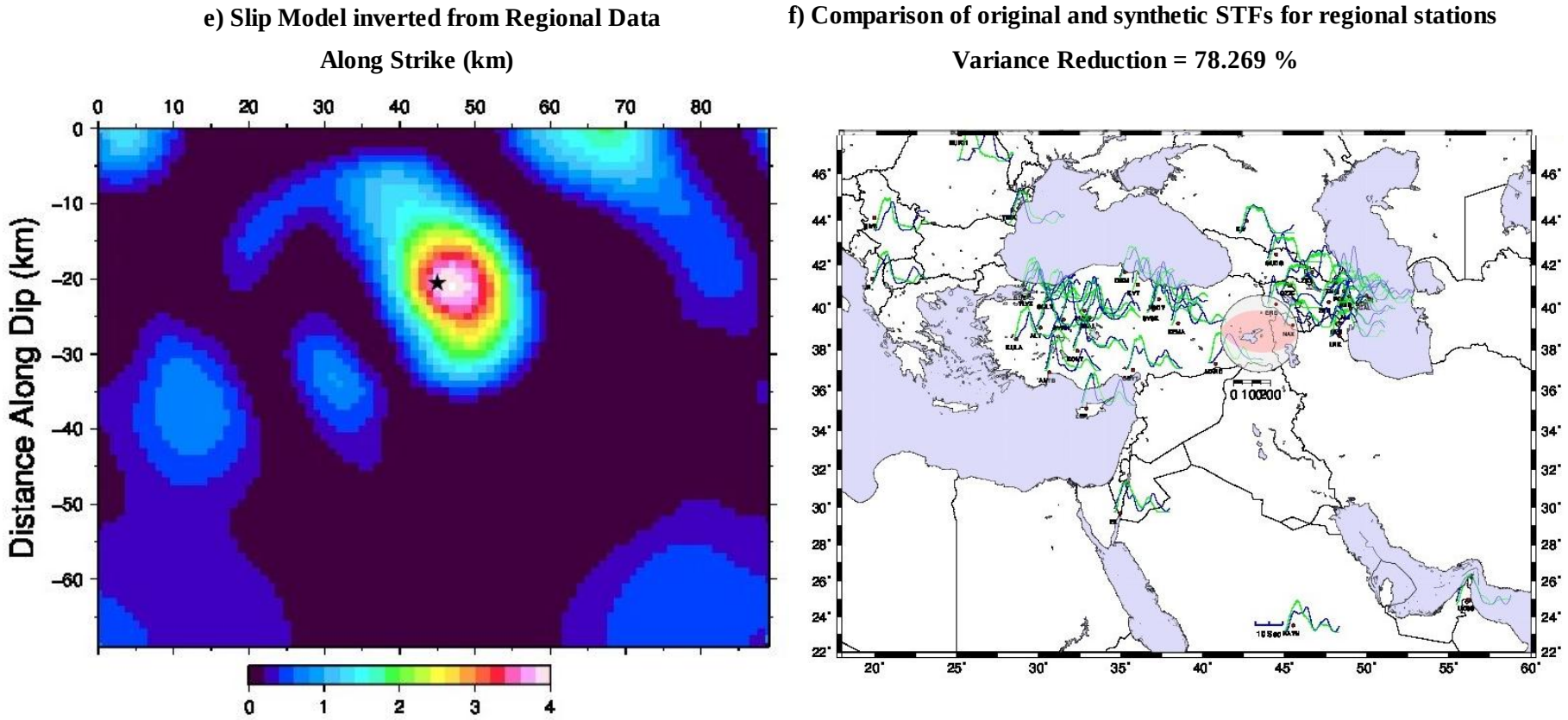

Figure 4.6. (e) Comparison of original and synthetic STFs and (f) the slip model inverted from regional data Rupture Velocity $V_R = 1.5\ km/s$; rise time $T_D = 1.5\ s$.

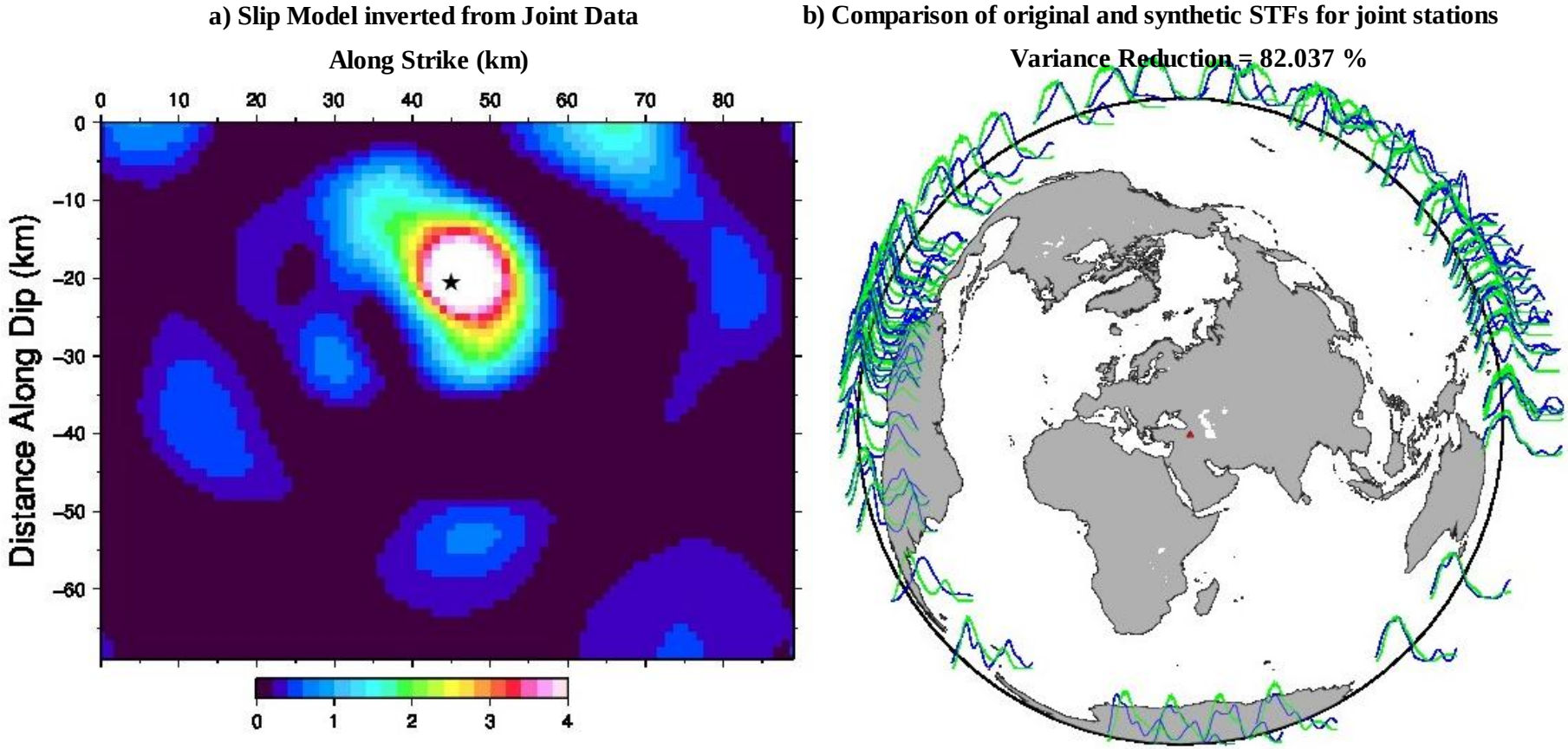

Figure 4.7. (a) Comparison of original and synthetic STFs and (b) the slip model inverted from joint data Rupture Velocity $V_R = 1.5\ km/s$; rise time $T_D = 2.0\ s$.

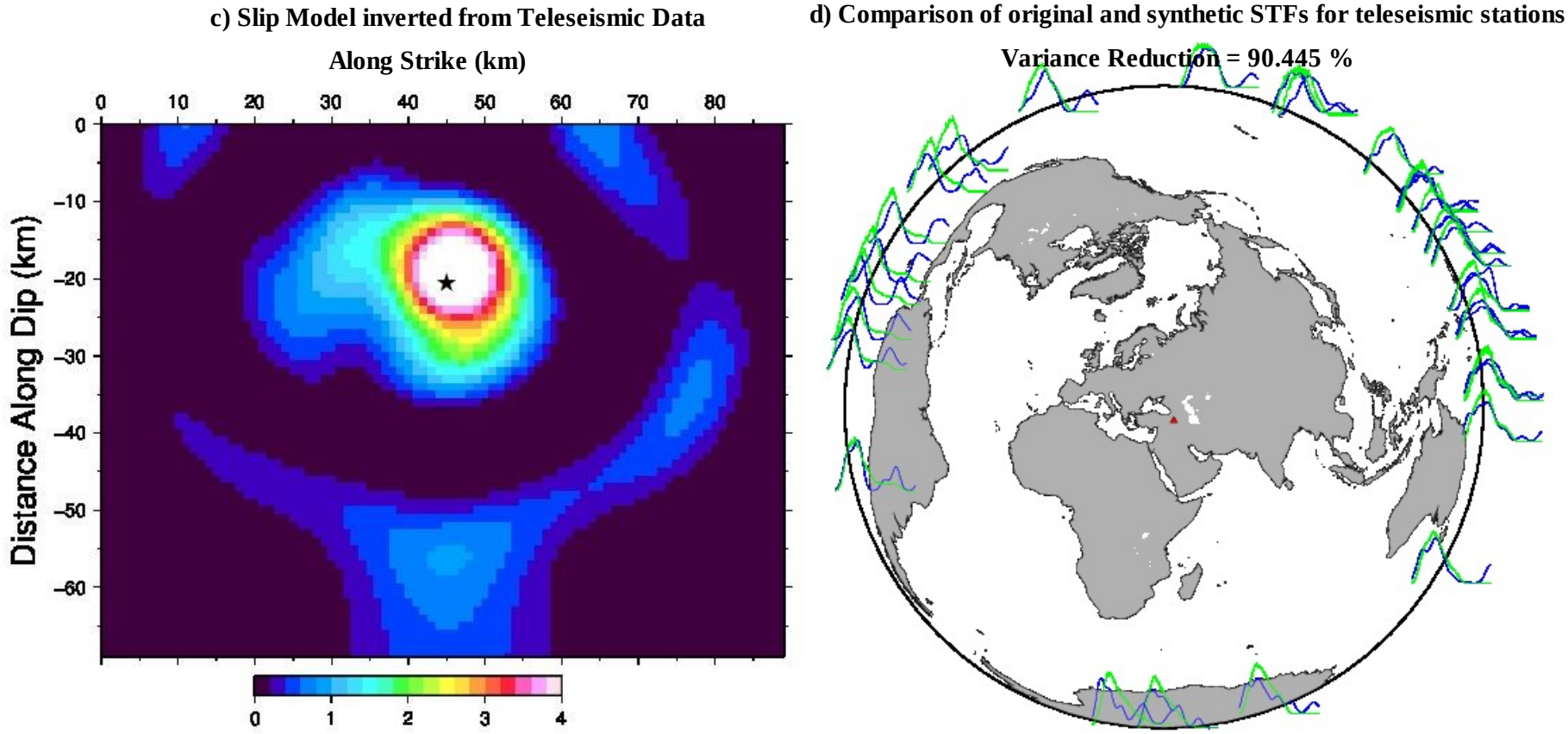

Figure 4.7. (c) Comparison of original and synthetic STFs and (d) the slip model inverted from teleseismic data Rupture Velocity $V_R = 1.5\ km/s$; rise time $T_D = 2.0\ s$.

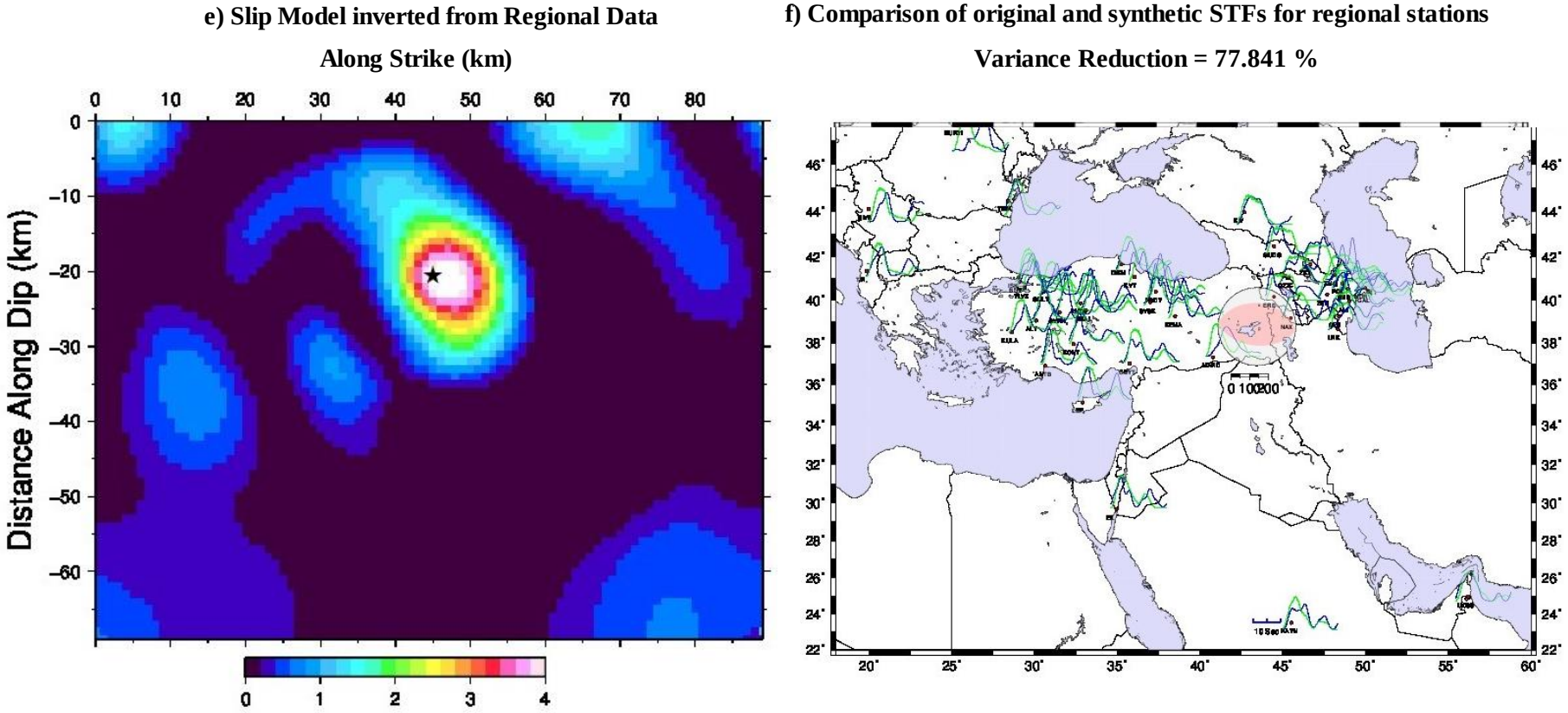

Figure 4.7. (e) Comparison of original and synthetic STFs and (f) the slip model inverted from regional data Rupture Velocity $V_R = 1.5\ km/s$; rise time $T_D = 2.0\ s$.

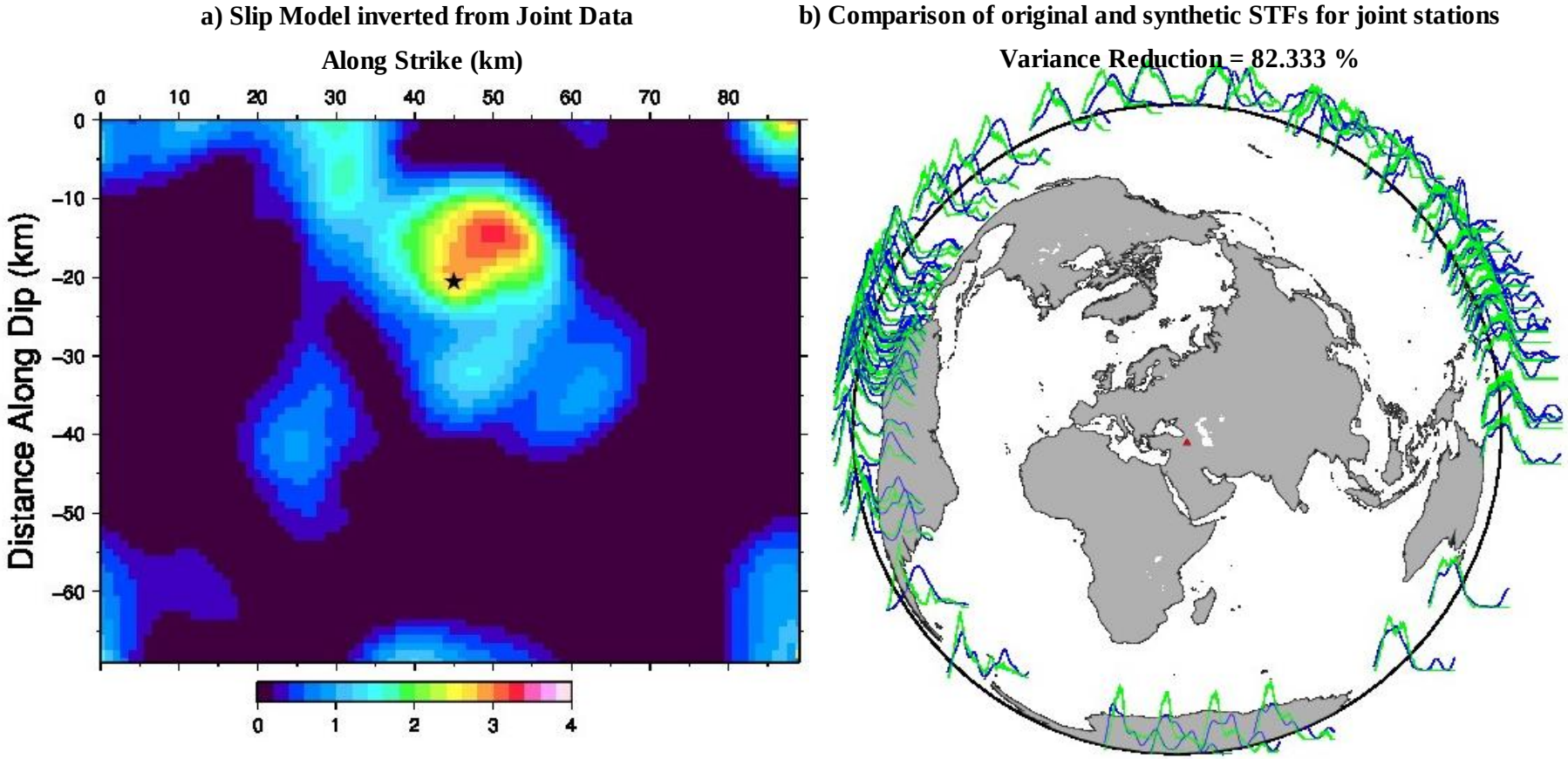

Figure 4.8. (a) Comparison of original and synthetic STFs and (b) the slip model inverted from joint data Rupture Velocity $V_R = 2.0\ km/s$; rise time $T_D = 1.0\ s$.

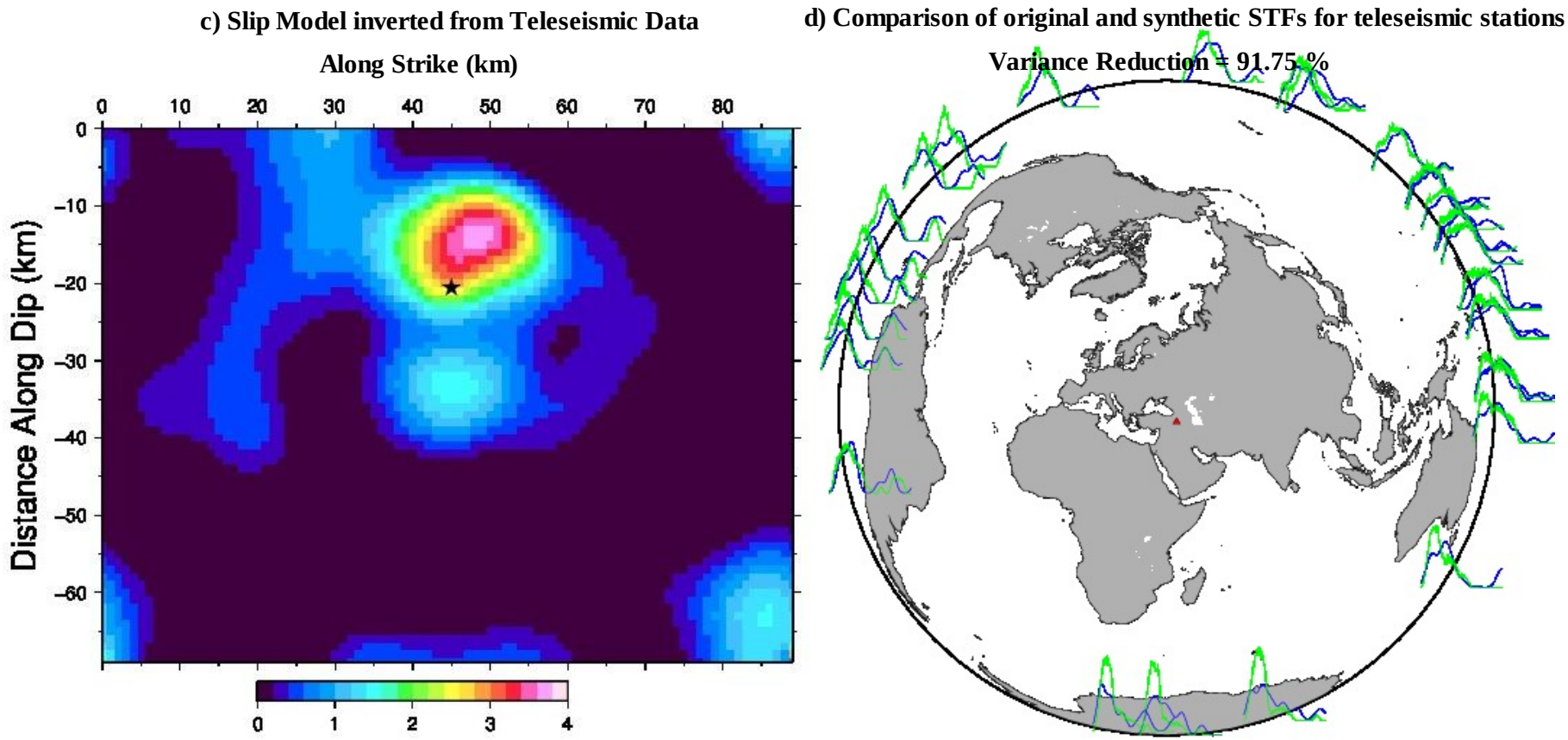

Figure 4.8. (c) Comparison of original and synthetic STFs and (d) the slip model inverted from teleseismic data Rupture Velocity $V_R = 2.0\ km/s$; rise time $T_D = 1.0\ s$.

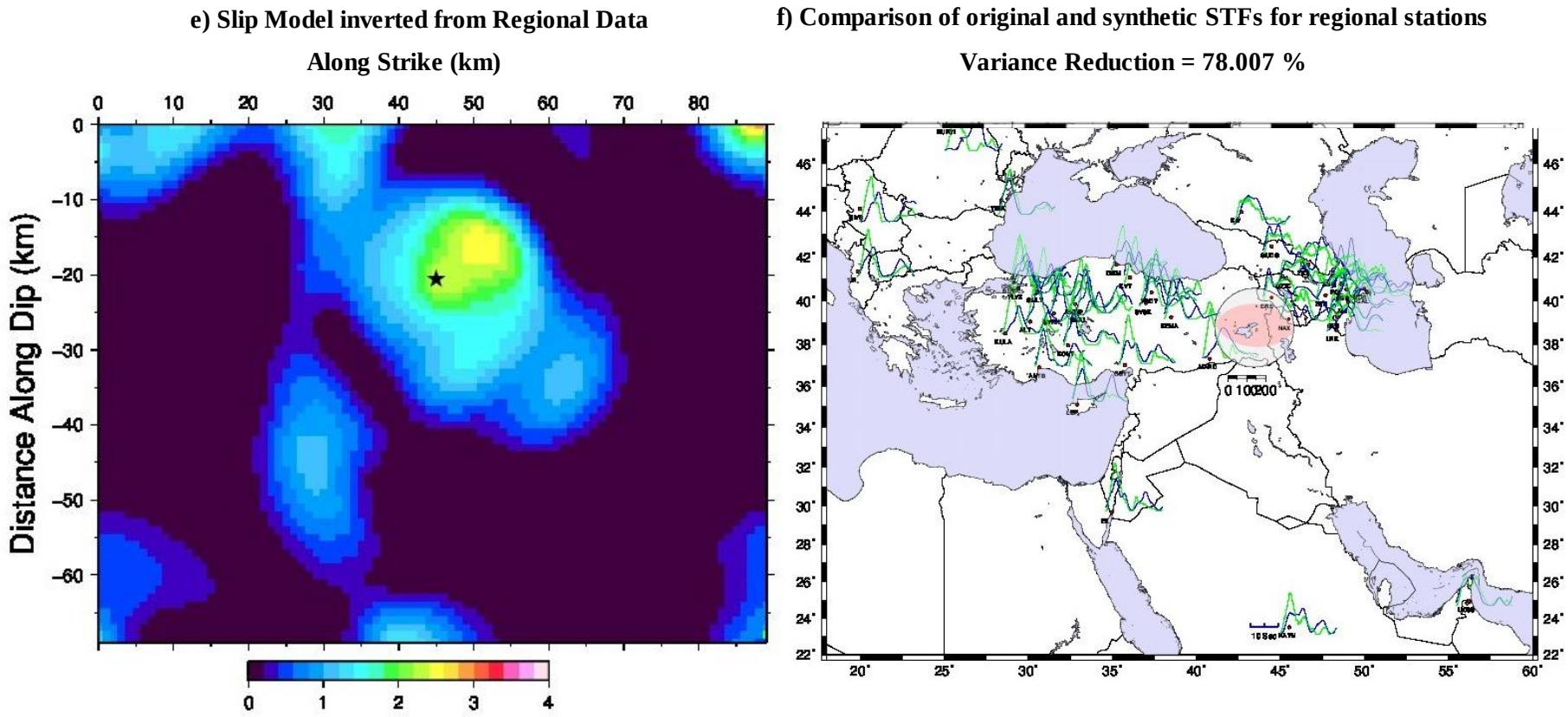

Figure 4.8. (e) Comparison of original and synthetic STFs and (f) the slip model inverted from regional data Rupture Velocity $V_R = 2.0\ km/s$; rise time $T_D = 1.0\ s$.

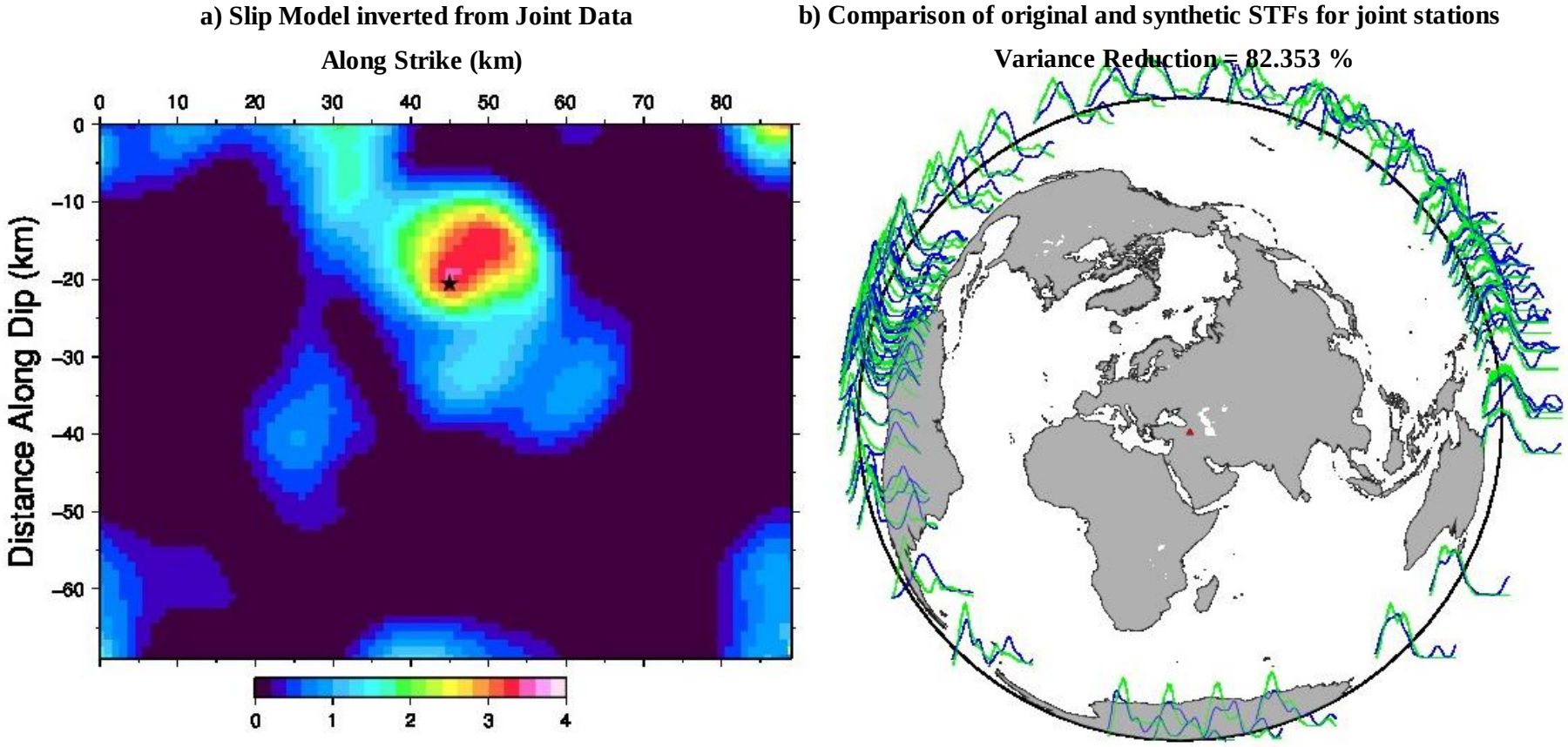

Figure 4.9. (a) Comparison of original and synthetic STFs and (b) the slip model inverted from joint data Rupture Velocity $V_R = 2.0\ km/s$; rise time $T_D = 1.5\ s$.

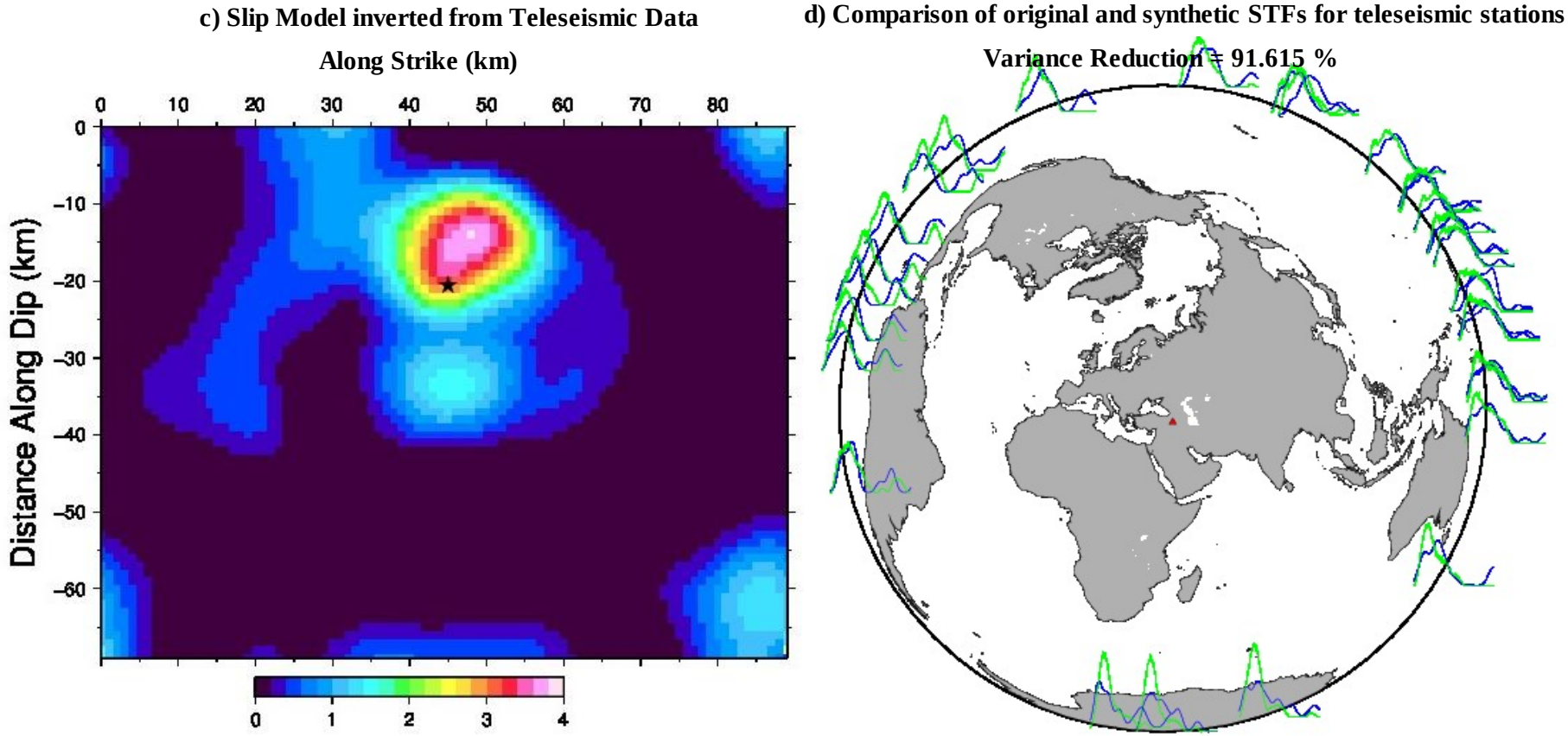

Figure 4.9. (c) Comparison of original and synthetic STFs and (d) the slip model inverted from teleseismic data Rupture Velocity $V_R = 2.0\ km/s$; rise time $T_D = 1.5\ s$.

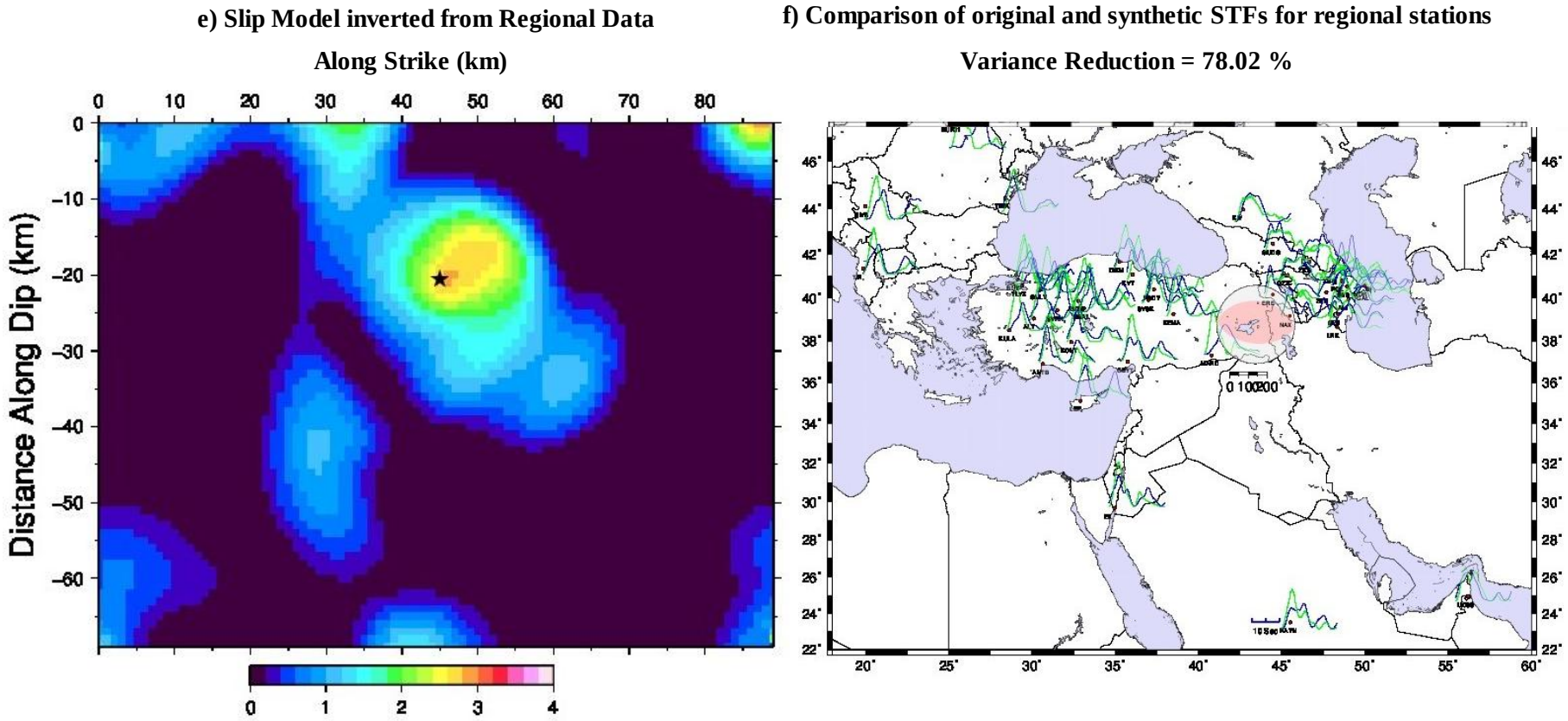

Figure 4.9. (e) Comparison of original and synthetic STFs and (f) the slip model inverted from regional data Rupture Velocity $V_R = 2.0\ km/s$; rise time $T_D = 1.5\ s$.

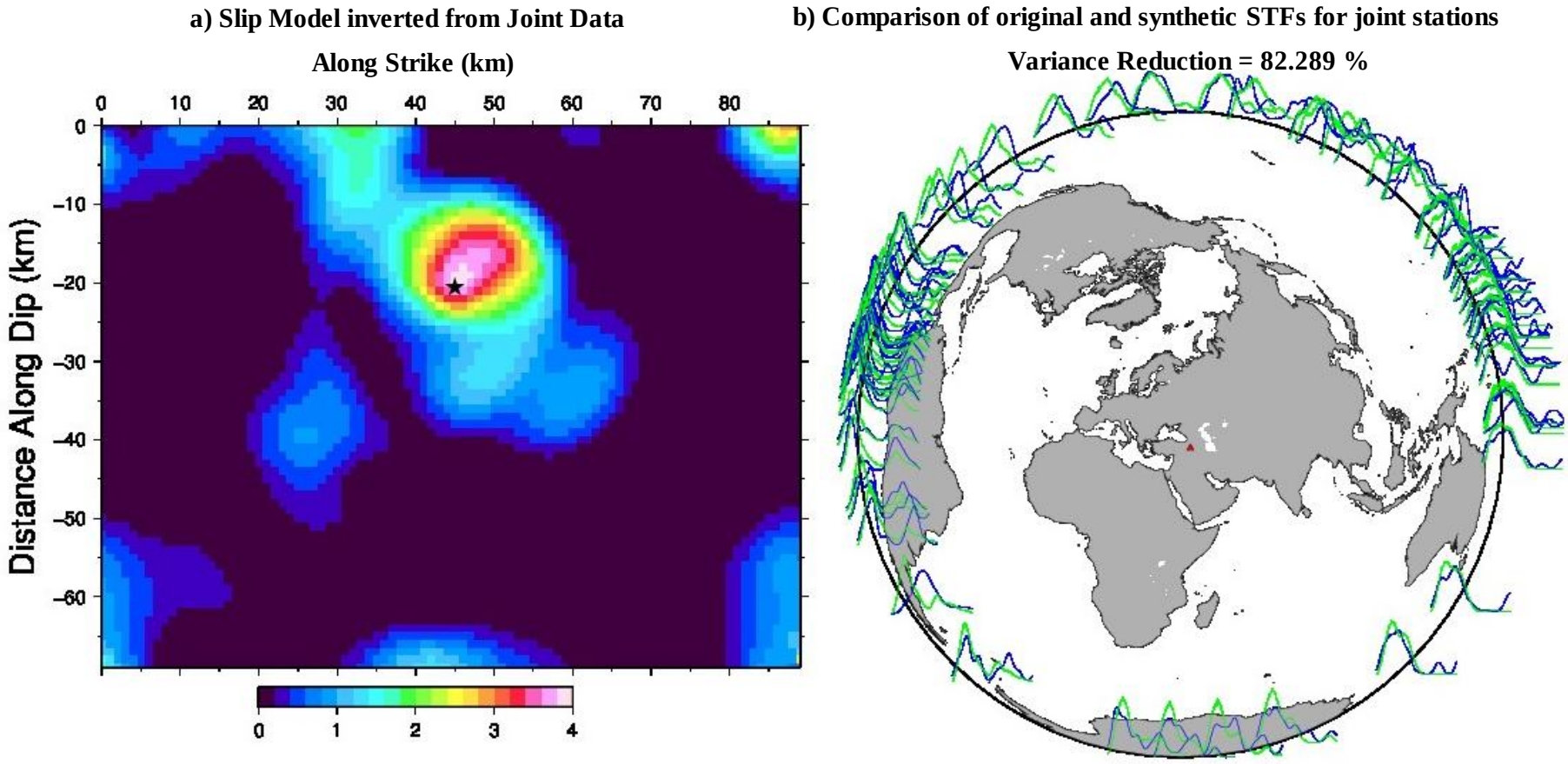

Figure 4.10. (a) Comparison of original and synthetic STFs and (b) the slip models inverted from joint data Rupture Velocity $V_R = 2.0\ km/s$; rise time $T_D = 2.0$ s.

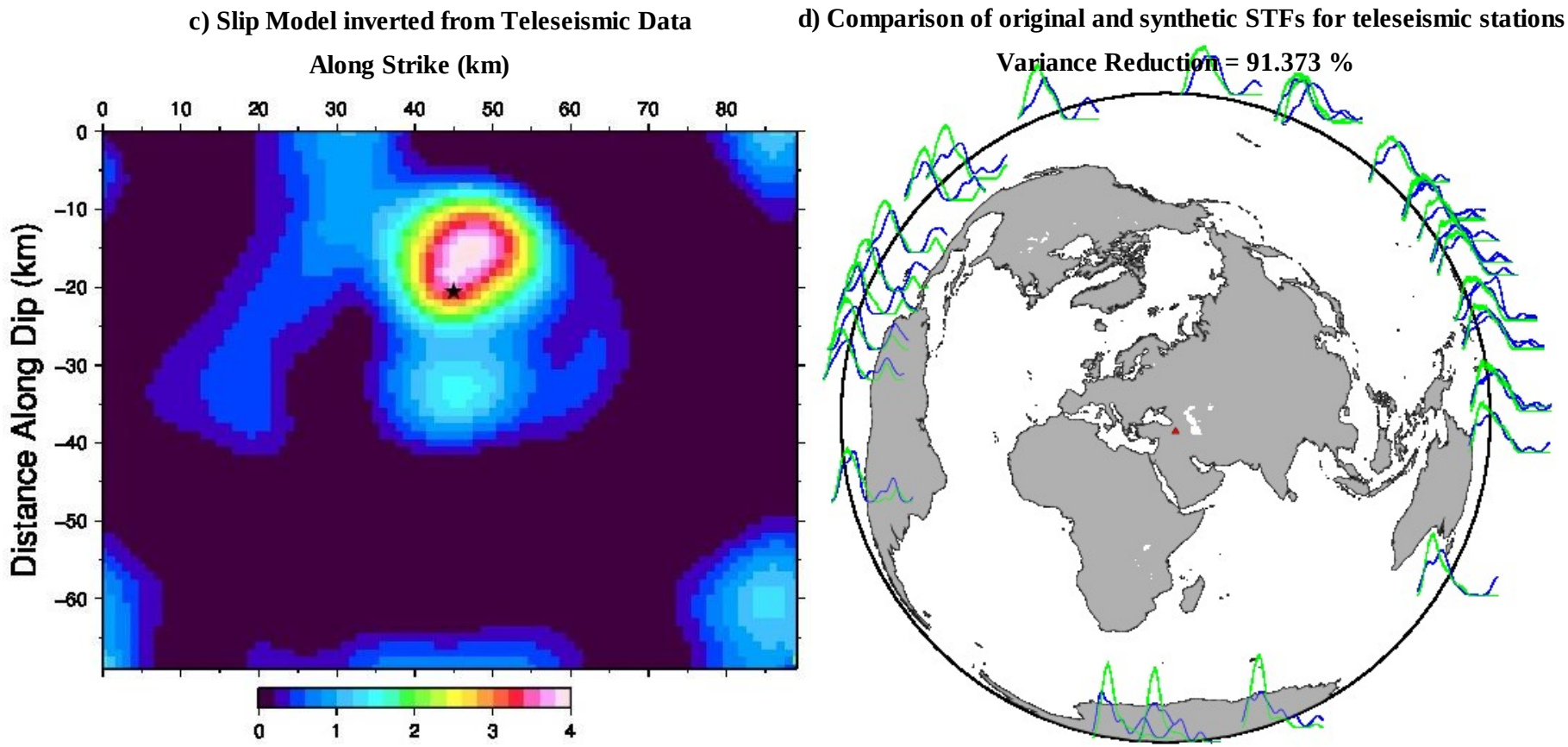

Figure 4.10. (c) Comparison of original and synthetic STFs and (d) the slip model inverted from teleseismic data Rupture Velocity $V_R = 2.0\ km/s$; rise time $T_D = 2.0\ s$.

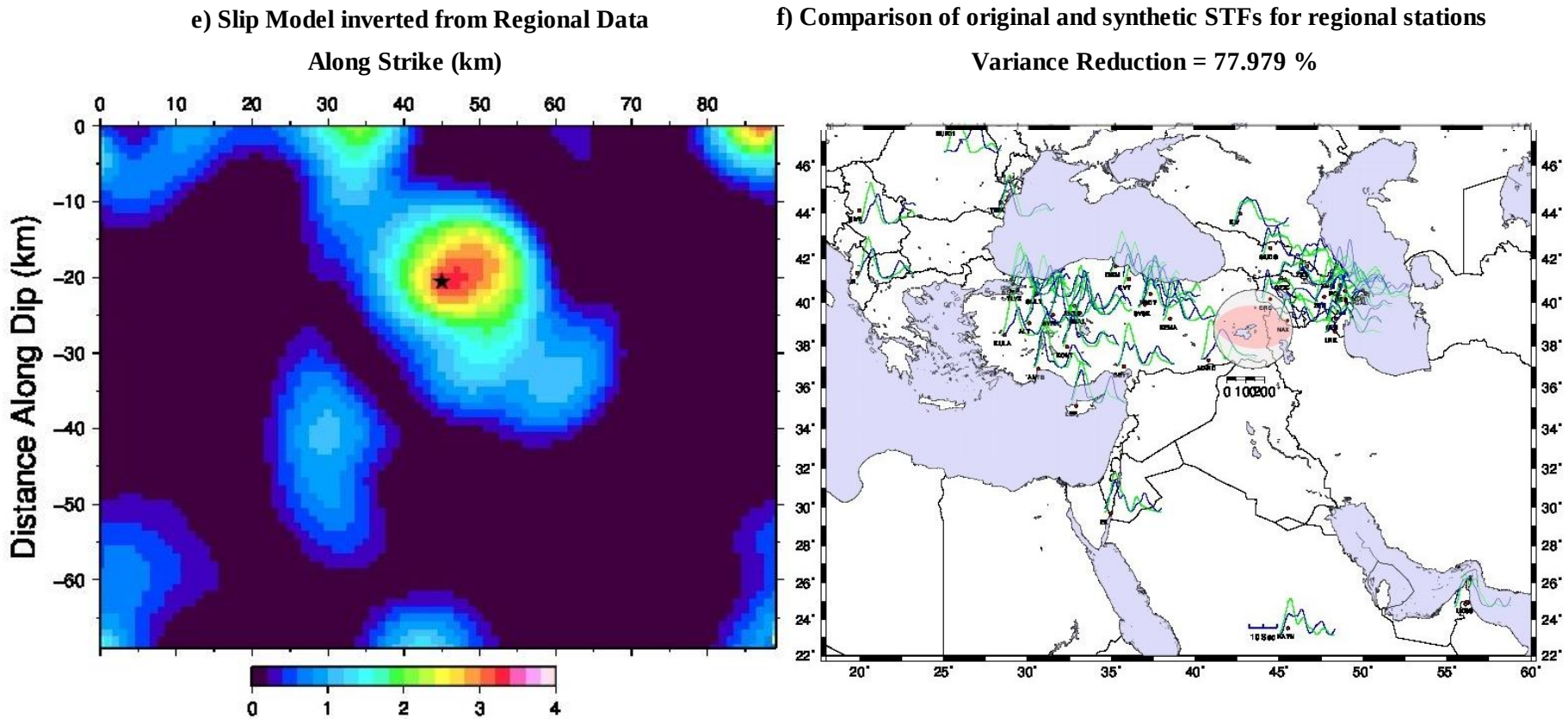

Figure 4.10. (e) Comparison of original and synthetic STFs and (f) the slip model inverted from regional data Rupture Velocity $V_R = 2.0\ km/s$; rise time $T_D = 2.0$ s.

5. DISCUSSION

5.1. Comparison with Currently Available Slip Models

So far, the only available finite-fault solutions for the 2011 Van Earthquake are those published online right after the earthquake *e.g.*, Gaven Hayes's solution on the USGS website, Chen Ji's solution published on the UCSB Large Earthquake Database, teleseismic model of Utkucu 2013 and Yagi (2011) as shown in Figure 5.1.a, 5.1.b, 5.2 and 5.3, respectively. All of these solutions are obtained from teleseismic waves using 1D Green's functions (Ji *et al*., 2002). Figure 5.1 compares these two solutions with our best-fit solution. The teleseismic solution of Ji 2011, Hayes 2011 and also Utkucu (2013) show that maximum slip is to the west of the hypocentre which is consistent with the solution obtained in this study from regional-teleseismic EGF's. Rupture velocity obtained by Ji *et al*. 2011, is about 1 km/s, while Hayes 2011 has obtained 1.5 km/s. Here we obtain the viable range of rupture velocities as 1.5-2 km/s. This value is roughly 50% of the shear wave used (3.4 km/s) in this study. Maximum slip obtained by Hayes is about 4 m and the one obtained by Ji is about 3.5 m and rupture direction is unilateral to SW. In this study we obtain the maximum slip as 3.5 m. The rise time is not available to the reader from these models. According to Yagi (2011) the rupture direction is bilateral up-dip and the maximum slip 4.5 m.

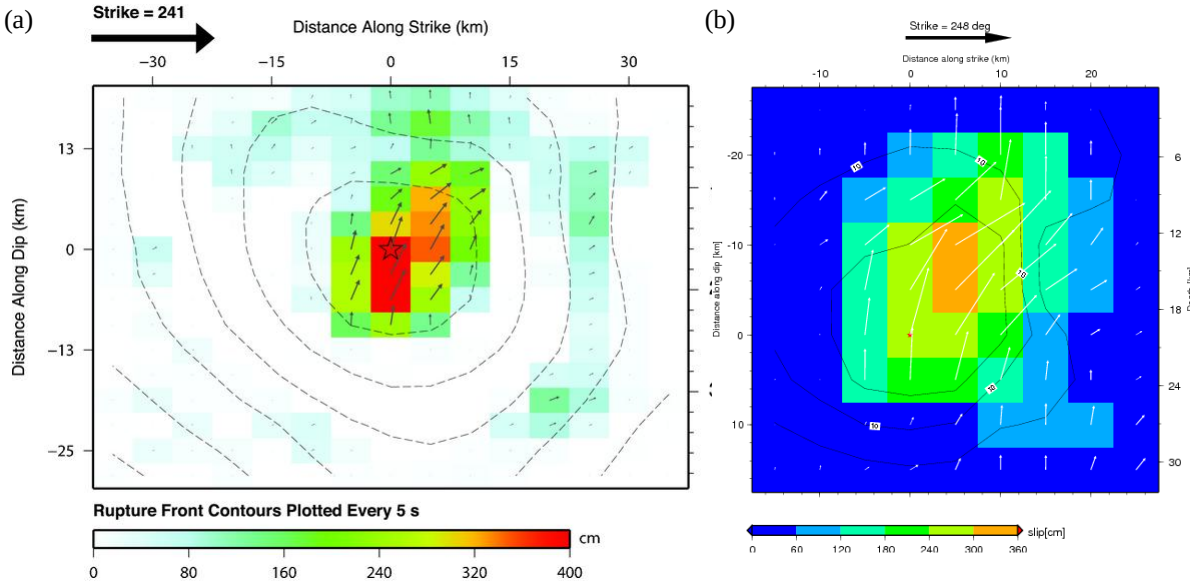

Figure 5.1. Various slip models for the 2011 Van M_w 7.1 Earthquake from (a) Hayes (2011) (b) Ji (2011).
(http://www.geol.ucsb.edu/faculty/ji/big_earthquakes/2011/10/23/turkey.html)

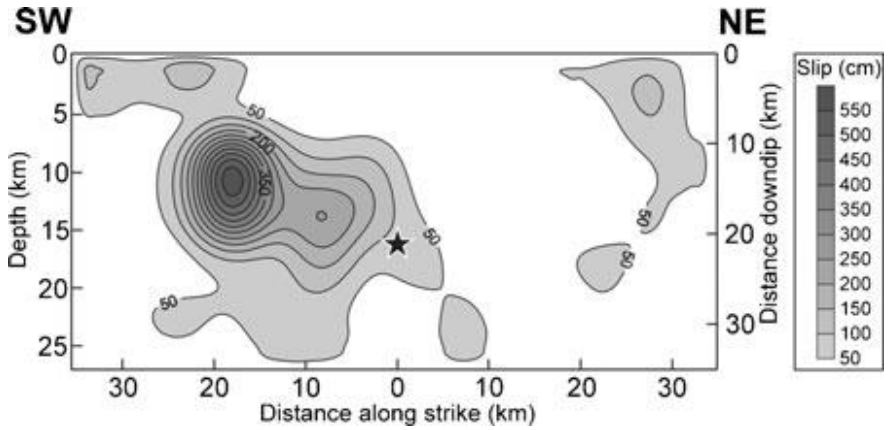

Figure 5.2. Slip model for the 2011 Van Mw 7.1 Earthquake from Utkucu (2013).

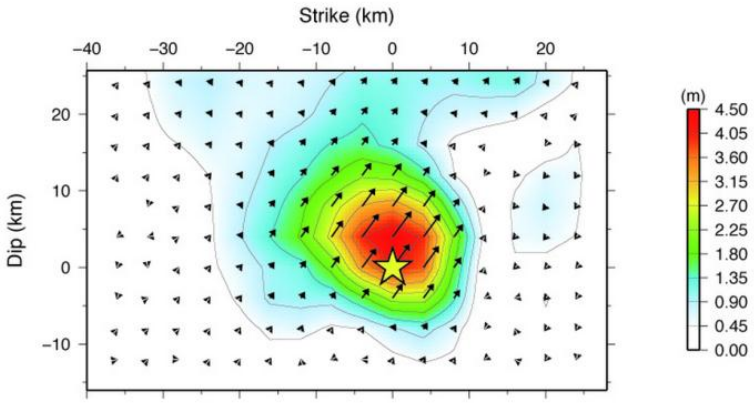

Figure 5.3. Slip model for the 2013 Van M_w 7.1 Earthquake from Yagi (2011).

5.2. Comparison with Other Reverse Mechanism Earthquakes and Comments on the Rupture Parameters

Here, we aim to characterize the rupture parameters of Van Earthquake by comparing it to other thrust mechanism earthquakes. We choose the M_w 7.5 1999 Chi-Chi, Taiwan Earthquake for comparison. Chi-Chi Earthquake was one of the best recorded and slip modeled earthquakes due to its dense station coverage (Schubert, 2007). It was a thrust mechanism interplate earthquake with a 5° of strike angle to NE and a 30° of dip angle in the direction of SW (Yagi and Kikuchi, 2001) (Figure 5.4). Since this earthquake was well studied with great detail, it can be used as a reference for comparison for the 2011 Van Earthquake.

Ji *et al*. (2003) has modelled the Chi-Chi Earthquake using the available strong-motion and GPS network. He has obtained a rupture velocity of 2 km/s, similar to the 2011 Van Earthquake. The average rise time obtained for Chi-Chi is about 7 seconds. Here we obtain rise time of 1-2 seconds with average slip of 2.5 m inside the asperity. This corresponds to a slip rate of ~1.5 m/s. Therefore, although Chi-Chi and Van Earthquake are of different magnitude, they are similar in terms of rupture parameters.

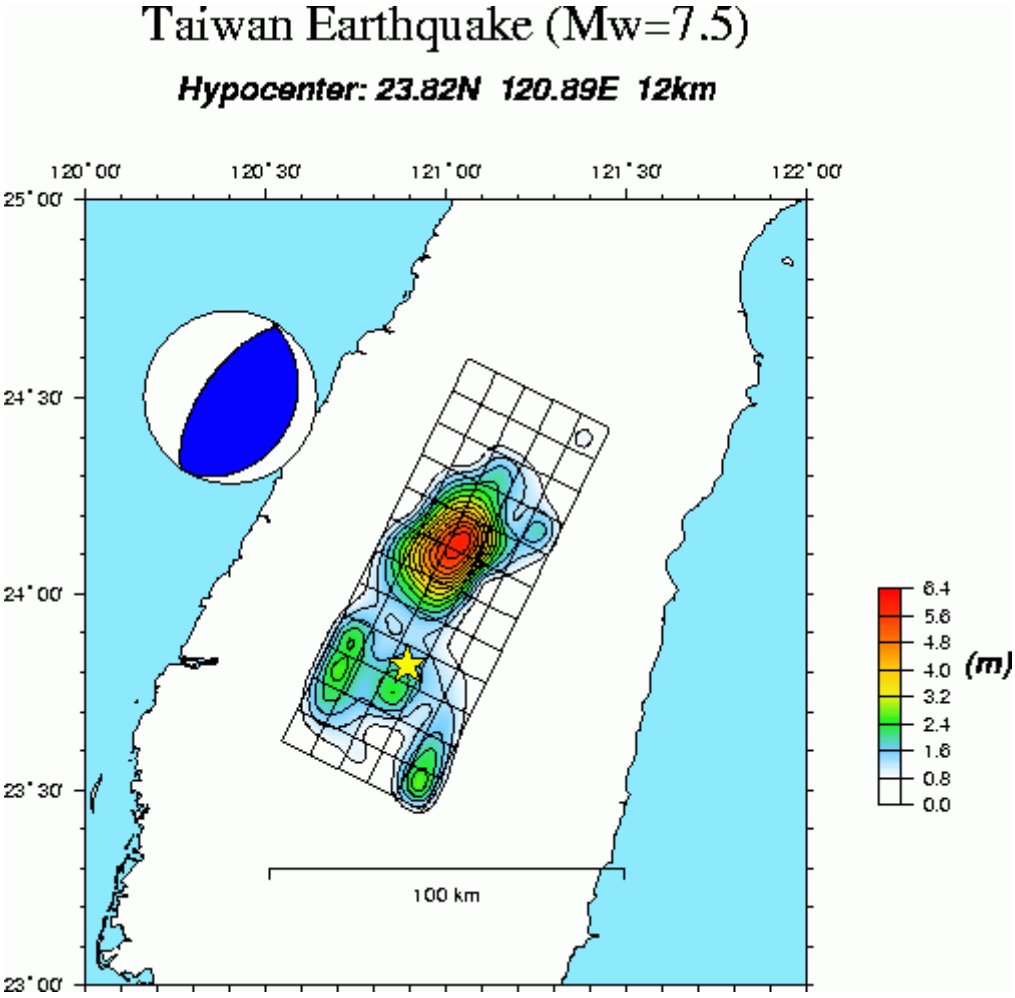

Figure 5.4. Map of slip distribution and focal mechanism for the 1999 Chi-Chi, Taiwan Earthquake (Yagi and Kikuchi, 2001).

The rupture velocity obtained here is about 45-60% of the shear wave speed. This slower rupture velocity is common for thrust earthquakes, where the behaviour is more Mode 3 crack. Usually rupture velocities are lower for reverse mechanism earthquakes in comparison to strike-slip earthquakes. For example, the rupture velocity of M_w8.5 2005 Nias Earthquake is about 2-2.5 km/s (Konca *et al*., 2007) and in 2011 M_w9 Tohoku Earthquake, rupture velocity is found to be around 1.2 km/s (Simons *et al*., 2011).

Therefore, Van Earthquake can be thought as a characteristic reverse mechanism earthquake in terms of its rupture velocity and slip rate on the fault.

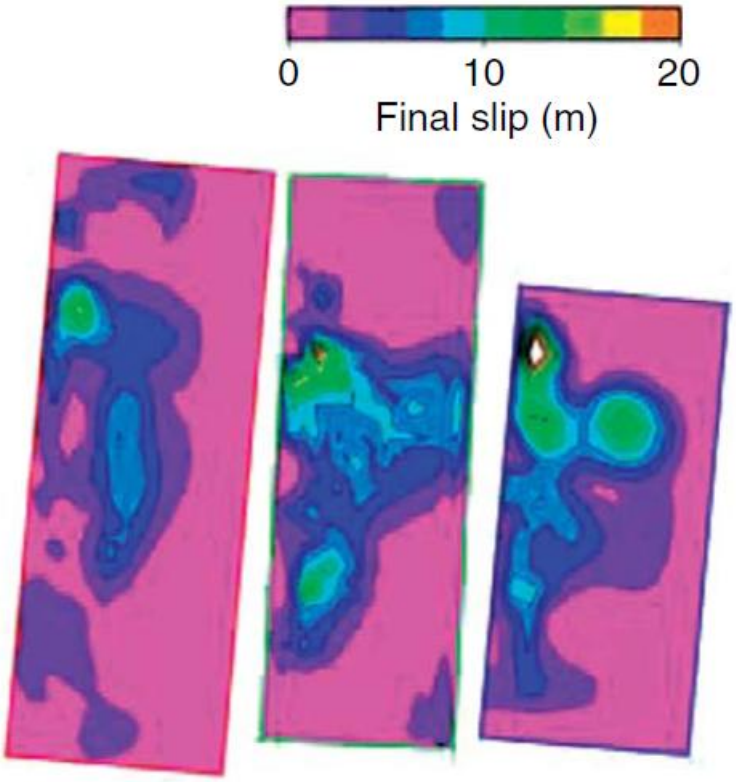

Figure 5.5. Various slip models for the 1999 Chi-Chi, Taiwan Earthquake from Chi *et al*. (2001), Ma *et al*. (2001) and Wu *et al*. (2001), respectively, modified by (Schubert, 2007).

5.3. Robustness of the Solution

Considering that we obtain similar results from both teleseismic and regional Green's functions implies that the average rupture velocity and the rise time we obtain are reliable. This allows us to join the regional and teleseismic distances and model the STF's from 2° all the way to 90° distances. However, further resolution tests with the given station configuration are necessary in order to understand the resolution of the slip distribution. This will be future work of this study.

6. CONCLUSIONS

We obtain a kinematic source model for the 23 October 2011 Van Earthquake using the Empirical Green's Function Method for both regional and teleseismic distances. The slip models are in good agreement with each other and also with previous studies for Van M_w 7.1 Earthquake. We determine the source characteristics such as rupture velocity, rise time where the models have high variance reductions. We find the range of rupture velocities between 1.5 and 2 km/s and the rise time between 1 s and 2 s. The rupture velocity is roughly 50% of the shear wave used (3.4 km/s) in this study. The maximum slip is about 3-3.5 meters and concentrated nearly at the hypocenter with a westward propagation along strike. The rupture progpagation is unidirectional which is consistent with the claim of large earthquakes are unidirectional (McGuire *et al.*, 2001). Van Earthquake has a reverse mechanism with small sinistral component in terms of its rupture velocity and slip rate on the fault as shown in Figure 6.1.

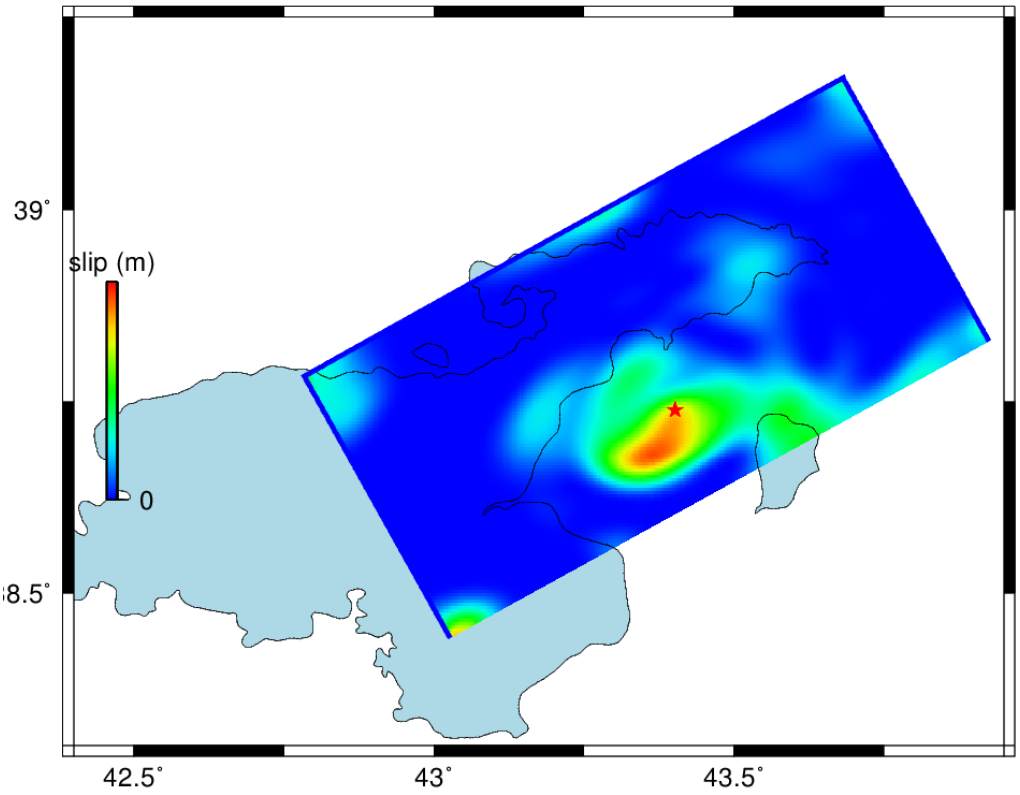

Figure 6.1. Map of the slip model for the October 23, 2011 Van M_w 7.1 Earthquake, inverted from joint data where rupture velocity is $V_R = 2.0\ km/s$; rise time $T_D = 1.0\ s$.

REFERENCES

Aki, K., 1968, "Seismic Displacements Near a Fault", *Journal of Geophysical Research*, 73, 5359-5376.

Aki, K. and P.G. Richards, 2002, *Quantitative Seismology: Theory and Methods*, University Science Books.

Archuleta, R.J., 1984, "A Faulting Model for the 1979 Imperial Valley Earthquake", *Journal of Geophysical Research: Solid Earth*, 89, 4559-4585.

Barazangi, M., E. Sandvol and D. Seber, 2006, "Structure and Tectonic Evolution of the Anatolian Plateau in Eastern Turkey", in Y. Dilek, S. Pavlides, (eds.), *Postcollisional Tectonics and Magmatism in the Mediterranean Region and Asia, Geological Society of America Inc, Boulder*, pp. 463-473.

Benioff, H., F. Press and S. Smith, 1961, "Excitation of the Free Oscillations of the Earth by Earthquakes", *Journal of Geophysical Research*, 66, 605-619.

Beroza, G.C., 1991, "Near-Source Modeling of the Loma-Prieta Earthquake - Evidence for Heterogeneous Slip and Implications for Earthquake Hazard", *Bulletin of the Seismological Society of America*, 81, 1603-1621.

Bozkurt, E., 2001, "Neotectonics of Turkey - A Synthesis", *Geodinamica Acta*, 14, 3-30.

Bracewell, R.N., 2000, *The Fourier Transform and Its Applications*, McGraw-Hill Higher Education.

Chi, W.C., D. Dreger, A. Kaverina, 2001, "Finite-Source Modeling of the 1999 Taiwan (Chi-Chi) Earthquake Derived from a Dense Strong-Motion Network", *Bulletin of the Seismological Society of America*, 91, 1144-1157.

Dewey, J.F. and K.C.A.Burke, 1973, "Tibetan, Variscan, and Precambrian Basement Reactivation: Products of Continental Collision", *The Journal of Geology*, 81, 683-692.

Dewey, J.F., M.R. Hempton, W.S.F. Kidd, F. Şaroğlu and A.M.C. Şengör, 1986, "Shortening of Continental Lithosphere: The Neotectonics of Eastern Anatolia — a Young Collision Zone", *Geological Society*, London, Special Publications 19, 1-36.

Dewey, J.F. and A.M.C. Şengör, 1979, "Aegean and Surrounding Regions: Complex Multiplate and Continuum Tectonics in a Convergent Zone", *Geological Society of America Bulletin*, 90, 84-92.

Dreger, D.S., 1994, "Empirical Greens-Function Study of the January 17, 1994 Northridge, California Earthquake", *Geophysical Research Letters*, 21, 2633-2636.

Faccenna, C., O. Bellier, J. Martinod, C. Piromallo and V. Regard, 2006, "Slab Detachment Beneath Eastern Anatolia: A Possible Cause for the Formation of the North Anatolian fault", *Earth and Planetary Science Letters*, 242, 85-97.

Fukao, Y. and M. Kikuchi, 1987, "Source Retrieval for Mantle Earthquakes by Iterative Deconvolution of Long-Period P-Waves", *Tectonophysics*, 144, 249-269.

Hartzell, S., P.C. Liu and C. Mendoza, 1996, "The 1994 Northridge, California, Earthquake: Investigation of Rupture Velocity, Risetime, and High-Frequency Radiation", *Journal of Geophysical Research-Solid Earth*, 101, 20091-20108.

Hartzell, S.H., 1978, "Earthquake Aftershocks as Greens Functions", *Geophysical Research Letters*, 5, 1-4.

Hartzell, S.H. and T.H. Heaton, 1983, "Inversion of Strong Ground Motion and Teleseismic Waveform Data for the Fault Rupture History of the 1979 Imperial Valley, California, Earthquake", *Bulletin of the Seismological Society of America*, 73, 1553-1583.

Haskell, N.A., 1964, "Total Energy and Energy Spectral Density of Elastic Wave Radiation from Propagating Faults", *Bulletin of the Seismological Society of America,* 54, 1811-1841.

Haskell, N.A., 1969, "Elastic Displacements in the Near-Field of a Propagating Fault", *Bulletin of the Seismological Society of America,* 59, 865-908.

Jackson, J. and D. McKenzie, 1988, "The Relationship Between Plate Motions and Seismic Moment Tensors, and the Rates of Active Deformation in the Mediterranean and Middle East", *Geophysical Journal,* 93, 45-73.

Ji, C., D. Helmberger, D. Wald and K. Ma, 2003, "Slip History and Dynamic Implications of the 1999 Chi-Chi, Taiwan, Earthquake", *Journal of Geophysical Research-Solid Earth,* 108, Art. No. 2412.

Ji, C., D. Wald and D.V. Helmberger, 2002, "Source Description of the 1999 Hector Mine, California Earthquake, Part I: Wavelet Domain Inversion Theory and Resolution Analysis", *Bull. Seismol. Soc. Am.*, 92, 1192-1207.

Kanamori, H., 1977, "The Energy Release in Great Earthquakes", *Journal of Geophysical Research*, 82, 2981-2987.

Kanamori, H. and D.L. Anderson, 1975, "Theoretical Basis of Some Empirical Relations in Seismology", *Bulletin of the Seismological Society of America*, 65, 1073-1095.

Kanamori, H. and G.S. Stewart, 1978, "Seismological Aspects of the Guatemala Earthquake of February 4, 1976", *Journal of Geophysical Research: Solid Earth*, 83, 3427-3434.

Kasahara, K., 1981, *Earthquake Mechanics*, Cambridge University Press.

Keskin, M., 2003, "Magma Generation by Slab Steepening and Breakoff Beneath a Subduction-Accretion Complex: An Alternative Model for Collision-Related Volcanism in Eastern Anatolia, Turkey", *Geophysical Research Letters,* 30, 8046.

Keskin, M., 2005, "Domal Uplift and Volcanism in a Collision Zone Without a Mantle Plume: Evidence from Eastern Anatolia", http://www. mantleplumes. org. Anatolia. html.

Keskin, M., 2007, "Eastern Anatolia: A Hotspot in a Collision Zone Without a Mantle Plume", *Geological Society of America Special Papers,* 430, 693-722.

Kikuchi, M. and H. Kanamori, 1982, "Inversion of Complex Body Waves", *Bulletin of the Seismological Society of America,* 72, 491-506.

Kikuchi, M. and H. Kanamori, 1991, "Inversion of Complex Body Waves—III", *Bulletin of the Seismological Society of America,* 81, 2335-2350.

Koçyiğit, A., A. Yılmaz, S. Adamia and S. Kuloshvili, 2001, "Neotectonics of East Anatolian Plateau (Turkey) and Lesser Caucasus: Implication for Transition from Thrusting to Strike-Slip Faulting", *Geodinamica Acta,* 14, 177-195.

Konca, A.O., V. Hjorleifsdottir, T.R.A. Song, J.P. Avouac, D.V. Helmberger, C. Ji, K. Sieh, R. Briggs and A. Meltzner, 2007, "Rupture Kinematics of the 2005 Mw 8.6 Nias-Simeulue Earthquake from the Joint Inversion of Seismic and Geodetic Data", *Bulletin of the Seismological Society of America,* 97, S307-S322.

Lawson, C.L. and R.J. Hanson, 1974, *Solving Least Squares Problems,* Prentice-Hall.

Lay, T. and T.C. Wallace, 1995, *Modern Global Seismology,* Elsevier Science.

Ligorría, J.P., 2000, *Investigation of the Mantle-Crust Transition Beneath North America and Poisson's Ratio of the North American Crust,* Saint Louis University.

Ligorria, J.P. and C.J. Ammon, 1999, "Iterative Deconvolution and Receiver-Function Estimation", *Bulletin of the Seismological Society of America,* 89, 1395-1400.

Liu, P.C. and R.J. Archuleta, 2004, "A New Nonlinear Finite Fault Inversion With Three-Dimensional Green's Functions: Application to the 1989 Loma Prieta, California, Earthquake", *Journal of Geophysical Research-Solid Earth,* 109.

Ma, K.F., J. Mori, S.J. Lee and S.B. Yu, 2001, "Spatial and Temporal Distribution of Slip for the 1999 Chi-Chi, Taiwan, Earthquake", *Bulletin of the Seismological Society of America,* 91, 1069-1087.

McClusky, S., S. Balassanian, A. Barka, C. Demir, S. Ergintav, L. Georgiev, O., Gurkan, M. Hamburger, K. Hurst, H. Kahle, K., Kastens, G. Kekelidze, R. King, V. Kotzev, O. Lenk, S. Mahmoud, A. Mishin, M. Nadariya, A. Ouzounis, D. Paradissis, Y. Peter, M. Prilepin, R. Reilinger, I. Sanli, H. Seeger, A. Tealeb, M.N. Toksöz and G. Veis, 2000, "Global Positioning System Constraints on Plate Kinematics and Dynamics in the Eastern Mediterranean and Caucasus", *Journal of Geophysical Research: Solid Earth,* 105, 5695-5719.

McGuire, J.J., L. Zhao and T.H. Jordan, 2001, "Teleseismic Inversion for the Second Degree Moments of Earthquake Space–Time Distributions", *Geophysical Journal International,* 145, 661-678.

McKenzie, D., 1972, "Active Tectonics of Mediterranean Region", *Geophysical Journal of the Royal Astronomical Society,* 30, 109-185.

Olson, A.H. and R.J. Apsel, 1982, "Finite Faults and Inverse Theory With Applications to the 1979 Imperial Valley Earthquake", *Bulletin of the Seismological Society of America,* 72, 1969-2001.

Örgülü, G., M. Aktar, N. Türkelli, E. Sandvol, M. Barazangi, 2003, "Contribution to the Seismotectonics of Eastern Turkey from Moderate and Small Size Events", *Geophysical Research Letters,* 30.

Pınar, A., 1995, *Rupture Process and Spectra of Some Major Turkish Earthquakes and Their Seismotectonic Implications*, Ph.D. Dissertation, Boğaziçi University.

Press, F., A. Ben-Menahem and M.N. Toksöz, 1961, "Experimental Determination of Earthquake Fault Length and Rupture Velocity", *Journal of Geophysical Research*, 66, 3471-3485.

Reilinger, R., S. McClusky, P. Vernant, S. Lawrence, S. Ergintav, R. Cakmak, H. Ozener, F. Kadirov, I. Guliev, R. Stepanyan, M. Nadariya, G. Hahubia, S. Mahmoud, K. Sakr, K., A. ArRajehi, D. Paradissis, A. Al-Aydrus, M. Prilepin, T. Guseva, E. Evren, A. Dmitrotsa, S.V. Filikov, F. Gomez, R. Al-Ghazzi and G. Karam, 2006, "GPS Constraints on Continental Deformation in the Africa-Arabia-Eurasia Continental Collision Zone and Implications for the Dynamics of Plate Interactions", *Journal of Geophysical Research-Solid Earth*, 111.

Scherbaum, F., 1994, *Basic Concepts in Digital Signal Processing for Seismologists*, Springer-Verlag.

Schubert, G., 2007, *Treatise on Geophysics: Earthquake Seismology*. Elsevier.

Semmane, F., F. Cotton, M. Campillo, 2005, "The 2000 Tottori Earthquake: A Shallow Earthquake With No Surface Rupture and Slip Properties Controlled by Depth", *Journal of Geophysical Research: Solid Earth*, 110, B03306.

Sengör, A.M.C., 1979, "The North Anatolian Transform Fault: Its Age, Offset and Tectonic Significance", *Journal of the Geological Society*, 136, 269-282.

Shear, P.M., 1999, *Introduction to Seismology*, Cambridge University Press.

Simons, M., S.E. Minson, A. Sladen, F. Ortega, J.L. Jiang, S.E. Owen, L.S. Meng, J.P. Ampuero, S.J. Wei, R.S. Chu, D.V. Helmberger, H. Kanamori, E. Hetland, A.W. Moore and F.H. Webb, 2011, "The 2011 Magnitude 9.0 Tohoku-Oki Earthquake: Mosaicking the Megathrust from Seconds to Centuries", *Science*, 332, 1421-1425.

Steidl, J.H., R.J. Archuleta and S.H. Hartzell, 1991, "Rupture History of the 1989 Loma Prieta, California, Earthquake by Nonlinear Inversion of Strong Motion Data", *Bull. Seismol. Soc. Am.*, 81, 1573-1602.

Stein, S. and M. Wysession, 2003, *An Introduction to Seismology, Earthquakes, and Earth Structure*. Wiley.

Stich, D., F.d.L. Mancilla, D. Baumont and J. Morales, 2005, "Source Analysis of the Mw 6.3 2004 Al Hoceima Earthquake (Morocco) Using Regional Apparent Source Time Functions", *Journal of Geophysical Research: Solid Earth*, 110, B06306.

Şaroğlu F, Emre Ö, İ, K., 1992, "Active Fault Map of Turkey", Publ. Miner Res. Explor. Ins. Turk, Ankara, Turkey

Şengör, A.M.C., M.S. Özeren, M. Keskin, M. Sakınç, A.D. Özbakır and İ. Kayan, 2008, "Eastern Turkish High Plateau as a Small Turkic-Type Orogen: Implications for Post-Collisional Crust-Forming Processes in Turkic-Type Orogens", *Earth-Science Reviews*, 90, 1-48.

Şengör, A.M.C., S. Özeren, T. Genç and E. Zor, 2003, "East Anatolian High Plateau as a Mantle-Supported, North-South Shortened Domal Structure", *Geophysical Research Letters*, 30, 8045.

Taşkın, B., A. Sezen, U.M. Tuğsal and A. Erken, 2013, "The Aftermath of 2011 Van Earthquakes: Evaluation of Strong Motion, Geotechnical and Structural Issues", *Bulletin of Earthquake Engineering*, 11, 285-312.

Taymaz, T., H. Eyidoğan and J. Jackson, 1991, "Source Parameters of Large Earthquakes in the East Anatolian Fault Zone (Turkey)", *Geophysical Journal International*, 106, 537-550.

Toksöz, M.N., J. Nábělek and E. Arpat, 1978, "Source Properties of the 1976 Earthquake in East Turkey: A Comparison of Field Data and Teleseismic Results", *Tectonophysics*, 49, 199-205.

Trifunac, M.D., 1974, "A Three-Dimensional Dislocation Model for the San Fernando, California, Earthquake of February 9, 1971", *Bulletin of the Seismological Society of America*, 64, 149-172.

Türkelli, N., E. Sandvol, E. Zor, R. Gok, T. Bekler, A. Al-Lazki, H. Karabulut, S. Kuleli, T. Eken, C. Gürbüz, S. Bayraktutan, D. Seber and M. Barazangi, 2003, "Seismogenic Zones in Eastern Turkey", *Geophysical Research Letters*, 30.

Utkucu, M., 2013, "23 October 2011 Van, Eastern Anatolia, Earthquake (M W 7.1) and Seismotectonics of Lake Van area", *J. Seismol.*, 17, 783-805.

Wald, D.J. and T.H. Heaton, 1994, "Spatial and Temporal Distribution of Slip for the 1992 Landers, California, Earthquake", *Bulletin of the Seismological Society of America*, 84, 668-691.

Wald, D.J., T.H. Heaton and K.W. Hudnut, 1996, "The Slip History of the 1994 Northridge, California, Earthquake Determined from Strong-Motion, Teleseismic, GPS, and Leveling Data", *Bulletin of the Seismological Society of America*, 86, S49-S70.

Wald, D.J., D.V. Helmberger and T.H. Heaton, 1991, "Rupture Model of the 1989 Loma Prieta Earthquake from the Inversion of Strong-Motion and Broadband Teleseismic Data", *Bull. Seism. Soc. Am.*, 81, 1540-1572.

Wu, C.J., M. Takeo, S. Ide, 2001, "Source Process of the Chi-Chi Earthquake: A Joint Inversion of Strong Motion Data and Global Positioning System Data with a Multifault Model", *Bulletin of the Seismological Society of America,* 91, 1128-1143.

Yin, A. and M.H. Taylor, 2008, "Non-Andersonian Conjugate Strike-Slip Faults: Observations, Theory, and Tectonic Implications", *IOP Conference Series: Earth and Environmental Science*, 2, 012026.

Zor, E., E. Sandvol, C. Gürbüz, N. Türkelli, D. Seber and M. Barazangi, 2003, "The Crustal Structure of the East Anatolian Plateau (Turkey) from Receiver Functions", *Geophysical Research Letters*, 30, 8044.

Clinton, J.F., 2004, *Modern Digital Seismology - Instrumentation, and Small Amplitude Studues in the Engineering World*, Ph.D. Dissertation, California Institute of Technology.

Yang, J., 2009, *Nonlinear Responses of High-Rise Buildings in Giant Subduction Earthquakes.* Ph.D. Dissertation, California Institute of Technology.

Pratt, K., 2012, *Common Conversion Point Imaging of the Western United States: Improved Methods for Receiver Function Stacks.* B.S., A Thesis in Geosciences

Toksöz, M.N., R.E. Reilinger, C.G.Doll, A.A. Barka, and N. Yalçın, 1999, "İzmit (Turkey) Earthquake of 17 August 1999: First Report", *Seismological Research Letters*, Vol.6, No.6, 669-679.

Dreger, D.S., 2002, *Time-Domain Moment Tensor Inverse Code (TDMT_INVC) Version 1.1*, ftp://www.orfeus-eu.org/pub/software/iaspei2003/8511_tutorial.pdf

Emre O., T.Y. Duman, S. Özalp and H. Elmacı, 2011, "Site Observations and Preliminary Evaluation of Source Fault of 23 October 2011 Van Earthquake", *Active Tectonics Research Group, MTA Publications*, Ankara (in Turkish).

Yagi, Y. and M. Kikuchi, 2001, *Spatiotemporal Distribution of Source Rupture Process for 1999 Chi-Chi, Taiwan Earthquake*, http://www.eic.eri.u-tokyo.ac.jp/yuji/taiwan/taiwan.html

Hayes G., 2011, *Updated Result of the Oct. 23, 2011 Mw 7.1 Eastern Turkey Earthquake*, http://earthquake.usgs.gov/earthquakes/eqinthenews/2011/usb0006bqc/finite_fault.php

Yagi, Y., 2011, *October 2011 Eastern Turkey Earthquake (Preliminary Result)*, http://www.geol.tsukuba.ac.jp/~yagi-y/EQ/2011_E_Turkey/index_e.html

Dhont, D. and J. Chorowicz, 2006, "Review of the Neotectonics of the Eastern Turkish–Armenian Plateau by Geomorphic Analysis of Digital Elevation Model Imagery", I*nt J Earth Sci (Geol Rundsch)*, 95:34–49. doi:10.1007/s00531-005-0020-3.

Şengör, A.M.C, N. Görür, and F. Şaroğlu, 1985, "Strike-Slip Faulting and Related Basin Formation in Zones of Tectonic Escape: Turkey as a Case Study", in K.T. Biddle and N. Christie-Blick (eds.), *Strike-Slip Faulting and Basin Formation*, S*pec Publ Soc Econ Paleontol Mineral* 37:227–264.

DATA SOURCES

IRIS, WILBER II

Global CMT Catalog

International Seismological Center (ISC)

NOAA, National Geophysical Data Center

BASE MAP

ESRI, Digital Chart of the World

USGS, The United States Geological Survey, Data Center

GMT-The Generic Mapping Tools

MATLAB

EMSC-Eastern Mediterranean Seismological Center, http://www.emsc-csem.org

APPENDIX A. LIST OF STATIONS

Table A.1. List of teleseismic stations (20° to 90°).

Station	Latitude	Longitude	GCARC	Azimuth
MLY	65.0308	-150.739	75.9722	6.13605
TIXI	71.649	128.867	52.3589	23.5004
ARU	56.4293	58.5615	20.3575	24.6842
BRVK	53.0581	70.2828	23.3764	43.4569
HIA	49.2667	119.742	53.7101	52.1576
TLY	51.6807	103.644	43.1672	52.1909
KURK	50.7154	78.6202	27.472	52.6285
ULN	47.8652	107.053	46.0141	56.9945
MAKZ	46.808	81.977	29.2033	61.3811
MKAR	46.7937	82.2904	29.418	61.424
BJT	40.0183	116.168	54.7527	63.9143
TARG	41.7291	77.8048	26.3304	72.4564
ARLS	41.861	74.323	23.7241	72.5626
ENH	30.2718	109.487	54.0657	77.6124
BTK	40.058	70.818	21.2004	77.7531
LSA	29.7	91.15	40.1171	88.1396
QIZ	19.0294	109.843	60.1526	88.8232
CHTO	18.8138	98.9438	51.7632	96.0891
PALK	7.2728	80.7022	45.9301	123.204
MSEY	-4.6737	55.4792	44.6193	162.728
ATD	11.53	42.847	27.1009	181.194
FURI	8.89667	38.6783	30.0152	189.362
TAM	22.7917	5.52333	35.9332	254.915
CLTB	37.5786	13.2156	23.7176	276.699
CUC	39.9931	15.8156	21.3368	282.103
AQU	42.3539	13.4019	23.0227	288.62
VLC	44.1594	10.3864	25.2245	293.043
FUORN	46.6202	10.2635	25.4593	298.773
KBA	47.0784	13.3447	23.4278	300.575

GRA1	49.6919	11.2217	25.342	306.092
OJC	50.2195	19.7984	20.2869	312.111
GKP	53.2697	17.2367	23.0936	317.527
VSU	58.462	26.7347	22.4862	336.786

Table A.2. List of regional stations (1° to 20°).

Station	Latitude	Longitude	GCARC	Azimuth
AKH	41.41	43.4928	2.66879	1.46702
GUDG	42.4646	44.4772	3.81057	12.0595
ERE	40.17	44.47	1.65105	29.7163
QZX	41.058	45.372	2.76776	32.5721
ZKT	41.654	46.667	3.83762	39.6204
GDB	40.721	45.754	2.68462	41.7548
ABKAR	49.2556	59.9431	15.8447	43.0951
SEK	41.209	47.198	3.81971	48.575
GANJ	40.646	46.322	2.94988	48.8688
MNG	40.773	47.085	3.49055	53.2528
XNQ	41.172	48.14	4.37717	54.7874
QBL	40.946	47.837	4.06345	55.7545
IML	40.793	48.182	4.21601	59.3823
PQL	40.789	48.593	4.49353	61.2632
ZRD	40.279	47.684	3.65169	63.749
GBS	40.535	48.942	4.63771	65.5079
NDR	40.581	49.987	5.40423	68.0307
GAL	40.41	50.155	5.47796	70.1442
ALI	39.958	49.006	4.51167	72.591
NAX	39.174	45.495	1.68865	74.4406
GLB	39.242	48.393	3.92133	81.0819
LRK	38.643	48.34	3.86506	89.8824
UOSS	24.9453	56.2042	17.5067	138.034
RAYN	23.5225	45.5032	15.2746	172.661
EIL	29.6699	34.9512	11.4291	220.2
MARD	37.3139	40.7789	2.51289	236.328
LEF	35.1193	32.8903	9.15791	249.998

CEYT	37.01	35.748	6.2959	256.459
ANTB	36.8998	30.6538	10.2525	263.637
KONT	37.9453	32.3605	8.71317	268.218
KULA	38.5144	28.6607	11.5362	273.491
ALT	39.0552	30.1103	10.3676	275.903
SVRH	39.4469	31.523	9.26442	278.096
BBAL	39.5427	33.123	8.02941	278.955
KEMA	39.2688	38.4932	3.86069	279.41
ANTO	39.8689	32.7936	8.30275	281.136
GULT	40.4323	30.515	10.0918	283.698
YLVX	40.5667	29.3728	10.9714	283.991
SVSK	39.917	36.998	5.10317	285.334
BUY	40.8523	29.1181	11.1922	285.37
TIR	41.3477	19.865	18.1989	285.697
ISK	41.0656	29.0592	11.2615	286.43
RSDY	40.3972	37.3273	4.9777	291.338
HAVZ	41.0743	35.718	6.3513	293.963
DIVS	44.0982	19.9917	18.3311	294.471
KVT	41.0806	36.0464	6.11946	294.783
DIKM	41.6496	35.2578	6.87869	297.569
TIRR	44.4581	28.4128	12.5847	301.782
BUR31	47.644	25.2002	15.9513	309.773
KIEV	50.6944	29.2083	15.6072	324.574
OBN	55.1138	36.5687	17.0181	346.493
KIV	43.9553	42.6863	5.23946	354.331

APPENDIX B. Slip Models Inverted From Regional, Teleseismic and Joint Data

Table B.1. Slip Models for the rise time T_D=1.0 s and the rupture velocities of 1.0-4.0 km/s.

T_D=1.0 s	Regional	Teleseismic	Joint
V_R = 1.0 km/s	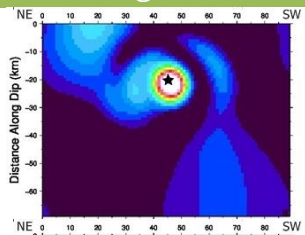	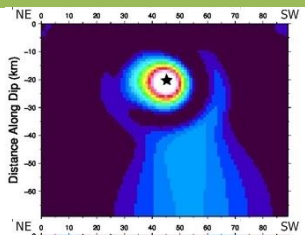	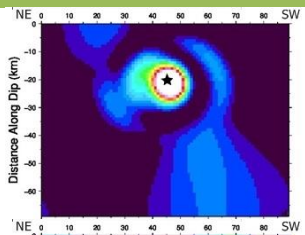
V_R = 1.5 km/s	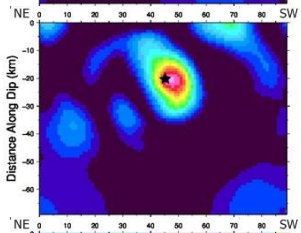	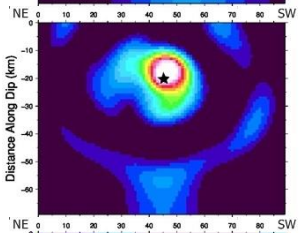	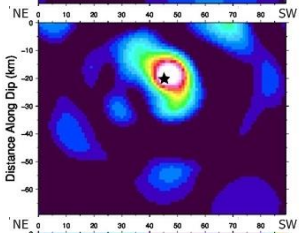
V_R = 2.0 km/ss	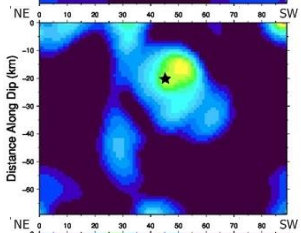	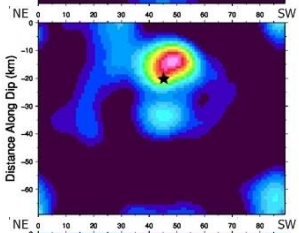	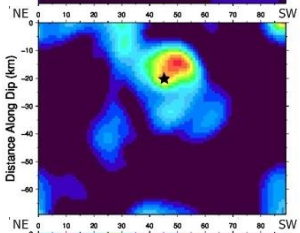
V_R = 2.5 km/s	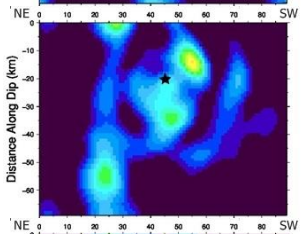	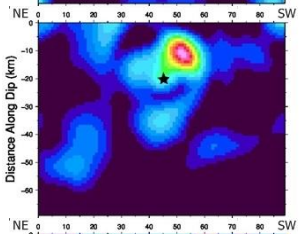	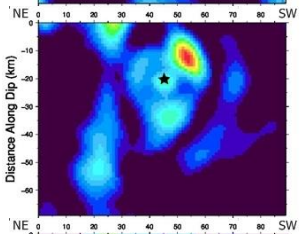
V_R = 3.0 km/s	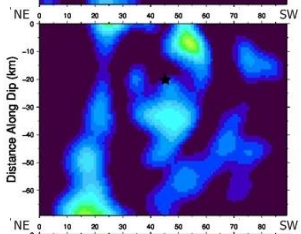	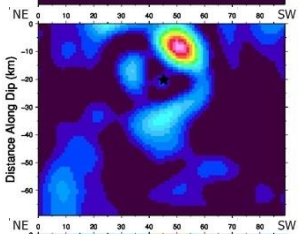	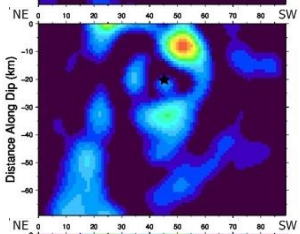
V_R = 3.5 km/s	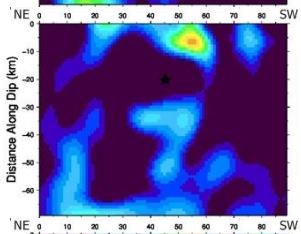	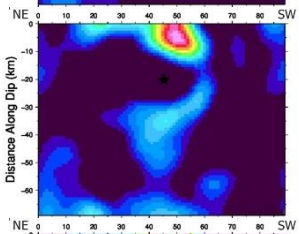	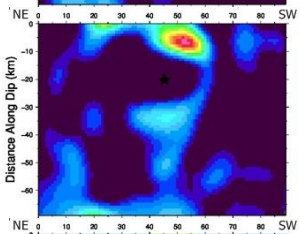
V_R = 4.0 km/s	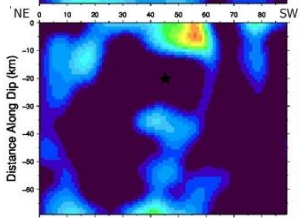	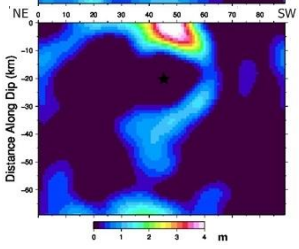	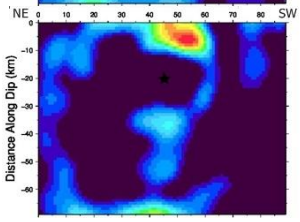

Table B.2. Slip Models for the rise time T_D=1.5 s and the rupture velocities of 1.0-4.0 km/s.

T_D=1.5 s	Regional	Teleseismic	Joint
V_R = 1.0 km/s	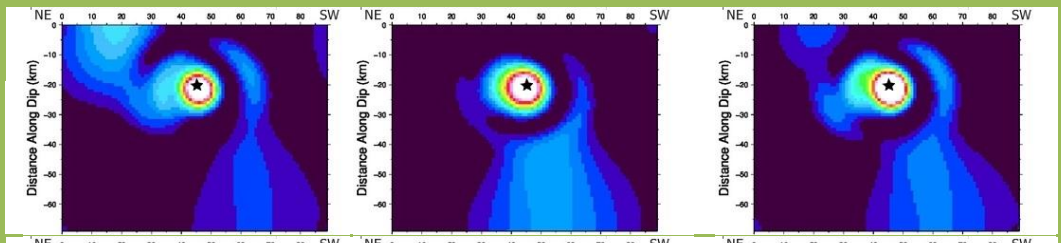		
V_R = 1.5 km/s	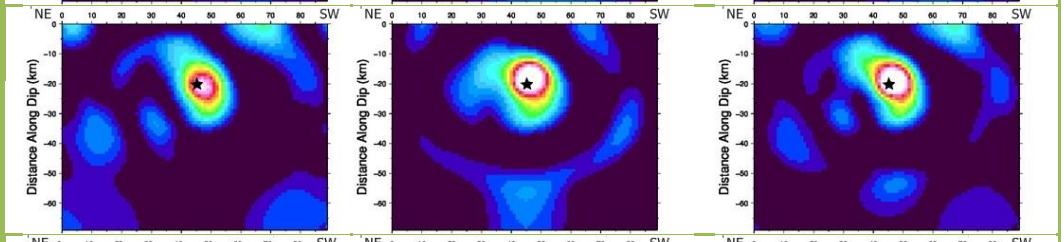		
V_R = 2.0 km/s	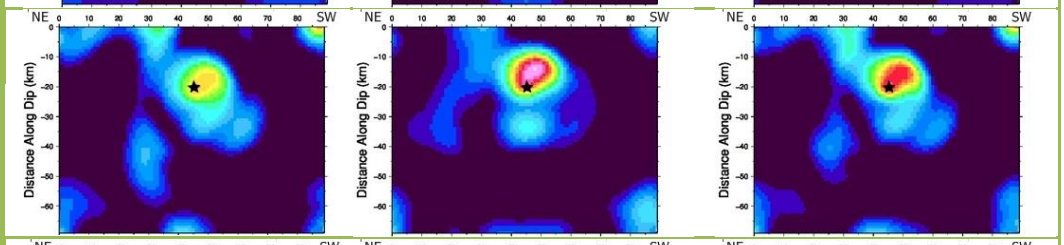		
riseV_R = 2.5 km/s	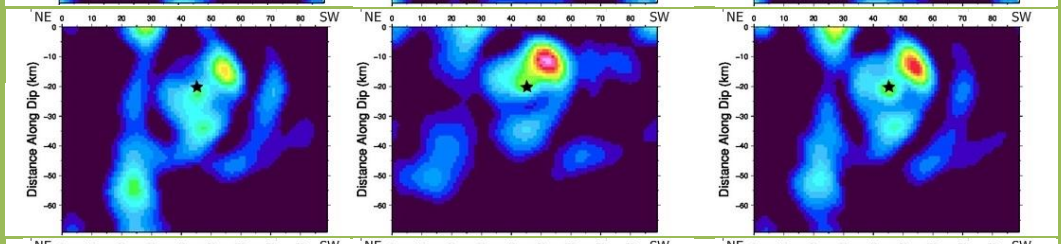		
V_R = 3.0 km/s	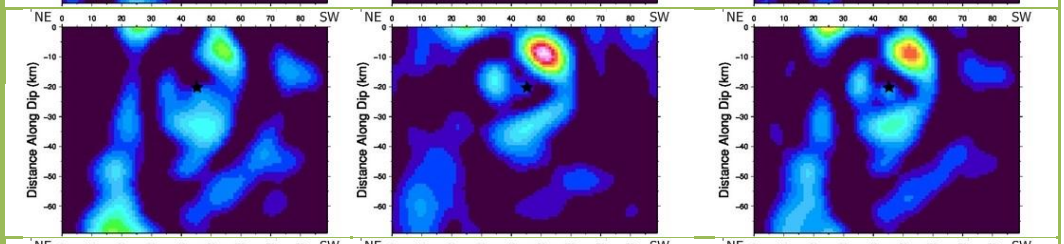		
V_R = 3.5 km/s	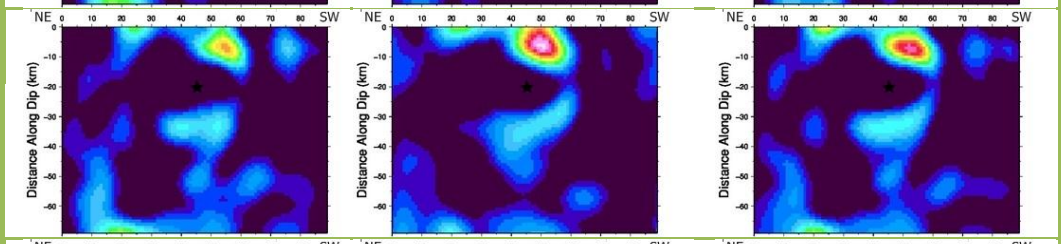		
V_R = 4.0 km/s	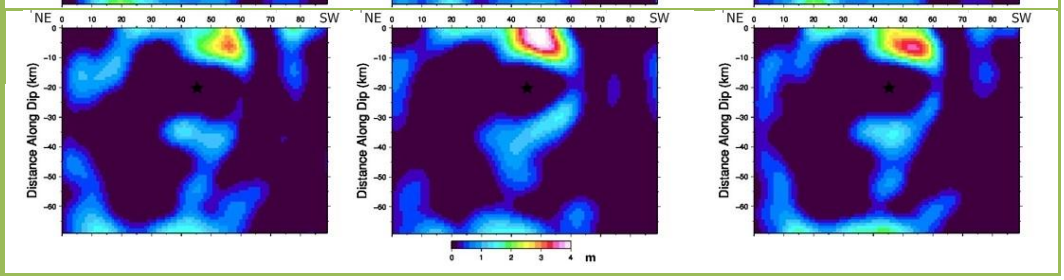		

Table B.3. Slip Models for the rise time T_D=2.0 s and the rupture velocities of 1.0-4.0 km/s.

T_D=2.0 s	Regional	Teleseismic	Joint
V_R = 1.0 km/s	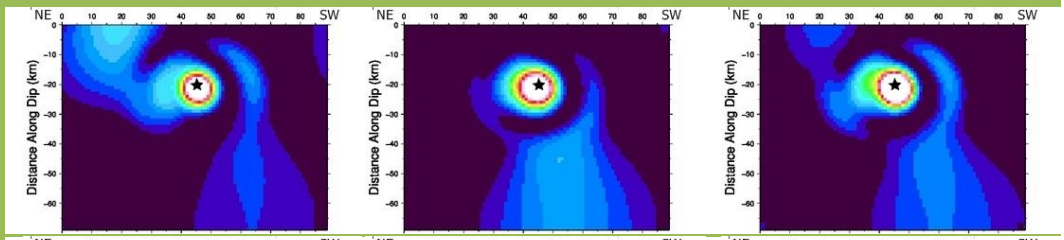		
V_R = 1.5 km/s	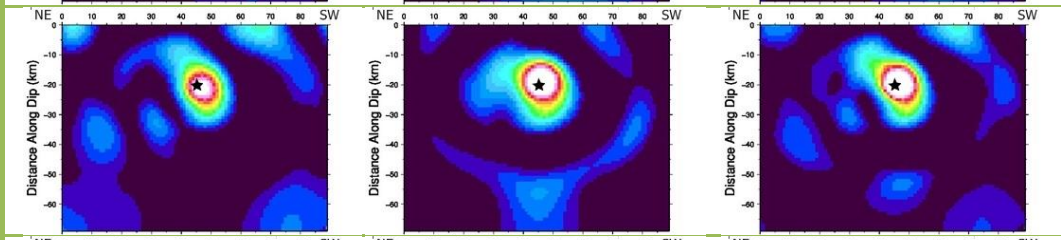		
V_R = 2.0 km/s	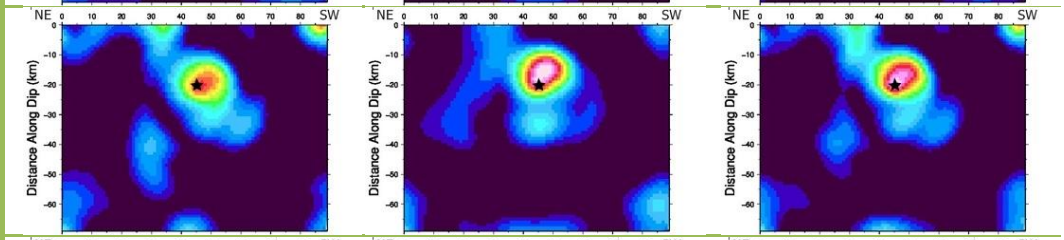		
V_R = 2.5 km/s	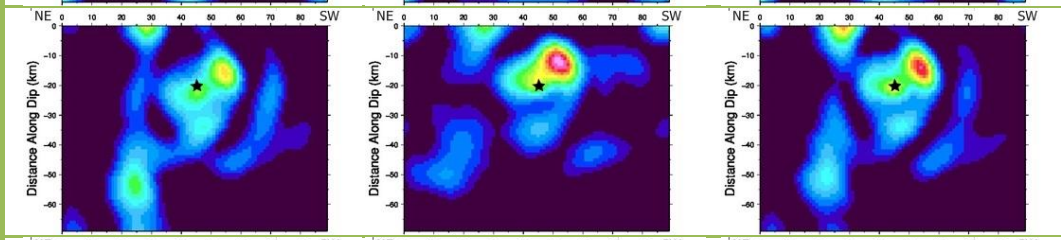		
V_R = 3.0 km/s	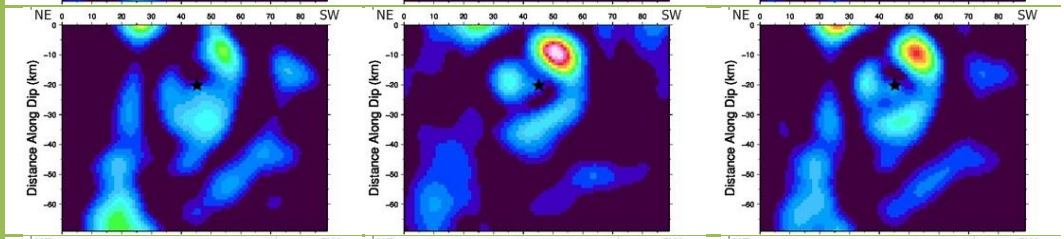		
V_R = 3.5 km/s	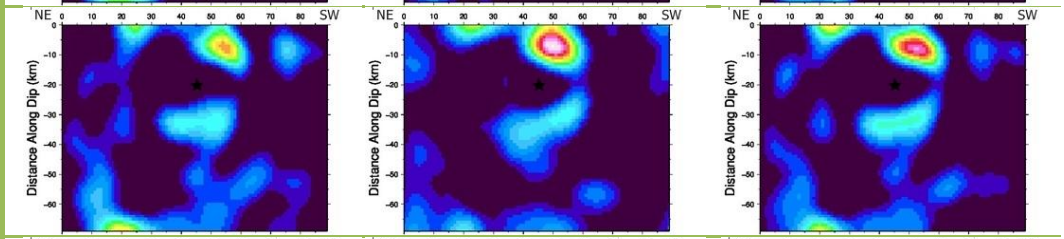		
V_R = 4.0 km/s	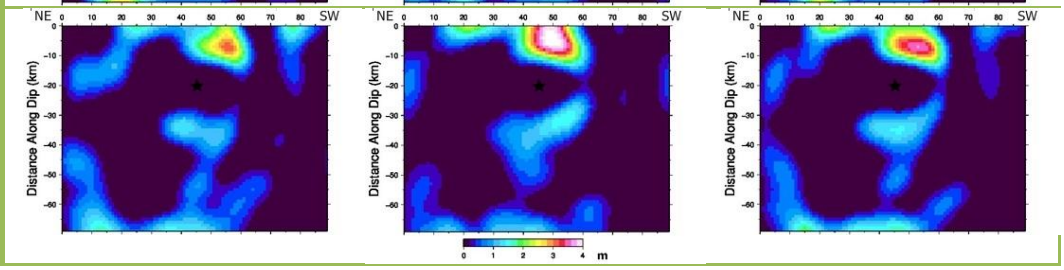		

Table B.4. Slip Models for the rise time T_D=2.5 s and the rupture velocities of 1.0-4.0 km/s.

T_D=2.5s	Regional	Teleseismic	Joint
V_R = 1.0 km/s	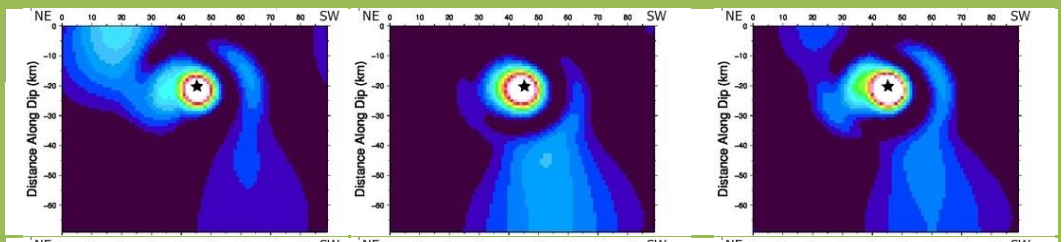		
V_R = 1.5 km/s	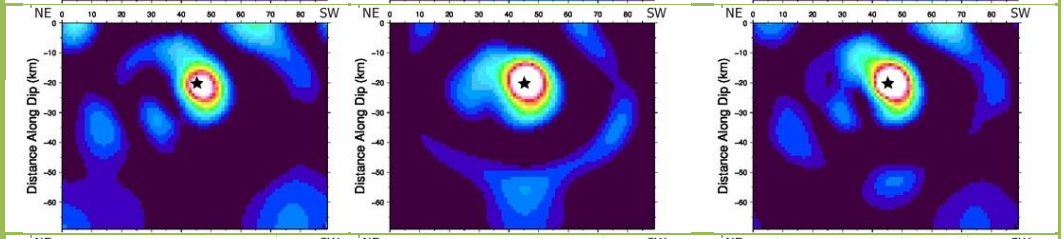		
V_R = 2.0 km/s	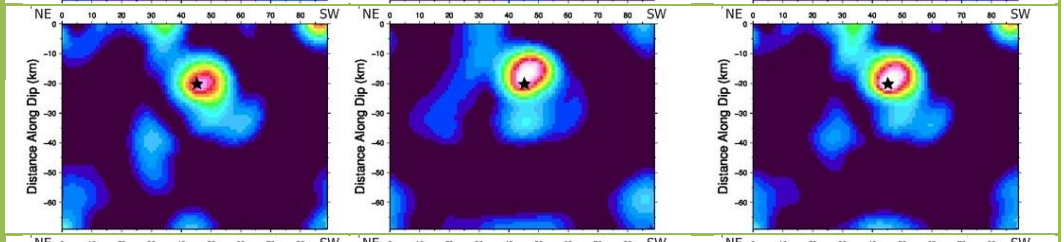		
V_R = 2.5 km/s	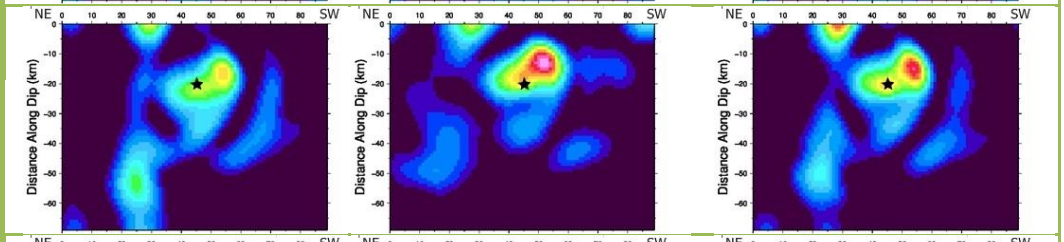		
V_R = 3.0 km/s	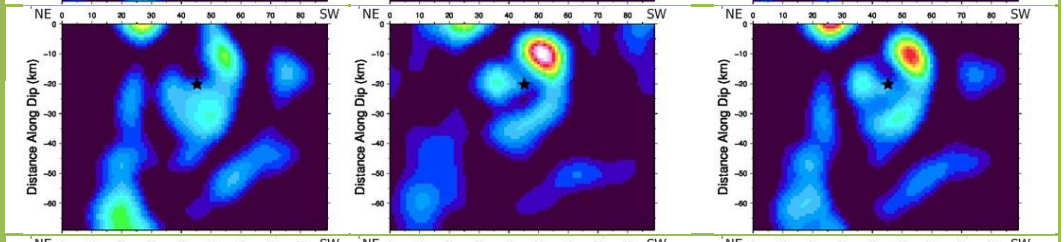		
V_R = 3.5 km/s	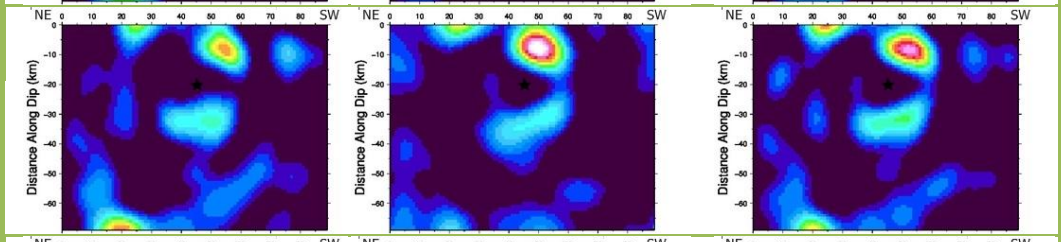		
V_R = 4.0 km/s	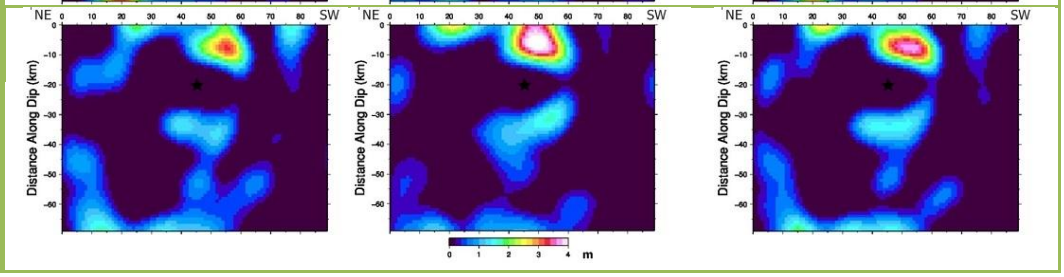		

Table B.5. Slip Models for the rise time T_D=3.0 s and the rupture velocities of 1.0-4.0 km/s.

T_D=3.0s	Regional	Teleseismic	Joint
V_R = 1.0 km/s	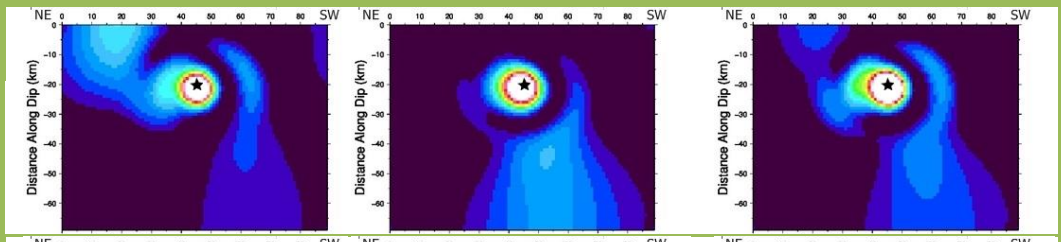		
V_R = 1.5 km/s	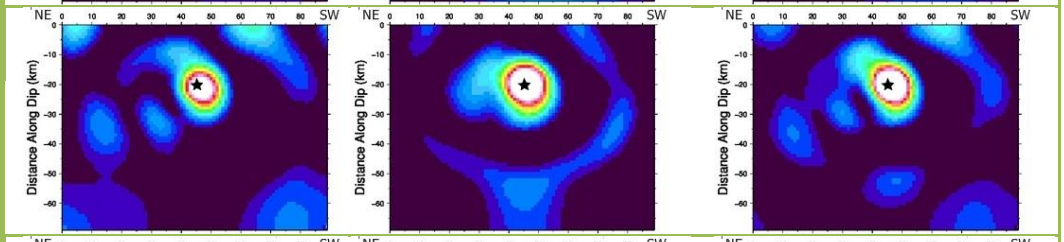		
V_R = 2.0 km/s	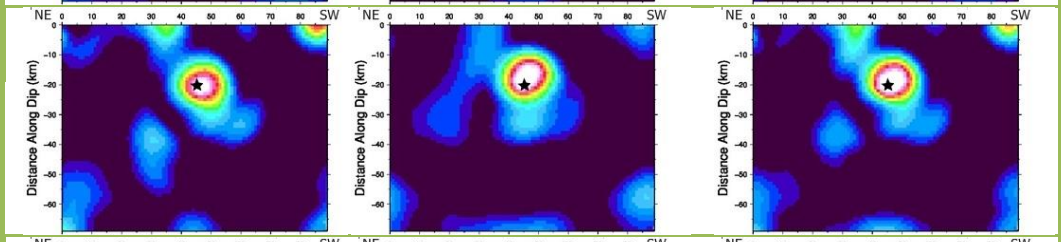		
V_R = 2.5 km/s	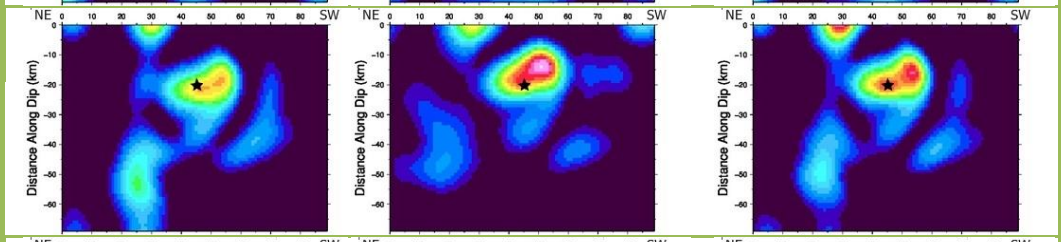		
V_R = 3.0 km/s	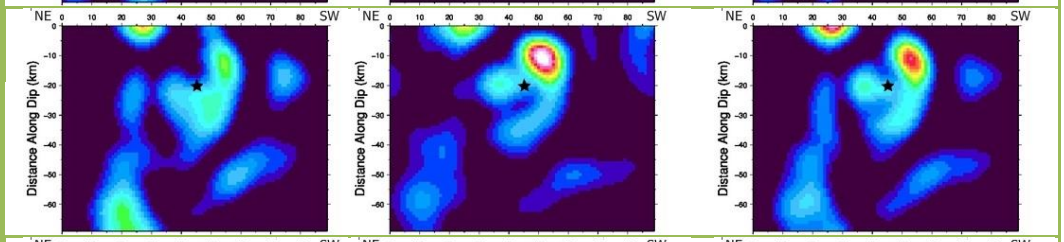		
V_R = 3.5 km/s	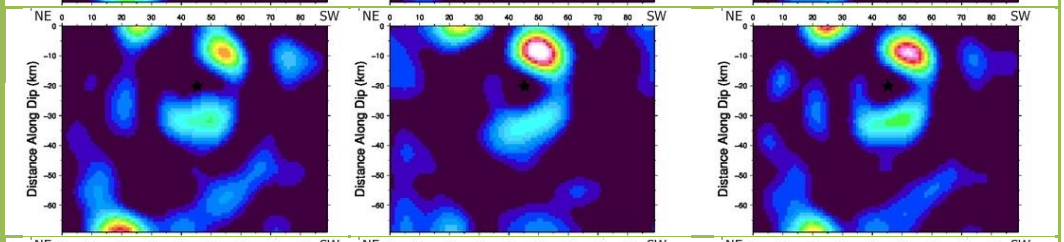		
V_R = 4.0 km/s	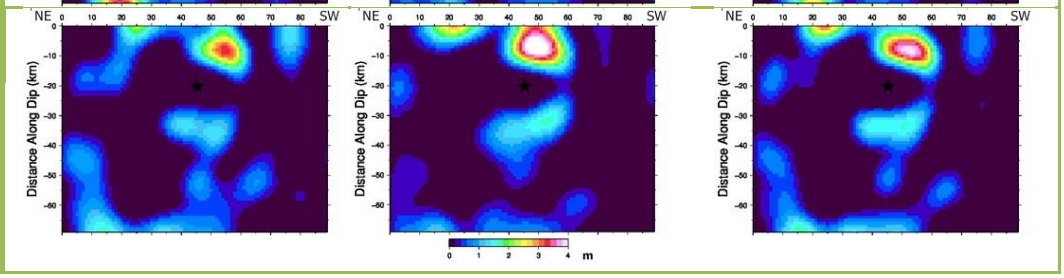		

Table B.6. Slip Models for the rise time T_D=3.5 s and the rupture velocities of 1.0-4.0 km/s.

T_D=3.5s	Regional	Teleseismic	Joint
V_R = 1.0 km/s	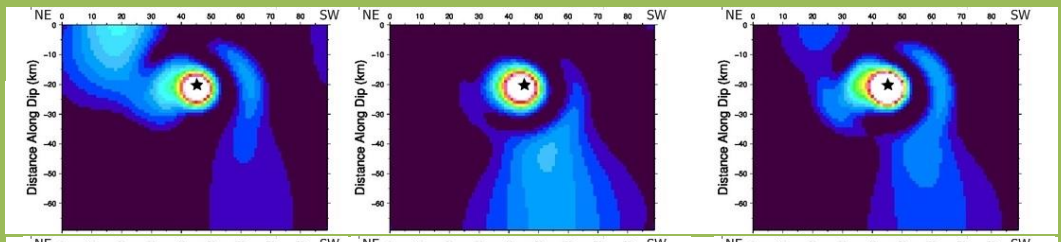		
V_R = 1.5 km/s	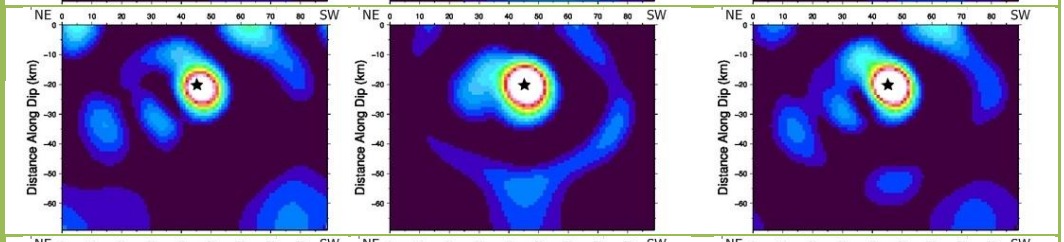		
V_R = 2.0 km/s	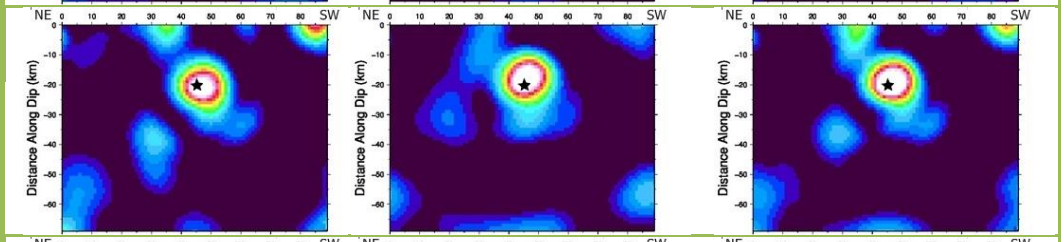		
V_R = 2.5 km/s	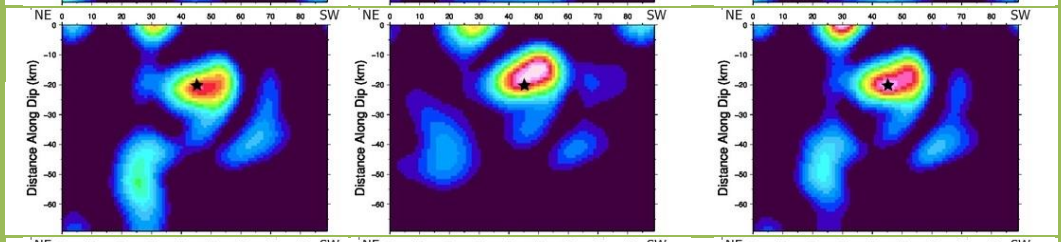		
V_R = 3.0 km/s	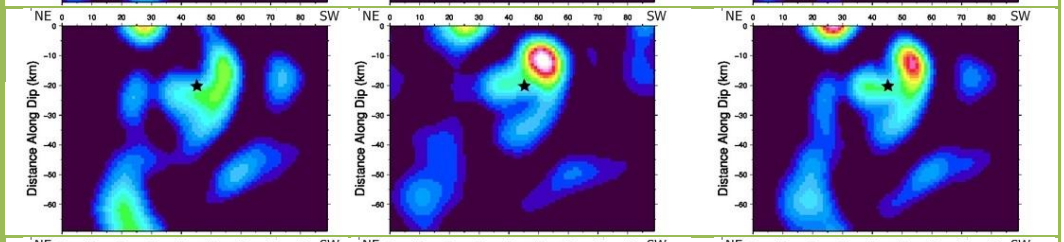		
V_R = 3.5 km/s	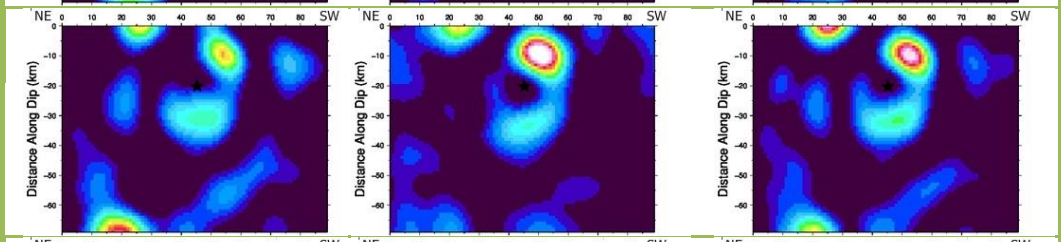		
V_R = 4.0 km/s	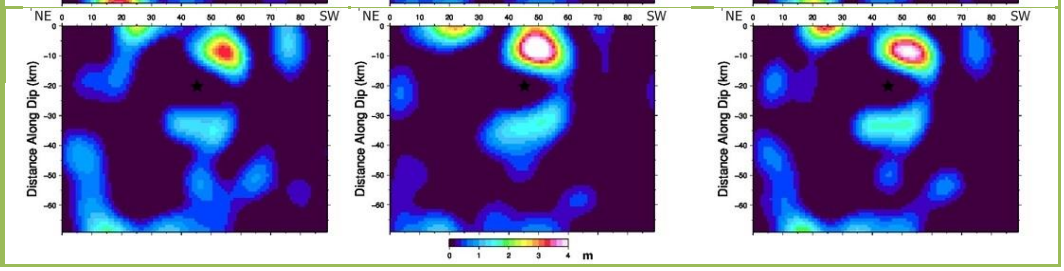		

Table B.7. Slip Models for the rise time T_D=4.0 s and the rupture velocities of 1.0-4.0 km/s.

T_D==4.0s	Regional	Teleseismic	Joint
V_R = 1.0 km/s	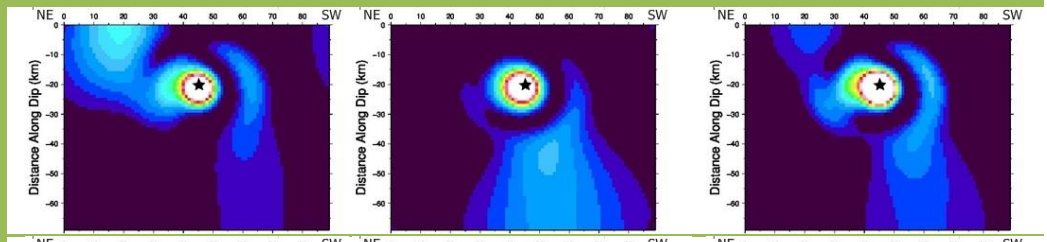		
V_R = 1.5 km/s	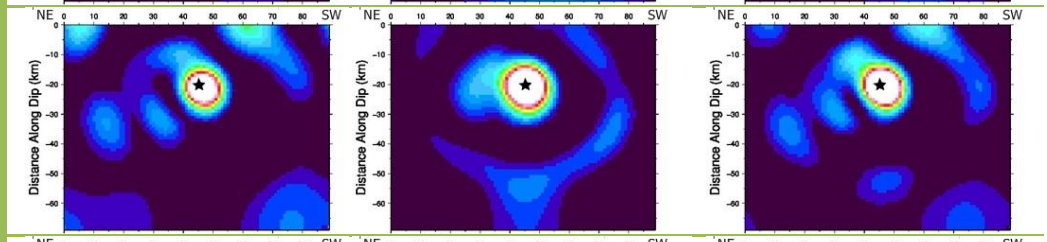		
V_R = 2.0 km/s	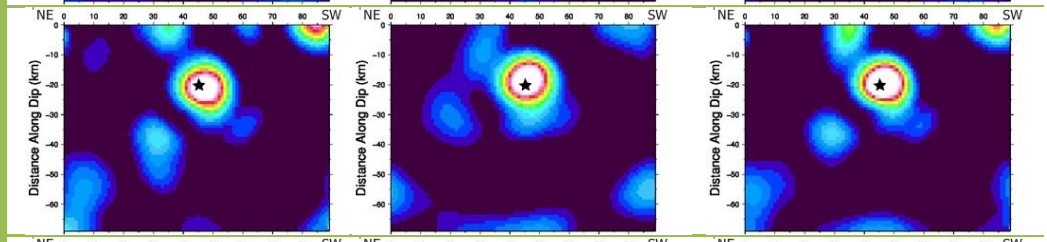		
V_R = 2.5 km/s	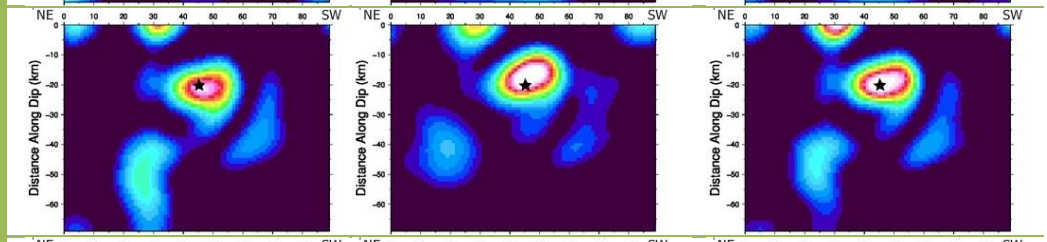		
V_R = 3.0 km/s	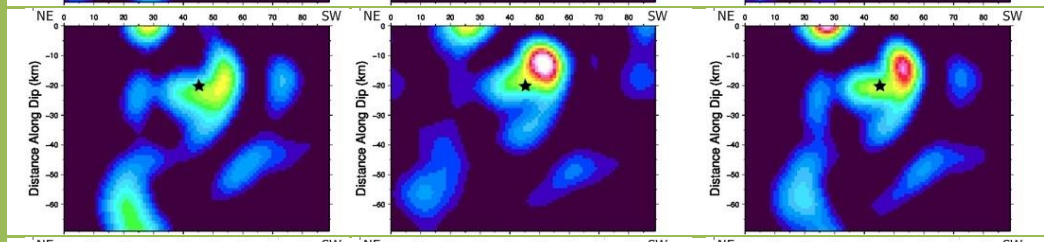		
V_R = 3.5 km/s	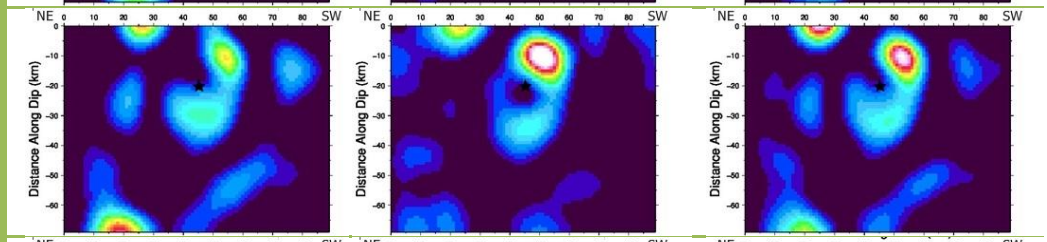		
V_R = 4.0 km/s	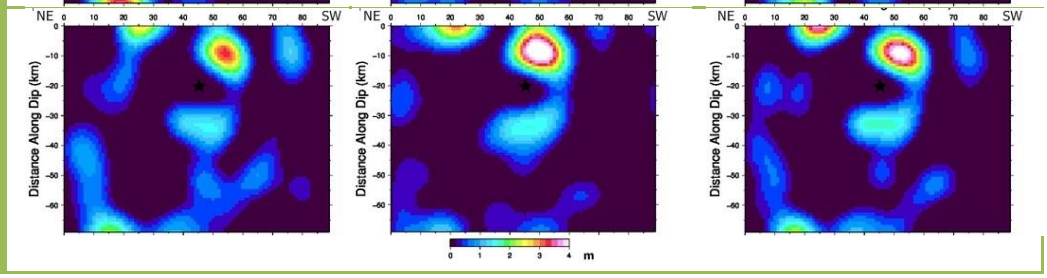		

Table B.8. Slip Models for the rise time T_D=4.5 s and the rupture velocities of 1.0-4.0 km/s.

T_D=4.5s	Regional	Teleseismic	Joint
V_R = 1.0 km/s	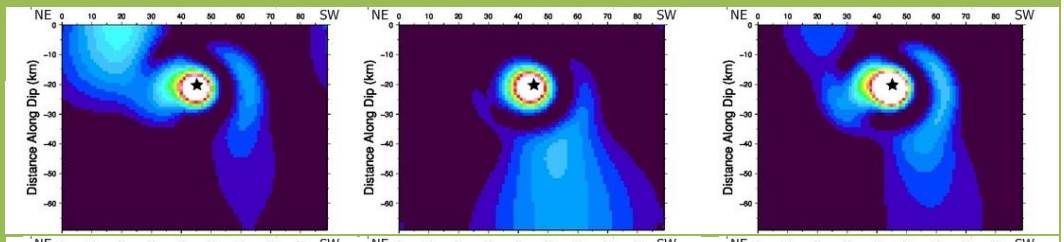		
V_R = 1.5 km/s	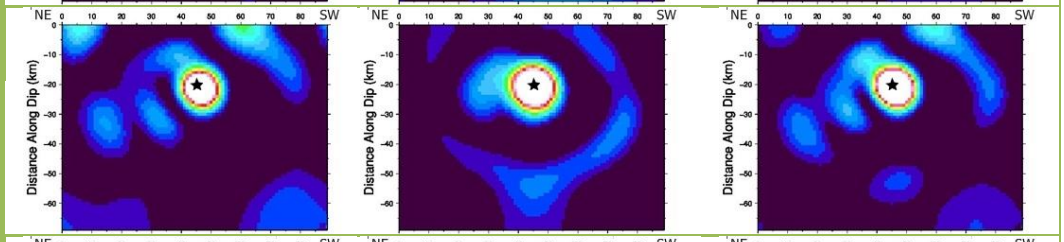		
V_R = 2.0 km/s	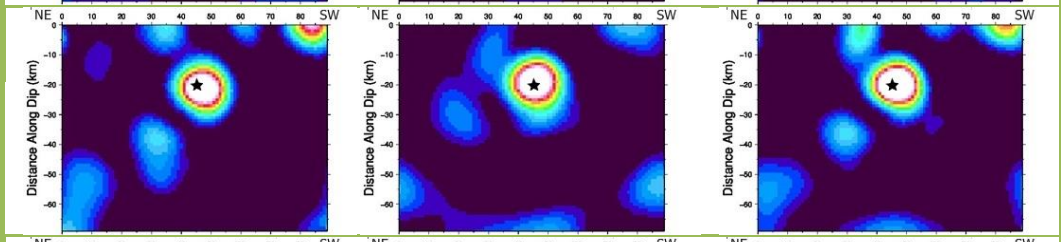		
V_R = 2.5 km/s	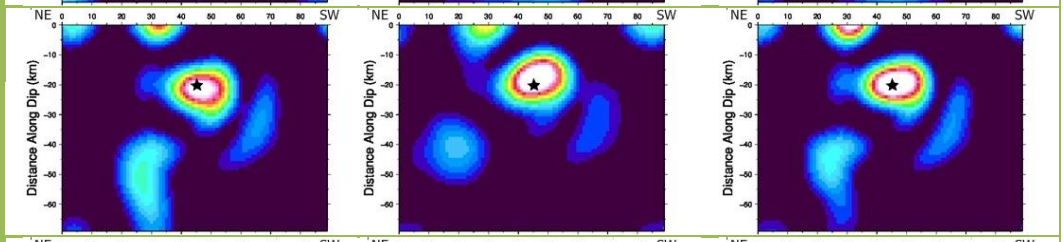		
V_R = 3.0 km/s	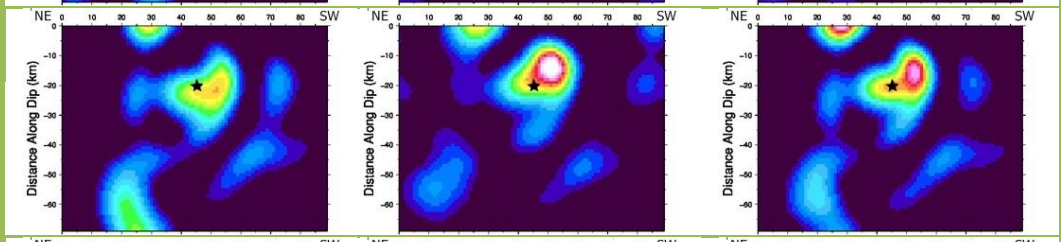		
V_R = 3.5 km/s	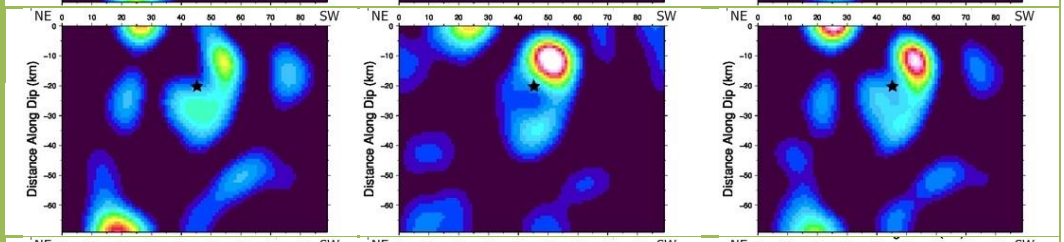		
V_R = 4.0 km/s	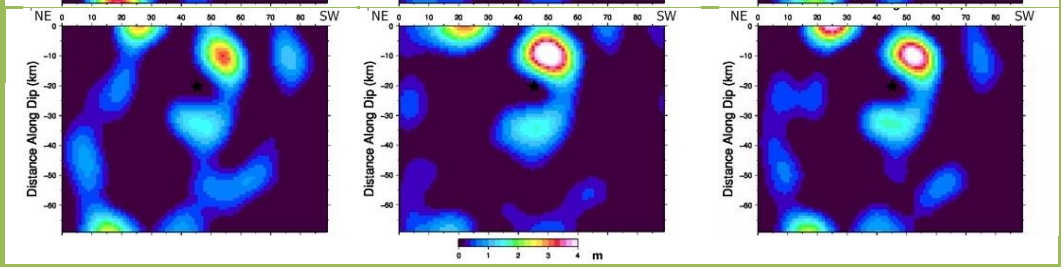		

Table B.9. Slip Models for the rise time T_D=5.0 s and the rupture velocities of 1.0-4.0 km/s.

T_D =5.0s	Regional	Teleseismic	Joint
V_R = 1.0 km/s	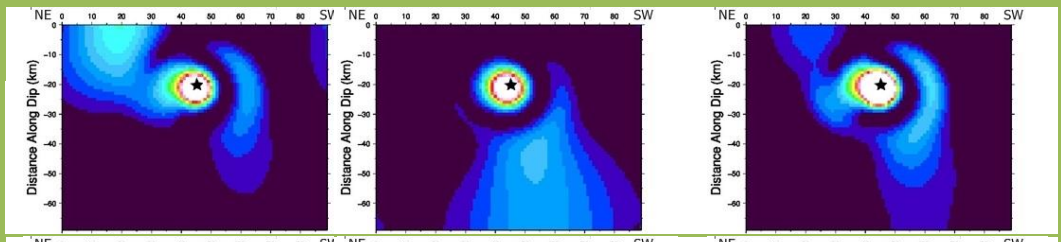		
V_R = 1.5 km/s	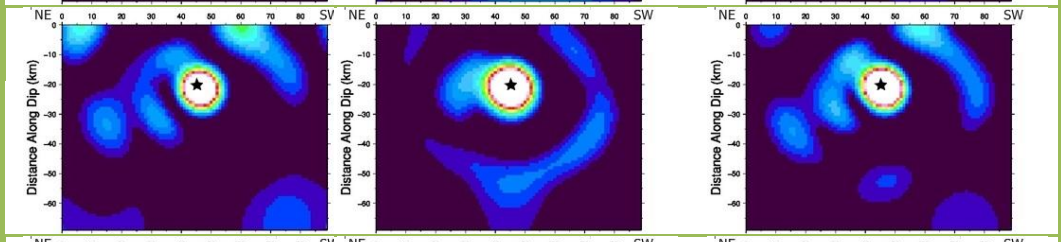		
V_R = 2.0 km/s	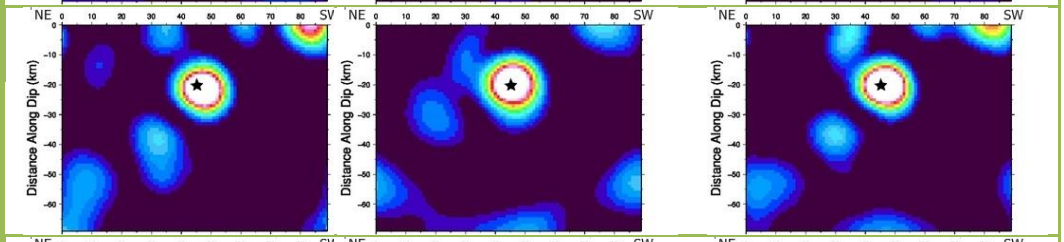		
V_R = 2.5 km/s	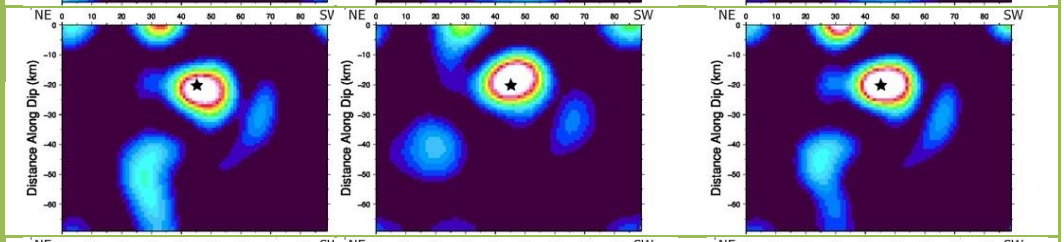		
V_R = 3.0 km/s	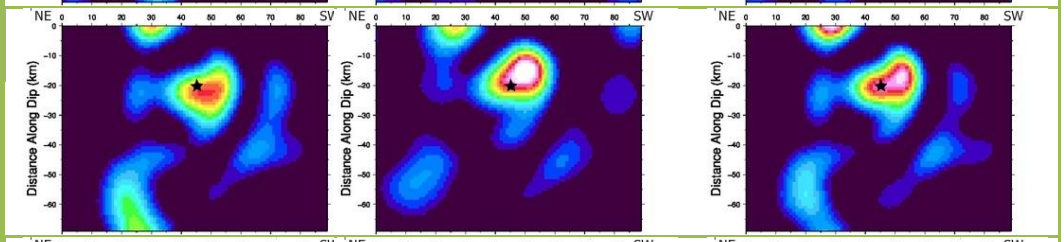		
V_R = 3.5 km/s	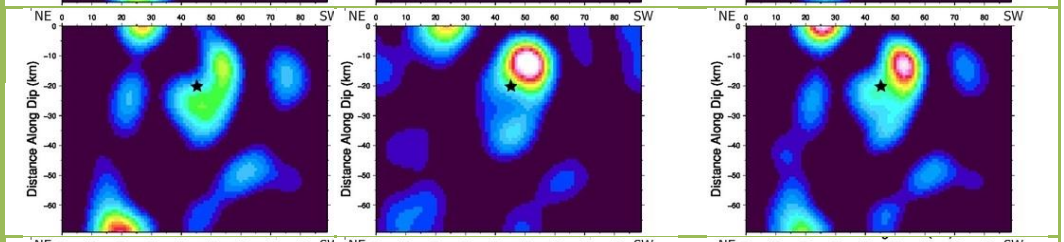		
V_R = 4.0 km/s	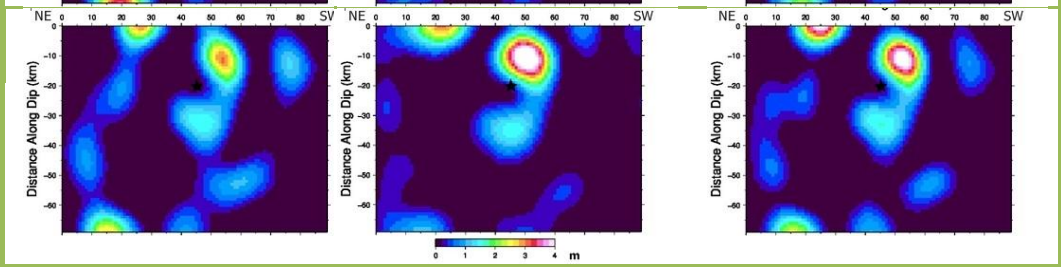		

APPENDIX C. Pre-processing

Table C.1. SAC commands used for pre-processing.

```
bp bu co $FL $FH np 4 p 2
cut t0 $CUTL $CUTH
rmean
rtrend
interpolate delta $INTDELTA
taper type HANNING WIDTH 0.1
```

Table C.2. The use of SAC file tool "saciterd".
(http://www.eas.slu.edu/eqc/eqc_cps/CPS/CPS330/cps330g.pdf)

```
saciterd -FN N -FD D -ALP ${ALP} -POS -D 3 -N 200
```

-FN represents the numerator N which is the big event and -FD represents the denominator D which is the small event. We used $ALP = 0.75$ which is the width of the Gaussian filter. N is the number of iterations ($N = 200$) and D is the delay of the output in seconds.